The structural setting of the Barsele Au deposit, Sweden

Tobias E Bauer
Luleå University of Technology, Sweden

Marcello Imaña, Kåre Höglund
Agnico Eagle Sweden AB

Helen Thomas
Luleå University of Technology, Sweden

Abstract. The Barsele Au deposit is hosted in Paleoproterozoic rocks that were subject to multiple deformation events during the Svecofennian orogeny 1.9-1.8 Ga ago. Rocks have been subjected to an approx. N-S-directed extensional event (1.89 Ga) potentially responsible for the formation of VMS deposits. The crustal extension was followed by a compressional event under ductile conditions and related basin inversion (D_2; 1.87 Ga) and overprinted by a brittle event at 1.8 Ga (D_3). The distribution of alteration minerals and veins suggests multiple phases of fluid flow and remobilisation. The latest phase of enrichment appears to be coupled to low-angle thrusting from ESE and brittle reactivation of earlier structures with emplacement of quartz veins along fault planes and tensile structures in an oblique Riedel system.

1 Introduction

The Barsele prospect is located in the Storuman area and forms part of the so-called Gold Line, a NW-SE trending belt of anomalous gold mineralization that occur c. 50 km southwest of the Skellefte district. In addition to Barsele the deposits in the belt include Knaften, Fäboliden, Svartliden, Stortjärnshobben and Blaiken (Bark & Weihed 2007). The Storuman area is tentatively suggested as the westward continuation of the Skellefte district and hosts both volcanic-hosted massive sulphide (VMS) deposits as the Norra VMS deposit and orogenic gold mineralizations.

This ongoing project is based on field work, mainly mapping an exploration trench at Barsele Central but also regional structural geological mapping. Additionally, structural framework modelling was performed from oriented drill core data using the MOVE software package (Midland Valley Exploration). The aim is to constrain structural controls on Au mineralizations in the area.

2 Regional geological framework

The Barsele prospect is located within Palaeoproterozoic supracrustal and associated intrusive rocks (Fig. 1). Bedrock in the area consists of 1.9–1.8 Ga supracrustal and associated intrusive rocks that were deformed and metamorphosed during the Svecokarelian orogeny (Lundström et al. 1997; Mellqvist et al. 1999; Kathol & Weihed 2005). The Storuman area is bordering the Skellefte district in the east. North of the district Palaeoproterozoic and reworked Archaean rocks form the Norrbotten craton. South of the study area, metasedimentary rocks of the Bothnian Basin occur.

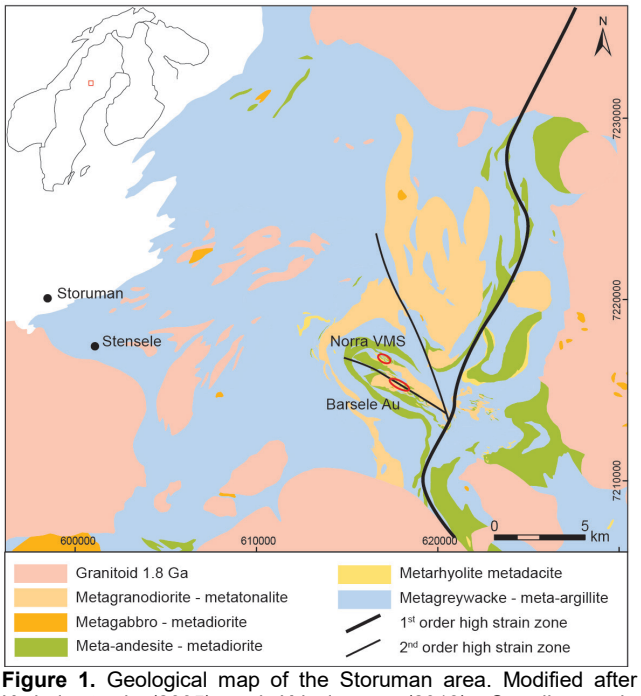

Figure 1. Geological map of the Storuman area. Modified after Kathol et al. (2005) and Krispinsson (2018). Coordinates in SWEREF99.

The lowest stratigraphic unit in the area consists of metasedimentary and intercalated volcanic rocks of the Bothnian Supergroup (Kathol & Weihed 2005; Skyttä et al. 2012). A metadacite in the Barsele area with an age of 1959±14 Ma (Eliasson et al. 2001) is regarded to form a part of this Supergroup. The Bothnian Supergroup forms the inferred basement to the 1.89-1.88 Ga, mainly felsic volcanic rocks of the Skellefte Group (Allen et al. 1996; Skyttä et al. 2011) that formed during a phase of crustal extension ($\mathbf{D_1}$) and utilizing syn-extensional normal and related transfer faults for emplacement (Bauer et al. 2011). VMS deposits formed dominantly as sub-seafloor replacement in volcanoclastic and sedimentary rocks and partly as exhalative deposits within the stratigraphically uppermost part of Skellefte Group volcanic rocks (Allen et al. 1996) utilizing the syn-extensional faults as fluid conduits (Bauer et al. 2014).

Studies from the close by Skellefte district indicate that the Skellefte Group volcanic rocks are overlain by a 1.88 - 1.87 Ga, dominantly sedimentary unit called the

Vargfors Group (Allen et al. 1996). Recent studies suggest that the local stratigraphy is comparable to volcanic evolution of the Skellefte district.

The oldest intrusive rocks in the district are early orogenic, 1.89-1.88 Ga granitoids, diorites and gabbros, including a quartz-monzodiorite in Barsele that has been dated at 1880±4 Ma (Eliasson et al. 2001). These early orogenic rocks are suggested to be co-magmatic with the volcanic rocks of the Skellefte Group. Younger phases of intrusives are assigned to the Perthite-Monzonite suite (Witschard 1984), which formed between 1.88 and 1.86 Ga (c.f. Bejgarn et al. 2012) and post-date the deposition of the volcanic rocks. In the south, west and in-between the Skellefte district and the Storuman area, the Skellefte, Vargfors and Bothnian Groups are all truncated by large intrusions of 1.82-1.78 Ga, late- to post-Svecokarelian GSDG-type (also referred to as Revsund-type) intrusive rocks of the Transscandinavian Igneous Belt (Kathol & Weihed 2005).

The main compressional deformation event (**D_2**) took place at 1.88-1.87 Ga and resulted in folding, re-activation of the syn-extensional faults and related transposition of VMS deposits (Bauer et al. 2011). The latest major deformation event at 1.82-1.80 Ga (**D_3**; Weihed et al. 2002) is inferred to have resulted from east-west crustal shortening causing reactivation of major syn-extensional high-strain zones with reverse kinematics (Bergman Weihed et al. 1996; Bauer et al., 2011; Skyttä et al., 2012). Gold deposits south of the Stensele area are classified as orogenic gold deposits and are related to the E-W crustal shortening event at 1.80 Ga (**D_3**; Bark & Weihed 2007).

3 Structures and related hydrothermal alteration

3.1 Ductile structures

The main mineralization at Barsele (Central) is hosted by an early orogenic metagranodiorite that intruded prior to metamorphism. Multiple generations of structures occur in Barsele and can be observed in a trench above the central deposit, in oriented drill-core and regional outcrops. The earliest observable structures are represented by a penetrative foliation (S_2) and can be correlated to the regional foliation that formed as a response to D_2 crustal shortening around 1.87 Ga (c.f. Bauer et al. 2011; Skyttä et al. 2012). Foliation intensity is varying from unfoliated to strong with the formation of a mylonitic fabric. The deposit is located within a series of WNW-ESE-trending shear zones (D_2). These high strain zone are characterized by strong strain partitioning and the formation of a strong mylonitic fabric. The cores of the high strain zones are tectonically brecciated and segmented into low strain blocks surrounded by strong foliation wrapping around the blocks.

3.2 Brittle structures

The ductile D_2-structures are overprinted by a set of semi-brittle structures (D_3). They appear as small-scale faults with discrete tourmaline-coating on the fault surfaces. Typically, D_2-foliation is deflected into the D_3 zones in their vicinity. Distinct slickenside-lineations that developed on the fault planes show the fault kinematics. Brittle high strain zones are characterized by strong cataclastic fabrics with fault gauges and the development of a spaced cleavage. The cataclastic zones inherit a strong strain partitioning with the formation of low strain blocks within the cataclastic fabric. There are several orientations of brittle structures whereas the most dominating ones are gently ESE-dipping fault zones. The slickenside foliations on the fault planes are near to down dip showing a mainly reverse sense of movement with east block up kinematics, hence low-angle thrusting. Also, a lower order set of interlinking relays developed in-between the thrust planes but show steeper orientations than the high order thrusts. Additionally, to the fault-set a network of conjugate joints developed without significant movements. Furthermore, two sets of open fissures formed. One set developed at right angle in-between the low angle thrusts hence representing a tensile opening. Another set forms an en-echelon pattern in the vicinity of reactived shear zones as a response on sinistral reactivation.

3.3 Hydrothermal alteration associations related to structures

Hydrothermal alteration varies in style and intensity within Barsele Central. In the following sections we only provide a macroscopic description of veins related to structures.

Related to the brittle faulting a series of quartz, quartz-calcite, quartz-tourmaline-bearing veins and polymetallic quartz veins were emplaced subparallel with the S_3-fabric (Fig. 2). Quartz vein filling varies from anhedral, massive quartz to euhedral shapes crystallized in open fissures. Mineralogy of veins varies a lot and is not subject to this study. Both S_3-foliated and unfoliated and deflected and undeflected veins are observed. This shows that the majority of veins were emplaced syn-tectonic with D_3-deformation. In the vicinity of D_3 high strain zones, especially associated with these veins, pyrrhotite can be found as selective pervasive alteration in form of disseminated crystals and locally also in small veinlets. Sizes vary from barely macroscopically observable up to 2mm. It is often associated with a more or less intense red staining of the surrounding rocks. Pyrrhotite is in the D_3 high strain zones often accompanied by chalcopyrite. Chalcopyrite can be found both disseminated and as small veinlets. Minor occurrences of sericite, chlorite and calcite alterations were observed together with pyrrhotite within the D_3 high strain zone.

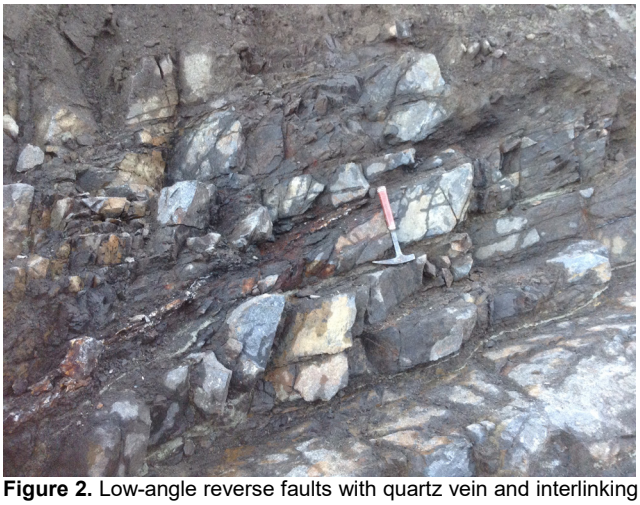

Figure 2. Low-angle reverse faults with quartz vein and interlinking steep faults at Barsele Central.

4 Discussion

The Storuman area was affected by poly-phase deformation events during the Svecofennian orogeny Fig. 3). Comparing the Norra VMS deposit with other VMS deposits in the Skellefte district we suggest that the Norra VMS formed along a syn-extensional normal fault that was later re-activated during basin inversion (c.f. Bauer et al. 2011). This together with the occurrence of alteration minerals around the ductile D_2 shear zones suggest that the ore forming fluids utilized the normal faults as fluid. Nevertheless, later fault re-activation might have resulted in a certain amount of remobilization and potentially further enrichment. The timing of the brittle structures is inferred from the interpretation of the paleo stress direction, the style of deformation and regional-scale relation to late orogenic intrusions and suggested to relate to the regional-scale E-W-compression event (D_3; c.f. Bergman Weihed et al. 1996).

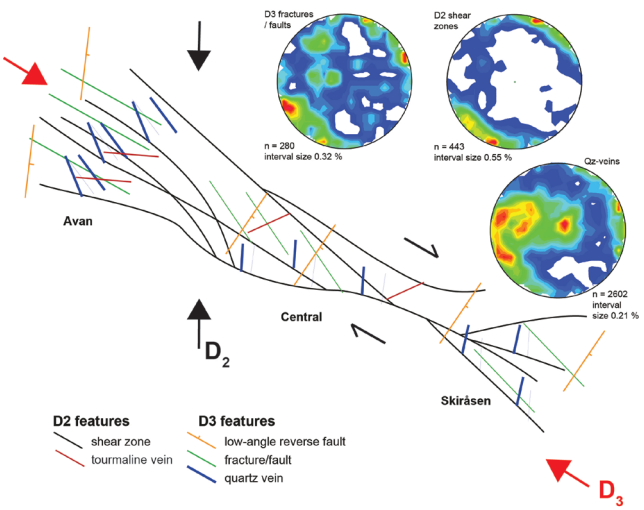

Figure 3. Conceptual structural model of the Barsele area. Lower-hemisphere, equal-area stereographic projections show structures observed in the Barsele Central trench and oriented drill core.

Results suggest a strong structural control on the Au mineralization in Barsele. A combination of kinematic indicators from fault sets indicates that the entire D_3-thrusting was mainly ESE-WNW-directed with a minor sinistral component.

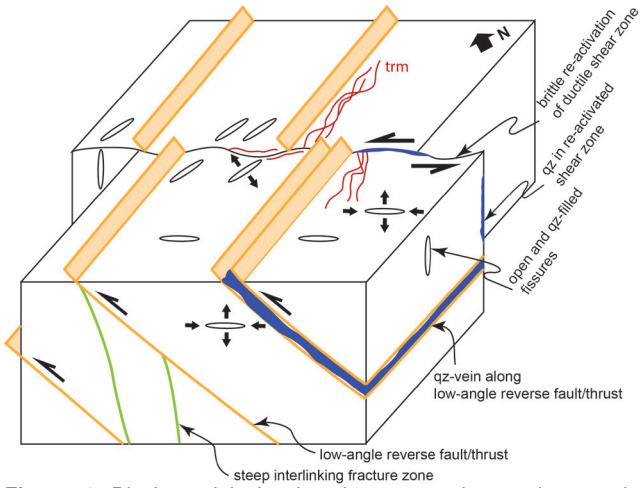

Figure 4. Block model showing the structural controls on vein emplacement in Barsele.

The formation of relays in an oblique, sinistral thrust system can be explained to form in a transpressive Riedel-system where the oblique relays represent synthetic Riedel-shears (R) with also sinistral kinematics. The interpretation as a transpressive Riedel-system goes in line with the occurrence of steep faults that form a part of an imbricate system within the thrust zone (Fig. 4). The host rock to the main gold mineralization is a reologically competent granodiorite; hence, an enhanced competency difference between the supracrustal and intrusive rocks might have favoured the formation of brittle structures within the latter.

When comparing the local and semi-regional geological features of the Barsele Central prospect with the regional geological architecture of the Skellefte district and Storuman area, a close spatial relationship to major approximately N-S-trending high strain zones becomes obvious (Fig. 1). The higher order structure immediate east of the Barsele prospect might represent a major crustal scale, 1st order structure that is interpreted to have the same origin as the known and well-studied Deppis-Näsliden and Vidsel-Röjnorret shear zones in the Skellefte district. Hence, it can be concluded that the 1st order structure east of the Barsele has the same syn-extensional and syn-volcanic origin, forming clearly before or during 1.90 Ga. Additionally, there is an important spatial relationship between the major N-S-trending high strain zones and Au-deposits in the area. All economically important deposits in the area, as Björkdal, Kankberg and Boliden, are located in conjunction to the same style of structures. The orogenic Au-deposits Svartliden, and Fäboliden and the Sjöliden prospect (Bark & Weihed 2007) are related to the same higher order structures as the Barsele prospect showing the high economic importance of this zone.

Acknowledgements

Agnico Eagle Sweden AB is thanked for support, access and discussions. Iain Pitcairn and Glenn Bark are acknowledged for contributions and discussions. This work was partly carried out in the EraMin project “Gold insight”. MOVE was used as part of the Academic software initiative by Midland Valley Exploration Ltd.

References

Allen, R.L., Weihed, P. & Svenson, S.-Å., 1996: Setting of Zn-Cu-Au-Ag massive sulphide deposits in the evolution and facies architecture of a 1.9 Ga marine volcanic arc, Skellefte district, Sweden. Economic Geology 91:1022-1053.

Bark, G., Weihed, P., 2007: Orogenic gold in the new Lycksele-Storuman ore province, northern Sweden; the Paleoproterozoic Fäboliden deposit. Ore Geology Reviews 32:431-451.

Bark, G., Weihed, P., 2012: Geodynamic settings for Paleoproterozoic gold mineralization in the Svecofennian domain: a tectonic model for the Fäboliden orogenic gold deposit, northern Sweden. Ore Geology Reviews 48:403-412.

Bauer, T.E., Skyttä, P., Allen, R.L. & Weihed, P., 2011: Syn-extensional faulting controlling structural inversion – Insights from the Palaeoproterozoic Vargfors syncline, Skellefte mining district, Sweden. Precambrian Research 191:166-183.

Bauer, T.E., Skyttä, P., Hermansson, T., Allen, R.L., Weihed, P. 2014 Comparison of provenance, ore body shape and regional deformation patterns of VMS deposits for mapping the prospectivity in the Skellefte district, Sweden. Mineralium Deposita 19:555-573.

Bejgarn, T., Söderlund, U., Weihed, P., Årebäck, H. & Ernst, R., 2012: Palaeoproterozoic porphyry Cu–Au, intrusion-hosted Au and ultramafic Cu–Ni deposits in the Fennoscandian Shield: Temporal constraints using U–Pb geochronology. Lithos, doi:10.1016/j.lithos.2012.06.015.

Bergman Weihed, J., Bergström, U., Billström, K. & Weihed, P., 1996: Geology, tectonic setting, and origin of the Paleoproterozoic Boliden Au-Cu-As deposit, Skellefte District, northern Sweden. Economic Geology 91:1073-1097.

Eliasson, T., Greiling, R.O., Sträng, T. & Triumf, C.-A., 2001: Bedrock map 23H Stensele, scale 1:50 000. *Sveriges geologiska undersökning Ai 126–129*.

Kathol, B. & Weihed, P., 2005: Description of regional geological and geophysical maps of the Skellefte district and surrounding areas. Geological Survey of Sweden SGU, Ba 57.

Kathol, B., Weihed, P., Antal Lundin, I., Bark, G., Bergman Weihed, J., et al., 2005: Regional geological and geophysical maps of the Skellefte District and surrounding areas. Bedrock map. Geological Survey of Sweden Ba 57:1.

Krispinsson, J., 2018: A GIS-based re-evaluation of the surface geology of the Storuman area, northern Sweden. BSc-thesis, Luleå University of Technology.

Lundström, I., Vaasjoki, M., Bergström, U., Antal, I. & Strandman, F., 1997: Radiometric age determinations of plutonic rocks in the Boliden area: the Hobergsliden granite and the Stavaträsk diorite. In: Lundqvist T (ed) Radiometric dating results 3, Sveriges geologiska undersökning C 830:20–30.

Mellqvist, C., Öhlander, B., Skiöld, T. & Wikström, A., 1999: The Archaean-Proterozoic Palaeoboundary in the Luleå area, northern Sweden: Field and isotope geochemical evidence for a sharp terrane boundary. Precambrian Research 96:225-243.

Skyttä, P., Hermansson, T., Andersson, J. & Weihed, P., 2011: New zircon data supporting models of short-lived igneous activity at 1.89 Ga in the western Skellefte District, central Fennoscandian Shield. Solid Earth 2:205-217.

Skyttä, P., Bauer, T.E., Tavakoli, S., Hermansson, T., Andersson, J. & Weihed, P., 2012: Pre-1.87 Ga development of crustal domains overprinted by 1.87 Ga transpression in the Palaeoproterozoic Skellefte district, Sweden. Precambrian Research 206–207:109-136.

Weihed, P., Billström, K., Persson, P.-O. & Bergman Weihed, J., 2002: Relationship between 1. 90–1.85 Ga accretionary processes and 1. 82–1.80 Ga oblique subduction at the Karelian craton margin, Fennoscandian Shield. GFF 124:163-180.

Witschard, F., 1984: The geological and tectonic evolution of the Precambrian of northern Sweden - a case for basement reactivation? Precambrian Research 23:273-315

The structural control on the gold mineralization at the Galat Sufar South deposit (Block 14, NE Sudan)

Julien Perret[1,2], Julien Feneyrol[1], Rémi Bosc[1], Aurélien Eglinger[2], Anne-Sylvie André-Mayer[2], Craig Hartshorne[3], Emmanuel Abanyin[3]
[1]Arethuse Geology SARL, France
[2]GeoRessources, Université de Lorraine-CNRS, France
[3]Orca Gold Inc., Canada

Abstract: The Galat Sufar South (GSS) gold deposit is an example of the Neoproterozoic gold potential of the Nubian Shield, especially along major sutures and shear zones such as the Keraf shear zone and the Atmur-Delgo suture. This study represents the first published work on the deposit and controls on mineralisation despite its strong gold endowment.

This petro-structural study leads to consider a polyphase deformation history at the GSS gold deposit, from the cryptic D_{1GSS} and the principal D_{2GSS} (early development of the Keraf shear zone at the regional scale) ductile deformation events to the late, post-Keraf shear zone D_{4GSS} brecciation episode. The GSS gold mineralization is critically related to deformation. Indeed, the main D_{2GSS} deformation episode is expressed by both folding and shearing controlling the geometry of the main gold-bearing ore features, from disseminated pyrite to boudinaged quartz and sulphide-dominated veinlets. Later, the D_{4GSS} brecciation is responsible for the formation of a polymetallic ore, potentially resulting from the remobilization of the early mineralization. Therefore, the GSS gold deposit should be ultimately classified as a structurally controlled deposit.

1 Geological setting

The Galat Sufar South (GSS) gold deposit is located within the western Nubian part of the Neoproterozoic Arabian-Nubian Shield (ANS; Fig. 1a), formed during the 850-550 Ma “Supercontinent Cycle” (Stern and Johnson 2010; Johnson et al. 2011). The ANS is one of the world’s promising Neoproterozoic regions for orogenic Au and polymetallic volcanogenic massive sulphide deposit exploration (Plyley et al. 2009; Trench and Groves 2015; Barrie et al. 2016) and contributes to the world resource of Neoproterozoic Au (Johnson et al. 2017; Goldfarb et al. 2017) as attested by probable reserves of 79.9 Mt @ 1.11g/t Au for a total of 2.853 Mozt across both the GSS and Wadi Doum deposits within the Block 14 project area (Orca Gold Inc. 2019).

The GSS gold deposit is located within the northern part of the Keraf shear zone (KSZ), at the junction with the Atmur-Delgo suture (ADS) (Fig. 1a). The N-trending KSZ, surimposed to an arc-continent suture, is interpreted to have formed during the *ca.* 620-580 Ma final assembly of the ANS by four-phased sinistral transpressive tectonics (Almond and Ahmed 1987; Stern 1994; Abdelsalam et al. 1995, 1998; Abdelsalam and Stern 1996; Ahmed Sulliman 2000) while the ADS possibly documents an aulacogenic oceanic re-entrant that used to separate the Halfa and Bayuda terranes (Schandelmeier et al. 1994).

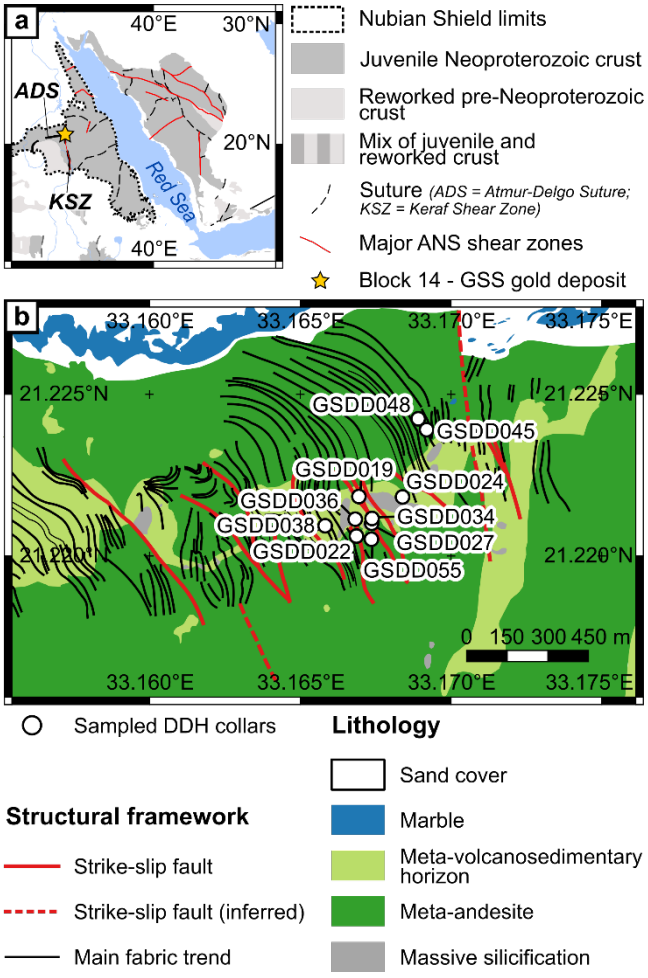

Figure 1. Litho-structural framework of the GSS gold deposit **a** Schematic lithostructural map of the ANS, simplified after Johnson et al. (2011) and Fritz et al. (2013). **b** Lithostructural framework at the GSS gold deposit, adapted after Orca Gold Inc. (2017), and localization of the sampled diamond drill hole collars. Geographic coordinates are reported as WGS 84 / Pseudo Mercator.

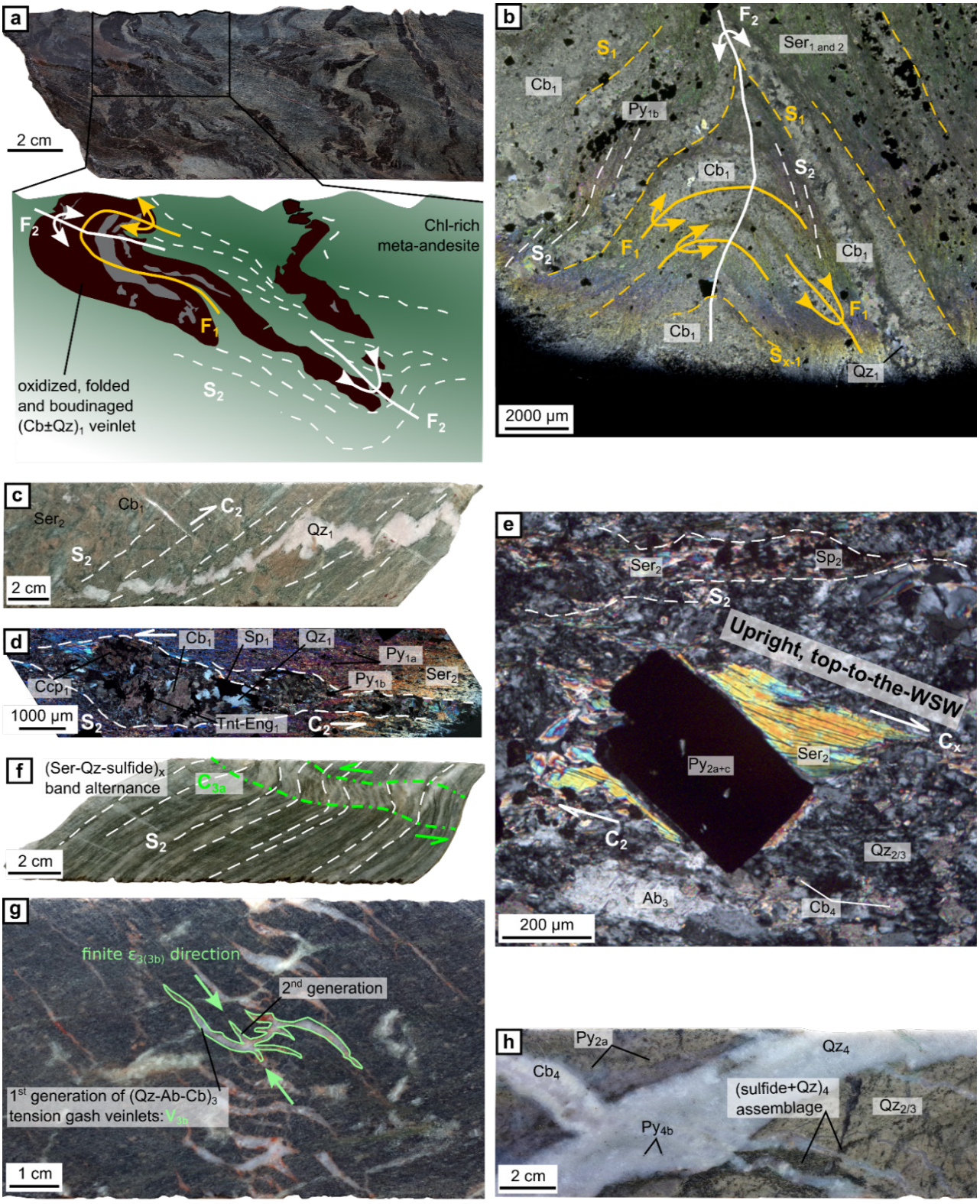

Figure 2. Deformation features related to the successive deformation events that occurred at the GSS gold deposit
a and **b** (cross-polarized, transmitted light) D_{1GSS}-related F_1 folds affecting early carbonate(-quartz) veinlets are transposed along the S_2 main fabric and refolded by the F_2 fold system. **c** C_2 shearing is developed along the S_2 penetrative fabric and affects an early quartz veinlet that is partially transposed along S_2. **d** (cross-polarized, transmitted light) The D_{2GSS}-related C_2 shearing and S_2 development are responsible for early carbonate-dominated veinlet boudinage and asymmetrical dismembering along S_2. **e** (cross-polarized, transmitted light) Ser_2-rich, asymmetrical strain fringes are developed around disseminated Py_2 grains displaying the non-coaxial D_2 shearing sense. **f** Rare D_{3GSS}-related C_{3a} shear bands affect the S_2-dominated gangue. **g** Multiple generations of quartz-albite-carbonate V_{3b} tension gash veinlets highlight the apparent, finite $\varepsilon_{3(3b)}$ orientation. **h** The D_{4GSS} event occurs as quartz-carbonate hydraulic breccia mostly affecting silicified intervals and containing a variable pyrite-sphalerite-chalcopyrite-galena-fahlore amount.

At the shield scale complex interference folding has been identified from satellite imagery within the Keraf meta-sedimentary rocks at the junction between the two regional major structures, the ADS and the KSZ (Abdelsalam et al. 1995, 1998; Abdelsalam and Stern 1996). Within this domain, an andesite dominated antiformal dome complex, host to the GSS deposit, is exposed (Fig. 1b).

At the deposit scale, the GSS gold deposit is hosted by a strongly deformed, interleaved meta-volcanosedimentary horizon, enclosed within a thick andesitic volcanic sequence. The deposit is thought to be "lithologically controlled" as the mineralization is limited to this unit (Davies 2016). Northwards, its extension is limited by a marine carbonate platform (Fig. 1b; Orca Gold Inc. 2017). The host unit has been altered multiple times by the variable addition of albite, sericite, silica and carbonate (Fig. 1b and 2; Orca Gold Inc. 2017). The GSS gold deposit structural framework displays a weakly preserved ENE-trending bedding orientation highlighted by the meta-volcanosedimentary horizon (Fig. 1b). The mostly NNW-trending, dominant, penetrative fabric is parallel to the axial plane of upright tight folds affecting primarily the mineralized unit (Fig. 1b; Orca Gold Inc. 2017).

2 Sampling and methodology

Samples have been collected along several diamond drill cores (Fig. 1b) to provide the most representative dataset about lithology, alteration, deformation and mineralization at the GSS gold deposit. The S_2 penetrative fabric orientation has been systematically measured along the studied drill cores using a "rocket launcher". Oriented thin sections have been prepared when possible.

A detailed petrographic and structural description has been carried out at the macro- and micro-scale to identify (i) the successive deformation stages and (ii) the related paragenetic sequence that occurred at the GSS gold deposit.

3 Results

The main deformation features observed at the GSS gold deposit are illustrated in Fig. 2. Index for mineral generations refers to deformation events in agreement with the paragenetic sequence that is considered.

3.1 Cryptic, ductile D_{1GSS} deformation event

The ductile D_{1GSS} event is weakly expressed at the GSS gold deposit because of strong overprinting by subsequent deformation. Nevertheless, evidence for an early F_1 folding stage has been observed. It occurs as early, up to decimetric, boudinaged to dismembered, carbonate (Cb)-rich veinlets displaying F_1 hinges that are affected by a subsequent F_2 folding episode (Fig. 2a, b). Limbs of these twice-folded veinlets are transposed along the S_2 penetrative fabric that represents the axial plane cleavage related to this fold system (Fig. 2a, b). Rare evidence of a S_1 schistosity is preserved and characterized by sericite flakes folded by the F_2 isoclinal folds with a S_2 schistosity in an axial planar position characterized by the assemblage of sericite-chlorite (Fig. 2b).

3.2 Major, ductile D_{2GSS} deformation event

The D_{2GSS}-related structural features control the global structural framework at the GSS gold deposit. At the deposit scale, the variable, mostly N140°- to N160°-trending S_2 penetrative fabric orientation is controlled by the predominant L_2 stretching lineation steeply dipping northwestwards (Fig. 3). D_{2GSS}-related folds are observed at both macro- and microscopic scales (Fig. 2a, b) and S_2, mostly expressed by the Ser_2-rich gangue in the meta-volcanosedimentary horizon, can be interpreted as F_2 axial plane cleavage (Fig. 2b).

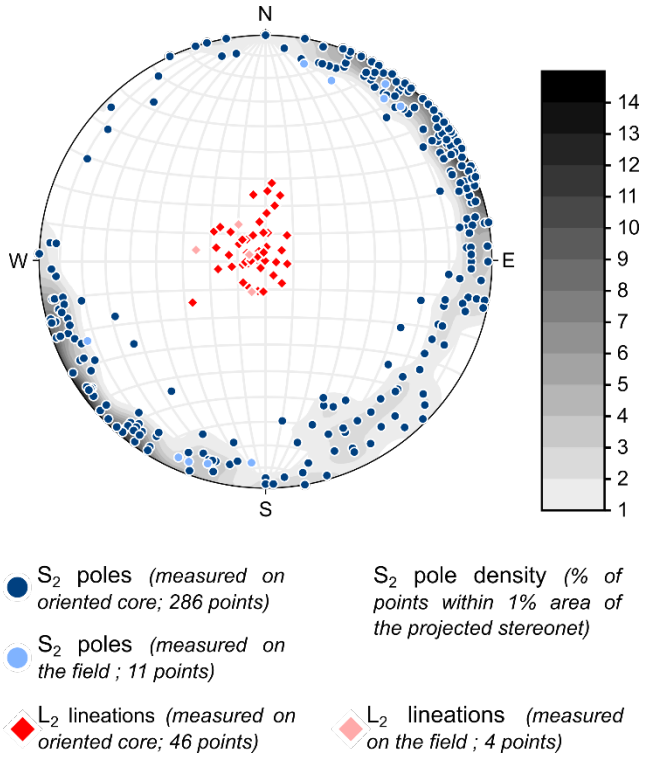

Figure 3. $S_2$and L_2 distribution at the GSS gold deposit. Data are plotted in an equal area stereonet, lower hemisphere projection.

C_2 shearing planes are developed along the S_2 penetrative fabric and earlier veinlets are partially to completely transposed along them (Fig. 2c). Besides, the shape of early, pluri-millimetric to centimetric carbonate(-quartz-pyrite-chalcopyrite-sphalerite-fahlore) veinlets, boudinaged and dismembered along S_2, illustrates the C_2 kinematics (Fig. 2d). The upright top-to-the-WSW C_2 shear sense is even better highlighted by asymmetrical strain fringes composed of variable amount of quartz, chlorite and sericite developed around disseminated, D_{2GSS}-related pyrite grains (Fig.2e). D_{2GSS}-related sulphide income forms the economic mineralization displayed at the GSS gold deposit.

3.3 Weak, ductile/brittle D_{3GSS} deformation event

A minor, ductile/brittle D_{3GSS} event occurred at the GSS gold deposit as pluri-centimetric C_{3a} kink bands postponing the S_2 main fabric (Fig. 2f). The latter are crosscut by pluri-millimetric to pluri-centimetric Qz-albite (Ab) V_{3b} tension gash veinlets (Fig. 2g; the crosscutting relationship between C_{3a} kink bands and V_{3b} tension gash veinlets has been observed on the thin section prepared for the sample visible in Fig. 2g). Therefore, the non-coaxial D_{3GSS} event recorded the syn-albitization ductile/brittle transition at the GSS gold deposit.

3.4 Late, brittle D_{4GSS} deformation event

Finally, a late, brittle D_{4GSS} event predominantly affected the silicified zones within the meta-volcanosedimentary horizon at the GSS gold deposit. The D_{4GSS}-related quartz-carbonate breccia could be interpreted as a hydraulic breccia due to the angular shape and rather constant size of the pluri-centimetric host rock clasts (Fig. 2h). A variable polymetallic sulphide mineralization composed by a pyrite-sphalerite-chalcopyrite-galena-fahlore(-electrum) is associated with these breccia occurrences (Fig. 2h).

4 Discussion

The GSS gold deposit has recorded a complex deformation history from ductile to brittle deformation. The main mineralization event, expressed by disseminated pyrite and quartz and sulphide-dominated veinlets transposed along S_2 is synchronous to the ductile D_{2GSS} event controlling the deposit structural framework. The D_{2GSS} event is also expressing evidence for simple shearing illustrated by asymmetrical strain fringes and dismembered veinlets (Fig. 2d, e) transposed along the main fabric, contrary to the pure shear model considered to date (Mason 2017). The GSS structural framework is dominated by subvertical, steeply NW-dipping L_2 responsible for S_2 variable orientation at the deposit scale. At the regional scale, the D_{2GSS} event could be related to the early KSZ development, *i.e.* the early emplacement of the ANS over the Saharan metacraton (Abdelsalam et al. 1995; Abdelsalam and Stern 1996; Ahmed Suliman 2000), which is expressed by large-scale folds with steep, NW-dipping fold axis. Besides, the D_{4GSS}-related brecciation, affecting mostly silicified intervals within the ore-bearing meta-volcanosedimentary horizon (Fig. 2h), is responsible for polymetallic ore formation, likely to result from the gold and base metal remobilization of the primary ore which remains to be proven. This event probably postdates the KSZ tectonic history as no preferential stress orientation has been deciphered. Although the mineralization is broadly limited to the meta-volcanosedimentary unit (Davies 2016), this study suggests that the genesis of the GSS gold deposit is intimately related to its deformation history.

Acknowledgements

The authors are grateful to the Orca Gold Inc. team for their welcome on GSS camp and their substantial logistical support. This work is part of Julien Perret's PhD project which benefited of a CIFRE funding, reference CIFRE N°2017/17371, attributed by the French National Research and Technology Agency.

References

Abdelsalam MG, Stern RJ, Schandelmeier H, Sultan M (1995) Deformational History of the Neoproterozoic Keraf Zone in NE Sudan, Revealed by Shuttle Imaging Radar. J Geol 103:475-491

Abdelsalam MG, Stern RJ (1996) Sutures and shear zones in the Arabian-Nubian Shield. J Afr Earth Sci 23:289–310

Abdelsalam MG, Stern RJ, Copeland P, Elfaki EM, Elhur B, Ibrahim FM (1998) The Neoproterozoic Keraf Suture in Ne Sudan: Sinistral Transpression Along the Eastern Margin of West Gondwana. J Geol 106:133–148

Ahmed Suliman ETB (2000) Keraf shear zone, NE Sudan: geodynamic characteristics of the Nile Craton - Nubian Shield boundary. PhD thesis, Technischen Universität Berlin, 141pp

Almond DC, Ahmed F (1987) Ductile shear zones in the northern Red Sea Hills, Sudan and their implication for crustal collision. Geological Journal 22:175–184

Barrie CT, Abu Fatima M, Hamer RD (2016) Volcanogenic Massive Sulphide-Oxide Gold Deposits of the Nubian Shield in Northeast Africa. In: Bouabdellah M, Slack JF (eds) Mineral Deposits of North Africa. Springer International Publishing, Cham, pp 417-435

Davies BM (2016) Galat Sufar South – a preliminary interpretationof the trap site environment and beyond. Renaissance Geology, unpublished report for Orca Gold Inc., 58pp.

Fritz H, Abdelsalam M, Ali KA, Bingen B, Collins AS, Fowler AR, Ghebreab W, Hauzenberger CA, Johnson PR, Kusky TM, Macey P, Muhongo S, Stern RJ, Viola G (2013) Orogen styles in the East African Orogen: A review of the Neoproterozoic to Cambrian tectonic evolution. J Afr Earth Sci 86:65–106

Goldfarb RJ, André-Mayer A-S, Jowitt SM, Mudd GM (2017) West Africa: The World's Premier Paleoproterozoic Gold Province. Econ Geol 112:123–143

Johnson PR, Andresen A, Collins AS, Fowler AR, Fritz H, Ghebreab W, Kusky T, Stern RJ (2011) Late Cryogenian–Ediacaran history of the Arabian–Nubian Shield: A review of depositional, plutonic, structural, and tectonic events in the closing stages of the northern East African Orogen. J Afr Earth Sci 61:167–232

Johnson PR, Zoheir BA, Ghebreab W, Stern RJ, Barrie CT, Hammer RD (2017) Gold-bearing volcanogenic massive sulfides and orogenic-gold deposits in the Nubian Shield. South Afr J Geol 120:63–76

Mason R. (2017) Interpretation of structure at Galat Sufar South, from field mapping and drill core data. Tectonite Geology, unpublished report for Orca Gold Inc., 48pp.

Orca Gold Inc. (2017) GSS presentation document, unpublished, 18p

Orca Gold Inc. (2018) www.orcagold.com, consulted on January, 30th 2019

Plyley B, Kachrillo JJ, Bennett M, Bosc R, Barrie CT (2009) Hadal Awatib East Cu-Au VMS Deposit, Sudan Resource Estimates NI 43-101 Technical Report, 105pp.

Stern RJ (1994) Arc Assembly and Continental Collision in the Neoproterozoic East African Orogen: Implications for the Consolidation of Gondwanaland. Annu Rev Earth Planet Sci 22:319–351

Trench A, Groves D (2015) The western Arabian-Nubian Shield; a rapidly emerging gold province. SEG Newsl 101:1

The invincible deposit: an example of pre-orogenic gold mineralization in the eastern Goldfields, western Australia

Sarah Jones
Gold Fields Limited

Abstract. The Invincible Deposit, located in the St Ives camp in the Eastern Goldfields, Western Australia, displays two distinct styles of gold mineralization. Type 1 mineralization comprises steep bedding-parallel quartz breccia veins and these are consistently overprinted by flat-lying to gently dipping Type 2 extension (or dilational) veins. Type 1 veins are strongly folded and boudinaged whereas the gently dipping Type 2 veins are undeformed.

Type 1 mineralized veins are truncated by unaltered conglomerate of the overlying c. 2665 Ma Merougil Formation. In contrast, the undeformed flat-lying extension veins extend into the overlying conglomerate. The Type 1 mineralizing event occurred prior to erosion and deposition of the Merougil Formation and prior to strong east-west horizontal compression and development of the flat-lying Type 2 extension veins.

1 Introduction

Most gold deposits in the Eastern Goldfields Superterrane (EGT) in Western Australia are described as orogenic gold deposits associated with structures formed during horizontal east-west compression (c.f., Groves et al., 1998).

Geochronological studies of mineralized assemblages across the EGT show gold deposition occurred over a period from ~2680 to 2620 Ma which broadly coincides with the timing of D1-4 deformation events (c.f., Czarnota et al., 2010). This indicates that at least some gold deposition occurred during the c. 2672-2660 Ma D1 event.

D1 structures comprise early recumbent folds and an axial planar layer-parallel S1 foliation that is variably developed throughout the EGT (Swager, 1997; Jones, 2014; Jones et al., 2019). D1 structures differ markedly from D2-4 structures as these formed during horizontal east-west compression and comprise upright north-trending folds, a steep axial planar S2 foliation, and D3-4 shears. Some of the larger gold deposits in the EGT display evidence for protracted mineralization during the D1 to D4 events (e.g., Golden Mile, Bateman et al., 2001; Waroonga, Jones et al., 2019).

In the St Ives camp, about 50 km south of Kalgoorlie, most gold deposits are associated with structures that developed during horizontal east-west compression (Figure 1). The Invincible deposit displays structural features that differ markedly from the other deposits in the camp and may be related to the early D_1 event.

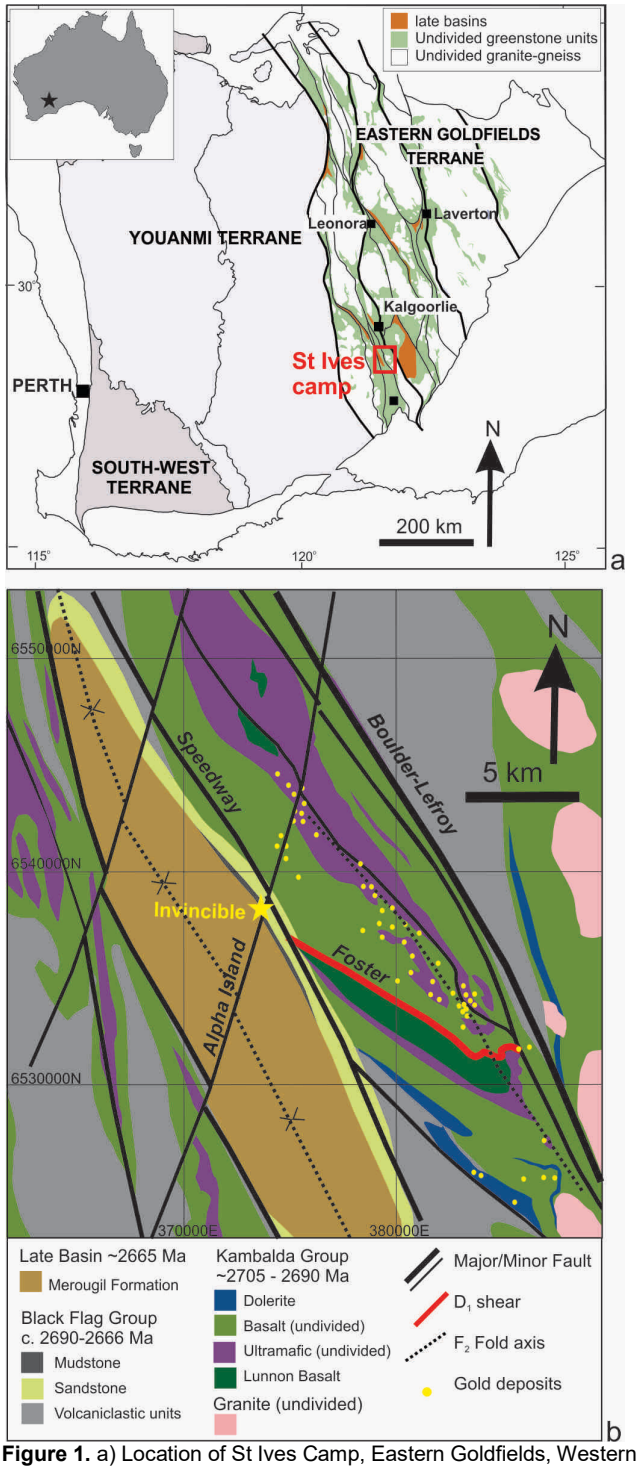

Figure 1. a) Location of St Ives Camp, Eastern Goldfields, Western Australia; b) Geology and structure of the St Ives camp.

2 Regional geological setting

The Invincible deposit, located in the St Ives camp, is in the southern part of the Kalgoorlie Terrane which forms part of the Eastern Goldfields Superterrane (Cassidy et al., 2006). The stratigraphy of the Kalgoorlie-Kambalda area can be broadly grouped into three sequences, with the dominantly mafic and ultramafic flows and interflow sedimentary units of the 2705-2690 Ma Kambalda sequence; the intermediate to felsic volcaniclastic units of the 2690-2670 Ma Black Flag Group; and the siliciclastic units of the c. 2665 Merougil Formation (Barley et al., 2008; Connors et al., 2002; Squire et al., 2010). The Merougil Formation is one of the 'late basins' that lie unconformably on the older sequences throughout the EGT (Figure 1).

Regional deformation events in the EGT comprise: early extension and basin development with deposition of the mafic-ultramafic and later volcanoclastic sequences (D_e); layer-parallel S_1 foliation and recumbent folds (D_1); upright north-trending folds and a steep axial planar S_2 foliation produced during horizontal east-west compression (D_2); continued east-west compression and development of shears along the F_2 fold limbs (D_3); and northeast-southwest directed compression that reactivates earlier structures (D_4).

3 Invincible deposit geology

The Invincible deposit is predominantly hosted by a mudstone unit (upper Black Flag Group) at the eastern edge of the c. 2665 Ma Merougil Basin (Figure 1). The Merougil Formation is tightly folded into a regional north-northwest trending D_2 syncline. The north-northeast trending Alpha Island Fault extends through the center of the deposit and is a large dextral D4 structure but may also represent an early basin controlling structure (Connors et al., 2002).

Mining of the deposit commenced in 2015 and the current resource is 9.2 Mt at 4.5 g/t yielding 1.3 Moz gold. Two distinct styles of mineralization are observed at Invincible, with early steep bedding-parallel Type 1 quartz breccia veins and flat-lying Type 2 extension veins. Type 2 extension veins consistently overprint the steeper Type 1 mineralization.

Type 1 veins are strongly folded and boudinaged and are surrounded by a well-developed sodic alteration halo. Type 2 extension veins are undeformed and are associated with weak sodic and hematite alteration. Type 1 mineralization is best developed in the mudstone, whereas the Type 2 extension veins are best developed in a footwall sandstone unit (upper Black Flag Group). However, the Type 2 veins also overprint the Type 1 mineralization and extend up into the overlying Merougil Formation.

Steep Type 1 ore lenses are consistently truncated by unaltered Merougil Formation conglomerate (Figure 2). The contact is not sheared and there is a 10-20° difference between bedding in the mineralized mudstone and the contact with the overlying conglomerate. In addition, multi-element data such as Sb shows a dramatic change between the altered mudstone and the conglomerate unit (Figure 3).

In weakly mineralized zones, sub-vertical Type 1 extension veins cut across beds that dip 70° to the southwest. In strongly mineralized zones, bedding is sub-vertical and large quartz breccia veins develop along the bedding (Figure 4). Moderately west-dipping shears extend across the bedding in these zones. Bedding-vein relationships indicate southwest-side-down kinematics during the early mineralizing event.

Upright north-trending folds and boudinaged zones are common in the Type 1 veins and suggest that the veins developed prior to strong horizontal east-west compression ($D_{2\text{-}3}$ events). In contrast, the flat-lying Type 2 extension veins are undeformed and likely developed synchronously with the compressional events.

Further examples of polyphase deformation are shown by tightly folded Type 1 extension veins (Figure 5). The extension veins developed above extensional shears during early southwest-side-down movement. The veins are tightly folded by subsequent horizontal compression. In the first deformation phase, the bedding 'opens', then 'closes' during the later compressional event. Early extensional shears are reactivated as reverse shears.

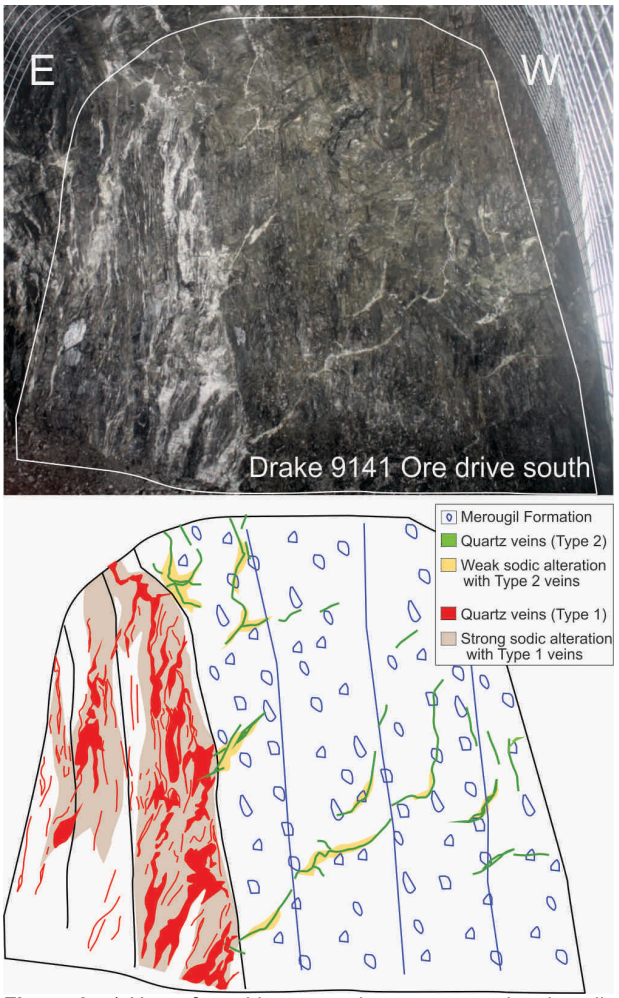

Figure 2. a) Unconformable contact between strongly mineralized mudstone and the overlying Merougil Formation conglomerate (modified from Jones et al., 2019).

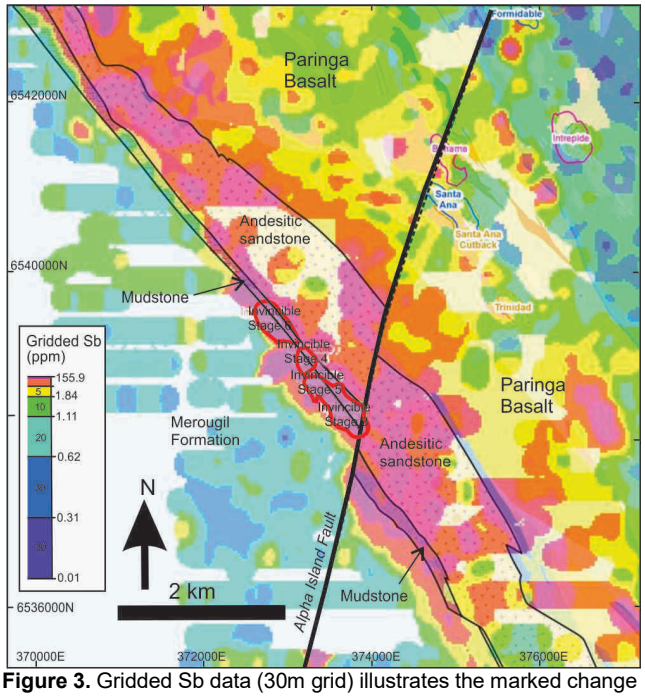

Figure 3. Gridded Sb data (30m grid) illustrates the marked change in Sb values from the altered mudstone to the overlying unaltered conglomerate unit. The mudstone unit dips 70° to the southwest and this accounts for the elevated Sb values to the west of the surface outcrop boundaries.

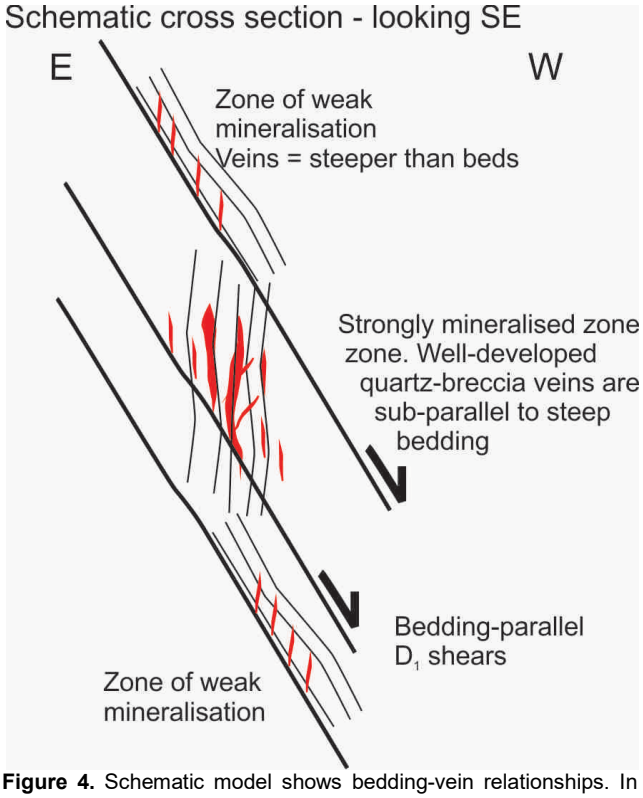

Figure 4. Schematic model shows bedding-vein relationships. In weakly mineralized zones, minor Type 1 extension veins develop steeper than bedding. In strongly mineralized zones, bedding is sub-vertical and large quartz breccia veins develop in the zone of enhanced dilation during south-west-side down movement.

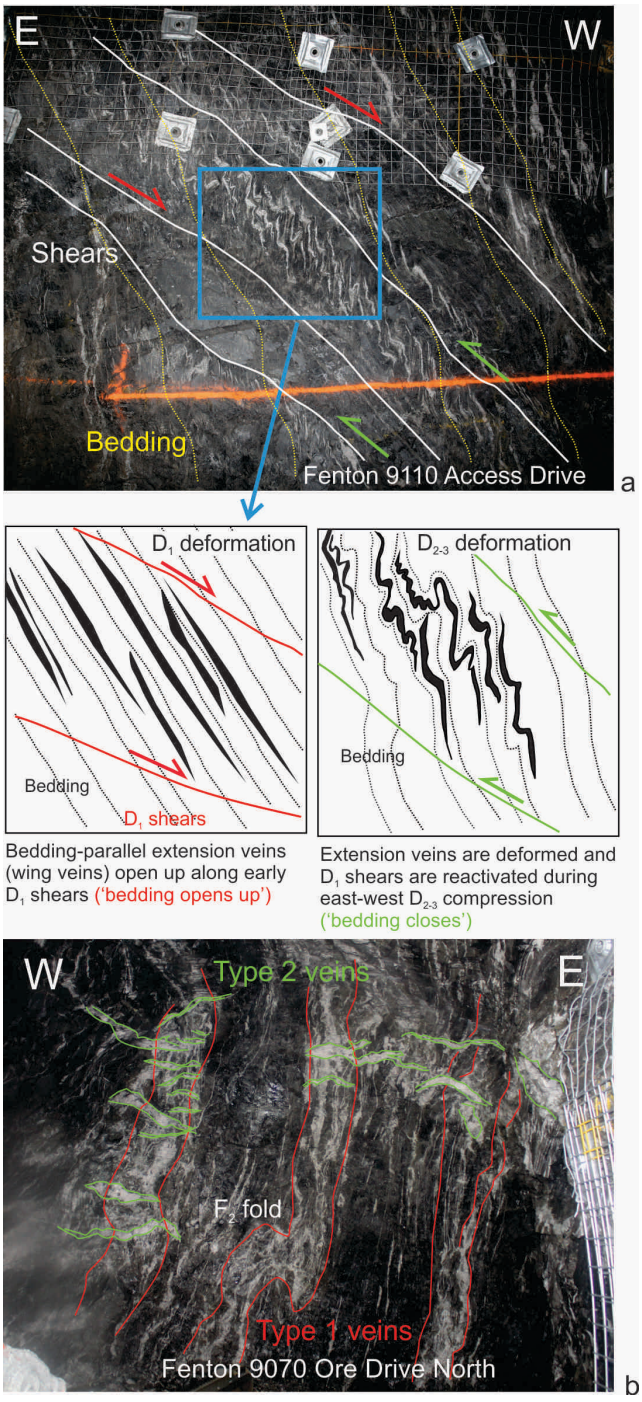

Figure 5. a) Two distinct deformation phases are shown by overprinting relationships. Early southwest-side-down movement is indicated by the orientation of steep bedding-parallel extension veins above the west-dipping shears. These Type 1 extension veins are folded by subsequent compression and the early extensional shears are reactivated as reverse shears. The first event 'opens up' the bedding, the second event 'closes' the bedding; b) flat-lying Type 2 extension veins cut across the steep bedding-parallel Type 1 veins. Note the upright east-verging F_2 fold in the Type 1 veins in the center of the face (modified from Jones et al., 2019).

4 Conclusions

The angular unconformity between the strongly mineralized mudstone and the overlying unaltered Merougil Formation conglomerate indicates that the main mineralizing event occurred prior to erosion and deposition of the conglomerate unit. The lack of alteration in the overlying conglomerate unit is consistent with deposition after the mineralizing event.

The strong modification of Type 1 veins by $D_{2\text{-}3}$ horizontal compression also suggests that the mineralizing event occurred early in the deformation history. Gently dipping Type 2 extension veins consistently overprint the Type 1 mineralization and are not deformed. These veins likely developed during the later compressional events.

Bedding-vein relationships indicate southwest-side down kinematics and the mineralizing event may have occurred during early extension and development of the Merougil Basin.

Acknowledgements

Thanks to all the mine, resource and exploration geology teams for the ongoing field trips and useful discussions. Thanks also to David Doutch for his insightful studies into the Invincible deposit.

References

Bateman R. J., Hagemann S. G., McCuaig T. C. & Swager C. P., 2001. Protracted gold mineralisation throughout Archaean orogenesis in the Kalgoorlie camp, Yilgarn Craton, Western Australia: structural, mineralogical, and geochemical evolution. In world-class gold camps and deposits in the eastern Yilgarn Craton Western Australia, with special emphasis on the eastern Goldfields Province. *In:* Hagemann S. G., Neumayr P. & Witt W. K. eds. 4th International Archaean Symposium. Geological Survey of Western Australia, *Record* **2001/17**:63–98. Perth WA.

Cassidy K. F., Champion D. C., Krapez B., Barley M. E., Brown S. J. A., Blewett R. S., Groenewald P. B. & Tyler I. M. 2006. A revised geological framework for the Yilgarn Craton. *Geological Survey of Western Australia, Record* **2006/8**. Perth WA.

Connors, K.A., Stolz, E.M.G. & Hanneson, J.E., 2002. Early fault architecture at St Ives: implications for Au and Ni mineralisation. In: Vearncombe, S. (ed), Applied structural geology for mineral exploration and mining, V. 36, Australian Institute of Geoscientists Bulletin: 29-31.

Czarnota K., Champion, D.C., Goscombe, B., Blewett R. S. Cassidy, K.F., Henson, P.A. & Groenewald P.B., 2010. Geodynamics of the eastern Yilgarn Craton. Precamb Res, 183: 175-202.

Groves, D.I., Goldfarbb, R.J., Gebre-Mariam, M., Hagemann, S.G., & Robert, F., 1998. Orogenic gold deposits: A proposed classification in the context of their crustal distribution and relationship to other gold deposit types. Ore Geol Rev, 13: 7-27.

Jones S. A. 2014. Contrasting structural styles of gold deposits in the Leonora Domain: Evidence for early gold deposition, Eastern Goldfields, Western Australia. AJES, **61/7**: 881-917.

Jones, S.A., Waters, A. & Ashley, P., 2019. Deformation and mineralisation in the Scotty Creek Basin: Evidence for D1- and D3-related gold mineralisation. AJES, 66, 379-410.

Jones, S.A., Doutch, D. & Lutter, T., 2019. The Invincible Deposit: Early gold mineralisation truncated by unaltered c. 2655 Ma conglomerate, St Ives, Eastern Goldfields, Western Australia. Ore Geol Rev (in press).

Squire R. J., Allen C. M., Cas R. A. F., Campbell I. H., Blewett R. S. & Nemchin A. A. 2010. Two cycles of voluminous pyroclastic volcanism and sedimentation related to episodic granite emplacement during the late Archean: Eastern Yilgarn Craton, Western Australia. Precamb Res **183**:251–274.

Swager C. P. 1997. Tectono-stratigraphy of late Archaean greenstone terranes in the southern Eastern Goldfields, Western Australia. Precamb Res **83**:11–42.

Reverse shear, horizontal shortening and lode-gold mineralisation along the Mougooderra Shear Zone, Western Australia

Jamie J. Price, Tom G. Blenkinsop, Andrew C. Kerr
School of Earth & Ocean Sciences, Cardiff University, UK

Kathryn M. Goodenough
British Geological Survey, The Lyell Centre, Edinburgh, UK

Adrian J. Boyce
Scottish Universities Environmental Research Centre, UK

Clinton Kuehnapfel
Minjar Gold Pty., Golden Dragon Project, 70km S of Yalgoo, Western Australia

Abstract. Exploration for lode-gold deposits in the Archaean Yalgoo-Singleton greenstone belt of Western Australia is difficult, due to widespread, thick transported cover blanketing the bedrock from the surface. This study has employed detailed structural logging of core drilled along the unexposed Mougooderra Shear Zone, primarily from the 400 koz Silverstone deposit, in order to characterize the style of mineralisation present. Structural analyses at Silverstone reveals reverse kinematics of a steep (~65°) west-dipping shear zone, with associated veining of two principal types: foliation-parallel shear veins and extensional flat veins. Mineralisation conforms to the fault-valve model, whereby highly pressured fluids are responsible for reverse shear along a steeply inclined structure. Similar analysis on another deposit on a splay structure also demonstrates fault-valve style mineralisation, suggesting most lode-gold deposits in the belt formed during the same contractional episode. This is supported by preliminary S isotope data. A paragenetic study has revealed two discrete phases of gold associated with arsenopyrite and ullmannite (NiSbS) at Silverstone, associated with intense carbonate alteration in mafic and ultramafic host rocks. A better understanding of mineralisation style and paragenesis will help to provide a revised rationale to underpin exploration in a highly-prospective area.

1 Introduction

The Archaean Yilgarn Craton of Western Australia is recognised as one of the best-endowed geological terranes on Earth, hosting a diverse array of world-class orogenic-lode gold deposits. These lode-gold deposits have a range of common characteristics including a spatial association with regional structures, a distinct structural control and formation from low salinity aqueous-carbonic fluids. Previous research into lode-gold deposits across the craton has focused on the largest and well renowned deposits of the Eastern Goldfields, in the east of the Yilgarn Craton, and not fully investigated mineralisation in lesser endowed, but

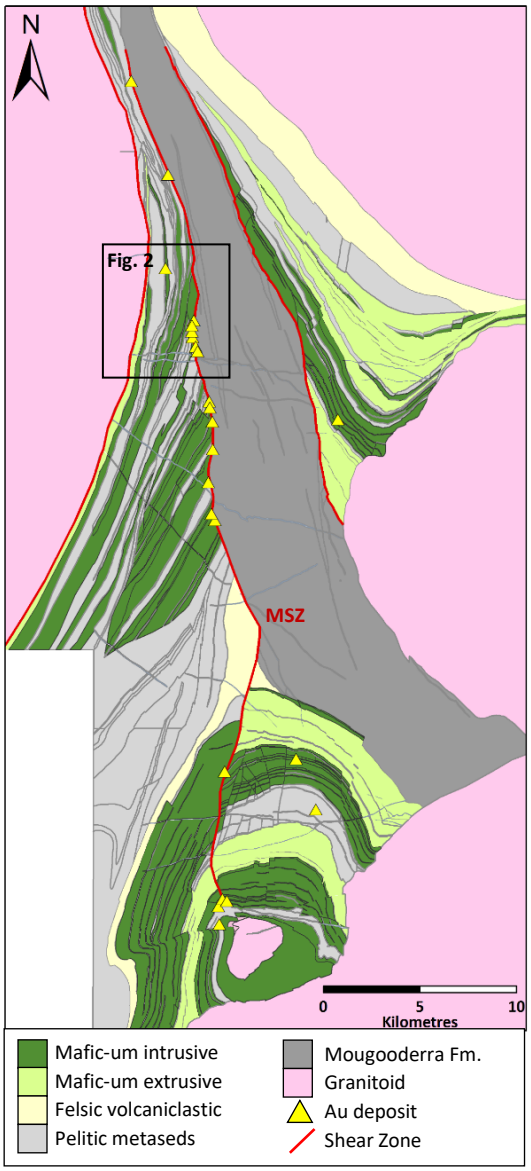

Figure 1. Simplified geological map of the central Yalgoo-Singleton greenstone belt, showing gold deposits, the Mougooderra Shear

Zone (MSZ) and Silverstone deposit. Geology from personal observations, Minjar Gold and GSWA. Extent of figure 2 outlined.

nevertheless, highly prospective areas elsewhere.

The Yalgoo-Singleton Greenstone Belt (YSGB) is situated in the far west of the Yilgarn craton. The belt has a similar stratigraphy and deformational history as the Eastern Goldfields (e.g. Czarnota et al. 2010), but is currently host to fewer discovered gold resources. This may be attributed to minimal (<5%) outcrop, thick transported cover and a high degree of weathering, all of which make for a more difficult exploration environment (Watkins & Hickman, 1990).

Using a combination of structural logging of drillcore, oxide pit observations, and thin section analysis, the kinematics and style of lode-gold mineralisation present in the YSGB has been assessed and the mineral paragenesis determined. Such structural analysis is a crucial means of characterizing mineralisation and host structures, to ultimately aid future exploration in the region.

2 Geological setting

2.1 The Murchison Domain

The Murchison Domain is a relatively understudied region situated in the western part of the Yilgarn Craton, Western Australia. Its geometry represents a typical Archaean granite-greenstone terrane, with thin, north-west trending greenstone belts bound by vast swathes of felsic intrusives (Watkins & Hickman, 1990). The rocks of these greenstone belts record a complex and protracted history, including multiple phases of volcanism and sedimentation from 2960 Ma to 2720 Ma, each followed by deformation, metamorphism and the emplacement of felsic and mafic-ultramafic intrusive complexes (Van Kranendonk & Ivanic, 2009).

Recent structural mapping focused in the northeast of the domain has identified four major deformational events (D1-D4; Van Kranendonk et al. 2013), including a late stage of shearing along N-S structures (D4). The latest deformational phase, D4, is attributed as the main stage of formation of shear-hosted lode-gold deposits in the domain.

2.2 The Yalgoo-Singleton greenstone belt

The Yalgoo-Singleton Greenstone Belt (YSGB) is a ~120 km, north-south trending belt located in the southwest of the Murchison Domain (Fig. 1). The geology of the YSGB consists of multiple folded limbs of Neoarchean (2950-2800 Ma) supracrustal rocks, primarily felsic volcaniclastics and (ultra)mafic volcanics intruded by mafic-ultramafic differentiated sills (Ivanic et al. 2015). These units are overlain by the Mougooderra Formation, which comprises shale, sandstone and minor conglomerate. This undated metasedimentary package is 2-3 km thick and occupies the centre of the belt. The belt is bound my multiple phases of felsic intrusive rocks, and is dissected in the south by a post-tectonic monzogranite (Zibra et al. 2018).

Deformation in the belt is heterogenous, with narrow NNW-trending shear zones dissecting less deformed areas. The largest shear zone present, the Mougooderra Shear Zone (MSZ; Fig. 1), is a concealed ~60 km structure located at the boundary between the Mougooderra Formation rocks and underlying mafic-ultramafic volcanics and intrusives (Watkin & Hickman, 1990). Most discovered lode-gold deposits in the belt are situated along the MSZ, however, very little is known about the geometry and kinematic history of this unexposed structure.

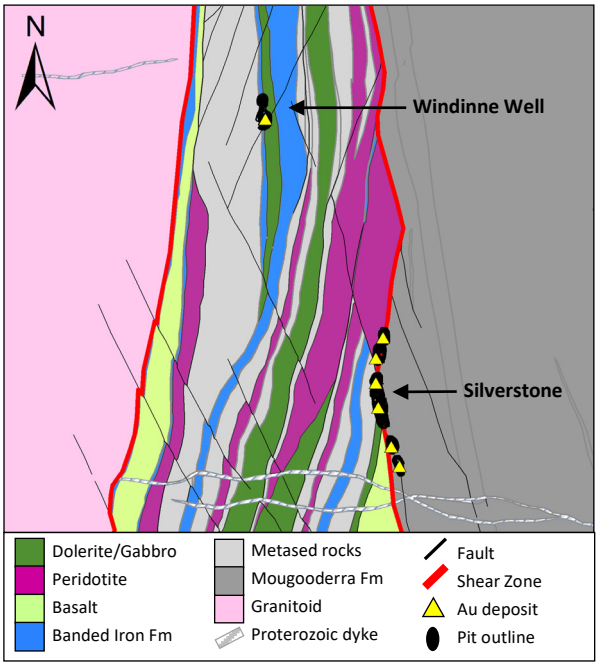

Figure 2. Simplified geological map of the interpreted bedrock geology of the area surrounding the Silverstone and Windinne Well deposits. Geology compiled from personal observations, Minjar Gold and G.S.W.A. See extent in figure 1.

3 Deposit-scale geology

3.1 The Silverstone deposit

The principal focus of this study, the 400 koz Silverstone deposit, is located directly on the MSZ (Fig. 2). The deposit currently consists of six oxide pits, extending 1.6 kilometres along strike, with 10-15 metres of transported cover at the surface. At Silverstone, the MSZ is moderate to steeply west-dipping resulting in a footwall that comprises shales of the metasedimentary Mougooderra Fm, and a hangingwall consisting of mafic-ultramafic units and interbedded shales. The latter units intersect the shear zone at an angle of ~20°, such that the hangingwall varies from ultramafic in the north, to mafic in the south (Fig. 2).

3.1 The Windinne Well deposit

The 100 koz Windinne Well deposit is situated on a N-S trending splay to the west of the MSZ within the greenstone package (Fig. 2). Mineralisation is hosted by

a 25-30 metre thick BIF, steeply east-dipping to vertical and is bound to the east by dolerite, and to the west by volcanogenic metasedimentary rocks.

4 Structural analysis

Structural logging of drillcore has been undertaken in six holes intersecting the MSZ at Silverstone, and three holes at Windinne Well. Measurements have been taken for both planar features (foliations, bedding, veins) and linear features (mineral lineations, vorticity vectors), and corroborated with pit mapping of overlying oxide pits.

4.1 Silverstone

Our structural analyses at Silverstone identify a principal NNW-trending and west dipping (~65°) foliation, confirming the geometry of a metasedimentary footwall and mafic-ultramafic hangingwall to depths of at least 200 metres. In several instances, a steep down-dip mineral elongation lineation is found on foliation planes. Furthermore, a range of kinematic indicators, including quartz σ-clasts, SC fabrics and sheared varioles (Fig. 3), reveal ubiquitous west-side up movement, demonstrating reverse kinematics of the MSZ. This is further supported by younging directions from graded bedding, with 5-10 metre scale isoclinal folding observed in the footwall metasedimentary units, and overturning of hangingwall units as they are transposed into the shear.

Two principal types of veining have been recorded at Silverstone: foliation-parallel shear veins and extensional flat veins. Cross-cutting relationships show a progression from early, foliation-parallel quartz-carbonate veins, to flat quartz-carbonate-sulphide veins and late calcite veinlets.

This vein geometry, along with reverse kinematics of a relatively steeply inclined structure, conforms to the fault-valve model of Sibson et al. (1988), requiring high pore fluid pressures to facilitate movement. In the fault-valve model, such highly pressured fluids develop near the brittle-ductile transition where pore spaces close and create an impermeable zone. Fluid pressure builds below this zone until pressures become high enough to induce failure along pre-existing structures (Sibson et al. 1988).

Some pyrite and arsenopyrite crystals are deformed into the foliation, whereas others occur as euhedral and undeformed crystals, consistent with mineralisation occurring in the late stages of shearing to post-shearing.

4.2 Windinne Well

At Windinne Well, a pervasive, steep (~80°), bedding-parallel foliation has been identified, in addition to a steep down-dip mineral lineation. Kinematic indicators, including sheared sulphide aggregates, demonstrate east-side-up sense of movement and thus near vertical reverse kinematics. Vein orientations are variable, but generally form two groups; bedding/foliation parallel and sulphide-bearing, shallowly inclined veins.

Similarities between Windinne Well and Silverstone deposits suggest they both formed via fault-valve behaviour, possibly as part of the same episode of crustal shortening.

Figure 3. Drillcore from the Silverstone deposit, orientated as in situ (facing north) and showing kinematic indicators: **a.** sheared quartz-carbonate veining showing west-side-up sense of movement, **b.** sheared varioles in a basalt also showing west-side-up movement.

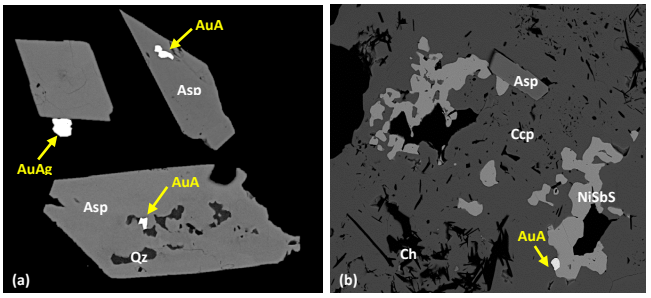

Figure 4. Back-scattered electron (BSE) images of Au-bearing sulphides. **a.** euhedral arsenopyrite crystals containing gold as inclusions or at its margins. **b.** ullmannite (NiSbS) containing Au, itself enclosed in chalcopyrite, with arsenopyrite inclusion.

5 Mineral paragenesis & gold occurrence

Our paragenetic study reveals the sulphide assemblage at Silverstone consists of pyrite, pyrrhotite and arsenopyrite, with minor chalcopyrite and ullmannite (NiSbS). In some parts of the ore zone, the sulphide assemblage is Sb-rich and relatively Fe-poor, with minerals including stibnite (Sb_2S_3), berthierite ($FeSb_2S_3$), chalcostibite ($CuSbS_2$) and ullmannite, in place of the above typical sulphides.

There are at least two discrete gold bearing phases at Silverstone, comprising an early phase of euhedral arsenopyrite crystals (Fig. 4) and a later phase of gold-bearing antimony sulphides, typically ullmannite (Fig. 5). These observations are consistent along strike of the shear zone, with identical textures and associations to those at the Silverstone identified over 30 km south. Accessory minerals associated with gold mineralisation include rutile and monazite (phase 1), and scheelite and apatite (phase 2).

Alteration varies depending on the host protolith. For mafic protoliths, the alteration-assemblage is chlorite-sericite-albite-calcite, whereas in ultramafic protoliths to the north, the typical assemblage is talc-magnesite-fuchsite, with the localized development of listwaenite.

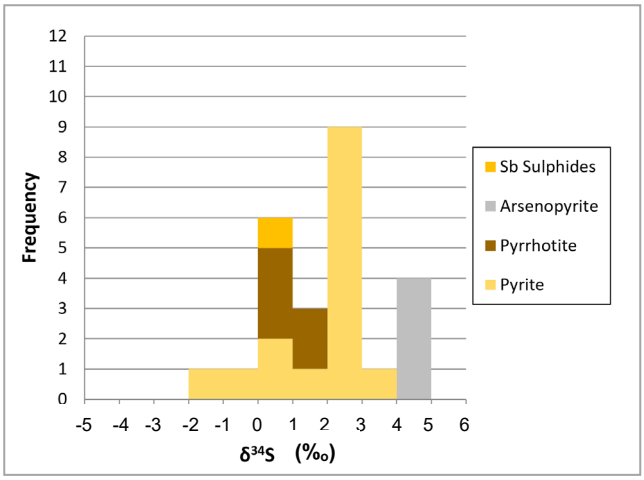

Figure 5. Histogram of preliminary $\delta^{34}S$ isotope data symbolized by mineral phase, showing the distribution of results obtained.

6 Preliminary sulphur isotope analysis

Preliminary conventional sulphur isotope analysis has been undertaken on a range of sulphide minerals from six deposits across the belt, primarily from those situated along the MSZ. A histogram of S isotope composition from samples along the MSZ is shown in figure 5. The collected $\delta^{34}S$ data occupies a narrow range from -1.5 to +4.5 per mil, with most data from 0 to +4.5 per mil.

Four pyrite analyses from barren quartz-sulphide veins return values of +0.5 to -1.5 per mil, in contrast to pyrite associated with Au grade which measures +1.0 to +3.0 per mil. These values appear to be consistent both within the Silverstone deposit, and at other deposits along the length of the MSZ for 30-40 kilometres. Values for gold-bearing arsenopyrite are markedly higher than for pyrrhotite and pyrite associated with mineralisation – this is also consistent across the length of the shear zone.

The consistency of $\delta^{34}S$ isotope data across multiple deposits supports structural analysis which indicates that mineralisation across the belt formed as part of the same contractional episode. It is plausible that variations in pH/fO_2 is causing fractionation of sulphur isotopes as modelled and tested by Ohmoto (1972) and Ohmoto & Rye (1979). It is unlikely that the variability in S isotope composition between earlier Au-bearing arsenopyrite and later pyrite is due to the tapping of multiple reservoirs.

7 Summary and conclusions

Deposits along the main Mougooderra Shear Zone and those on second-order structures display reverse kinematics and fault-valve behaviour, and were likely formed as part of the same episode of crustal shortening. This is currently supported by preliminary S isotope data from deposits across the belt, which shows a consistent signature of +1 to +3 per mil for pyrite associated with mineralisation, and +4.0 to +4.5 per mil for gold-bearing arsenopyrite. Lode-gold mineralisation was emplaced syn-shearing, as demonstrated by deformed sulphide aggregates and boudinaged arsenopyrite crystals. There is currently little evidence for strike-slip/transpressional strains commonly associated with lode-gold mineralisation elsewhere in the Yilgarn Craton.

At Silverstone, the ore zone has experienced intense carbonate alteration in both mafic and ultramafic protoliths, with a sulphide assemblage dominated by pyrite, pyrrhotite and arsenopyrite, but notably with an enrichment in Sb-bearing minerals. Two phases are directly associated with gold, comprising an early phase of arsenopyrite, and a later phase of gold associated with ullmannite (NiSbS).

Structural logging and analysis of oriented drillcore remains a crucial tool for understanding the geometry and style of mineralisation, especially in areas such as the Australian mid-west, where outcrop is minimal to non-existent.

Acknowledgements

The authors acknowledge the support of Minjar Gold for providing access to drillcore, in addition to accommodation and logistical support during fieldwork. JP is supported by a NERC GW4+ Doctoral Training Partnership studentship from the Natural Environment Research Council [NE/L002434/1]. JP acknowledges the generous support of an SEG-CF grant towards fieldwork costs. Many thanks to Mrs. Alison McDonald for help during conventional S isotope analysis.

References

Czarnota, K., Champion, D.C., Goscombe, B., Blewett, R.S., Cassidy, K.F., Henson, P.A. & Groenewald, P.B. (2010). Geodynamics of the eastern Yilgarn Craton. Precam Res 183:175–202.

Ivanic, T.J., Li, J., Meng, Y., Guo, L., Yu, J., Chen, S.F., Wyche, S. & Zibra, I. (2015). Yalgoo 1:100 000 Geological Series Sheet 2241 (First edition). Geological Survey of Western Australia, map.

Ohmoto, H. (1972). Systematics of sulfur and carbon isotopes in hydrothermal ore deposits. Econ Geol, 67(5):551-578.

Ohmoto, H. & Rye, R.O. (1979). Isotopes of sulfur and carbon. In Barnes, H.L. (Ed.), Geochemistry of hydrothermal ore deposits (Second Edition), John Wiley & Sons, New York. 509-567.

Sibson, R. H., Robert, F., & Poulsen, K. H. (1988). High-angle reverse faults, fluid-pressure cycling, and mesothermal gold-quartz deposits. Geology, 16(6):551-555.

Van Kranendonk, M.J. & Ivanic, T.J., (2009). A new lithostratigraphic scheme for the northeastern Murchison Domain, Yilgarn Craton. Geological Survey of Western Australia, Annual Review 2007-08:34-53.

Van Kranendonk, M.J., Ivanic, T.J., Wingate, M.T.D., Kirkland, C.L. & Wyche, S. (2013). Long-lived, autochthonous development of the Archean Murchison Domain, and implications for Yilgarn Craton tectonics. Precam Res 229:49-92.

Watkins, K.P. & Hickman, A. H. (1990). Geological Evolution and Mineralisation of the Murchison Province - Western Australia, Geological Survey of Western Australia: Bulletin 137:267.

Zibra, I., Peternell, M., Schiller, M., Wingate, M.T.D., Lu, Y. & Clos, F. (2018). Tectono-magmatic evolution of the Neoarchaean Yalgoo Dome (Yilgarn Craton). Report 176; Geological Survey of Western Australia. 43pp.

Stratigraphic and structural controls on Carlin-type mineralization in central Yukon (Canada)

Nicolas Pinet, Patrick Mercier-Langevin, Denis Lavoie, Benoit Dubé
Geological Survey of Canada, Canada

Patrick Sack
Yukon Geological Survey, Canada

Julia Lane
ATAC Resources limited

Abstract. Late Cretaceous Carlin-type mineralization at the Conrad prospect in central Yukon (Canada) is mainly hosted in Neoproterozoic limestone (and in a lesser amount in calcareous siltstone) in the core of a doubly-plunging anticline. The limestone unit is in fault-contact to the north and in stratigraphic contact to the south with non-calcareous siliciclastic units with low porosity and permeability. The upper part of the limestone unit that consists of lime mudstone, packstone, floatstone (deposited as debris flows) and calcareous siltstone and shale played an important role in channeling fluid flow. In more massive lithologies, fractured and brecciated intervals also focused fluid flow via the selective replacement of irregular and often complex pre-mineralization vein sets that were preferentially dissolved by acidic fluids early in the mineralizing process. Multiple feedback effects between sedimentologic, hydrothermal and tectonic parameters resulted in complex ore shapes and variable mineralization styles.

1 Introduction

Carlin-type deposits are formed from fluids often described as 'passive' or 'opportunistic' because the fluids are interpreted to have exploited a variety of pathways (Cline et al. 2005; Muntean 2018). The opportunistic nature of the fluids is mainly due to the relatively shallow depth (a few kilometres at most) of mineralization which results in a wide variety of ore zone shapes at the deposit scale.

In central Yukon, recently discovered Carlin-type orebodies are for the most part concordant with lithologic units at property scale (Tucker et al. 2018; Pinet et al. 2018; Pinet and Sack 2019). Orebody geometries are however more complex in detail and correlation between drill holes located a few tens of metres apart can be problematic. This study presents a reappraisal of the geometry and mineralization characteristics of the Conrad prospect. A similar approach for the nearby Sunrise prospect has been reported in Pinet and Sack (2019).

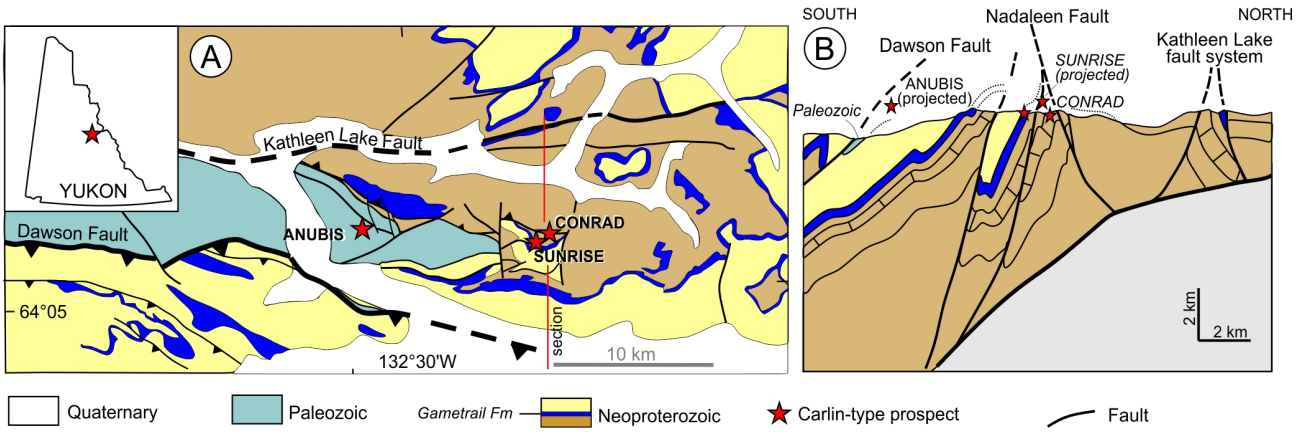

Figure 1. a. Geological map (simplified from Moynihan 2016). **b.** cross-section of the eastern Rackla belt in east-central Yukon

2 Geological setting

Carlin-type gold prospects of central Yukon are located in the Rackla belt, a 5-15 km-wide fault and fold belt bounded to the north by the Kathleen Lake Fault and to the south by the Dawson Fault (Fig. 1A). The Racka belt roughly coincides with the paleogeographic boundary between the Selwyn Basin and the Olgivie/MacKenzie Platform during the Neoproterozoic and part of the Paleozoic (Fig. 1A). This spatial coincidence suggests that depositional patterns were controlled by a major, long-lived, probably deep-seated, structure that may have been reactivated during mountain building. The succession is complexly folded and faulted (Fig. 1B) and experienced several phases of deformation (Steiner et al. 2018). Major faults have been interpreted as thrusts or backthrusts, but most of them bear a significant strike-slip component.

Carlin-type gold prospects in the eastern Rackla belt form the Nadaleen trend. Gold mineralization is predominantly hosted in Neoproterozoic limestones (with few mineralized intervals in siltstones) belonging to the Nadaleen and Gametrail formations (Windermere Supergroup; Moynihan, in press) and in mid-Paleozoic calcareous siltstones. The Conrad and Sunrise-Osiris prospects (cumulative inferred resource of 12.4 Mt at 4.23 g/t Au, 1.69 Moz Au: Atac resources website) exhibit characteristics consistent with Carlin-type mineralization including: i) host-sediments deposited in slope to base of slope settings; ii) alteration that includes partial to complete decalcification of mineralized intervals, and local silicification and argilization; iii) the 'invisible' nature of gold which occurs as rims of Au-bearing arsenian pyrite on pre-ore pyrite or as sub-micrometer particles; iv) the association of gold with Tl, As, Hg, Sb; v) the low base metal and Ag content (Tucker et al. 2018; Pinet and Sack 2019; Sack et al. 2019).

3 Conrad prospect

The Conrad gold prospect is one of the Neoproteroic-hosted prospects in the eastern Rackla belt (Fig. 1). The host limestone unit forms the core of a doubly-plunging anticline and is in fault-contact to the north and in stratigraphic contact to the south with non-calcareous siliciclastic rocks with low porosity and permeability.

The oldest sedimentary unit is a vari-coloured thinly laminated mudstone and siltstone with quartz pebble conglomerate intervals. This unit is regionally correlated with the Ice Brook Formation (Moynihan et al., in press) and is found in the hanging-wall of the Nadaleen Fault, structurally overlying the Conrad prospect. The Nadaleen Fault is an east-striking, steeply- north-dipping (65˚) fault with a damage zone up to several tens of meters in thickness.

In the footwall of the Nadaleen Fault, the limestone unit is a medium grey lime mudstone/wackestone (Fig. 2A) with some packstone (and minor grey to black siltstone). Toward the top of the limestone unit, close to the contact with stratigraphically overlying siliciclastic rocks, the succession is more diverse (Fig. 2B) and includes lime mudstone, packstone, floatstone and calcareous siltstone. Floatstone intervals (Fig. 2C) correspond to matrix-supported sedimentary breccia with angular fragments interpreted as debris flow deposits formed on a carbonate slope. Both the host limestone and the stratigraphically overlying siliciclastic rocks in the footwall of the fault are correlated with the Nadaleen Formation (Moynihan, in press).

Though the limestone host unit is poorly exposed, there is evidence of complex folding and faulting. Observations from diamond drill core indicate that the deformation style varies with rock competency. In the more massive and competent intervals, multiple generations of calcite (±dolomite/quartz) veins may locally represent up to 20% of the rock volume. In the more thinly bedded and less competent intervals, shearing on bedding planes and bed-restricted fractures predominate.

4 Mineralization

In the Conrad prospect, ore bodies are mainly hosted in: i) the steeply-dipping upper part of the limestone unit, close to its contact with stratigraphically overlying siliciclastics; ii) in the immediate footwall of the Nadaleen Fault; and iii) close to fault intersection zones (Fig. 3). Mineralized intervals are documented for 800 m along strike and to a minimum depth of 500 m. Contacts of mineralized zones are sharp and gold grades decrease from several ppm to background values in a few meters at most. Bedding is still visible close to, or even within, mineralized intervals.

Realgar and orpiment (±fluorite) are generally good visual guides for gold mineralization in the Conrad prospect. These minerals often post-date the main stage of gold mineralization. However, the spatial association of realgar and orpiment with gold mineralized intervals strongly suggests that these minerals formed in the late stage of a single event, not during a distinct hydrothermal pulse.

Decalcification is the main alteration type associated with gold mineralization and resulted in a significant increase of the rock porosity (Fig. 2H). The intensity of decalcification varies strongly, with some decimeter-scale intervals still reacting with HCl a few centimeters from decalcified ore segments. Silicification and argilization are more discrete alteration styles.

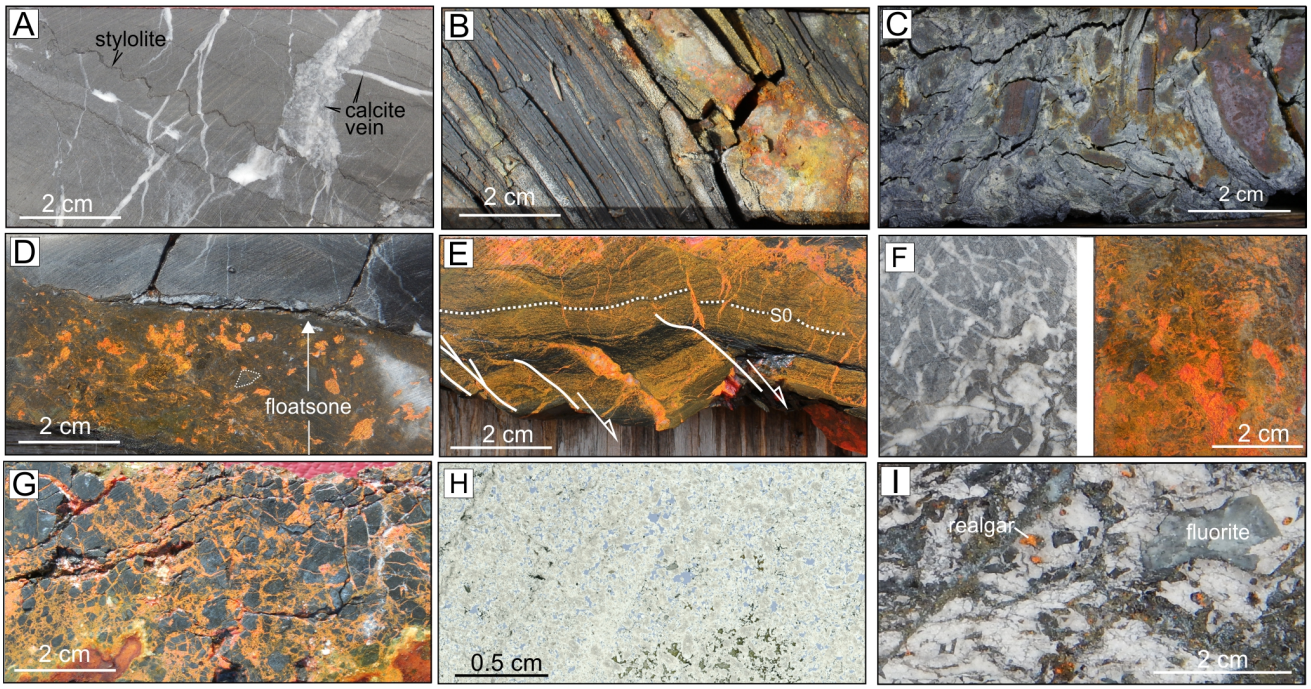

Figure 2. Lithology, mineralization and alteration, Conrad prospect. Orange colors correspond to realgar. **a.** Typical lime mudstone interval with bedding parallel stylolites and several generations of calcite veins. **b.** mineralized alternation of finely laminated limestone and calcareous mudstone. **c.** mineralized matrix-supported floatsone interval. **d.** stratigraphic contact between a mineralized floatsone interval and barren limestone. **e.** realgar replacement of selected limestone beds and filling fractures and minor faults at high angle to bedding (S0). **f.** comparison between barren limestone with complex calcite vein sets predating the ore fluid event and a mineralized breccia. **g**. mineralized hydrothermal breccia with angular limestone clasts in a realgar-rich matrix**. h.** Thin section showing the increase in porosity (blue epoxy) due to decalcification. **i.** Mineralized gabbroic dyke with realgar and fluorite.

At the macroscopic scale, gold mineralization styles vary significantly, even in the same mineralized interval. These styles include selective replacement of mm- to cm-thick beds (Fig. 2E), mineralized fractures at high angle to bedding (Fig. 2E), preferential mineralization of matrix-supported floatstone intervals (Fig. 2D), dark, almost featureless decalcified intervals (high matrix-content debris flow deposits?), irregular veining associated with brecciated intervals and hydrothermal breccia (Fig. 2G).

A 0.25-4 m thick gabbro dyke is intersected in drill holes, in the footwall of the Nadaleen Fault. Assays from this Upper Cretaceous dyke (74.1 ± 1.0 Ma, Tucker et al., 2018) are commonly >1 g/t and the dyke is altered with realgar and fluorite (Fig. 2I). This evidence has been used to provide an older age limit for mineralization (Tucker et al. 2018). Recent LA-ICPMS U-Pb results on hydrothermal calcite associated with mineralization allow narrowing this time constraint and show that dyke intrusion was (within age uncertainties) syn-mineralization (Davis et al. 2019).

5 Discussion

In the Conrad prospect, the limestone unit forms a tight domal feature that constitutes a four way dip closure fold/fault trap for mineralizing fluids. The two low-permeability mudstone/siltstone units in fault (to the north) and stratigraphic (to the south) contact with the limestone acted as prospect-scale aquitards and exerted a first order control on fluid flow. Lithologic and structural parameters provided second-order control that resulted in complex ore shapes and variable mineralization styles (Fig. 3).

Interbedded lime mudstone, packstone, floatstone and calcareous siltstone in the upper part of the limestone unit are the most favourable host rocks for mineralization. A strong lithological control was also noted in the Sunrise prospect in which floatstone intervals are major hosts (Pinet and Sack 2019). Fracture density also influenced fluid flow. In most cases, fractures predate mineralization and highly fractured intervals are linked to specific beds, fault damage corridors or fold hinge zones. Fractures were infilled with several generations of calcite and dissolution of calcite by acidic, early stage mineralizing fluids resulted in increased porosity and permeability (Fig. 2H) which focused later gold-bearing fluids.

The factors favouring gold mineralization should not be considered separately as sedimentologic, hydrothermal and tectonic parameters show feedback effects which have resulted in complex ore shapes (Fig. 3).

Acknowledgements

ATAC Resource Ltd is thanked for the tremendous logistical and scientific support. This is a contribution to Natural Resources Canada's Targeted Geoscience Initiative Program, Gold Project.

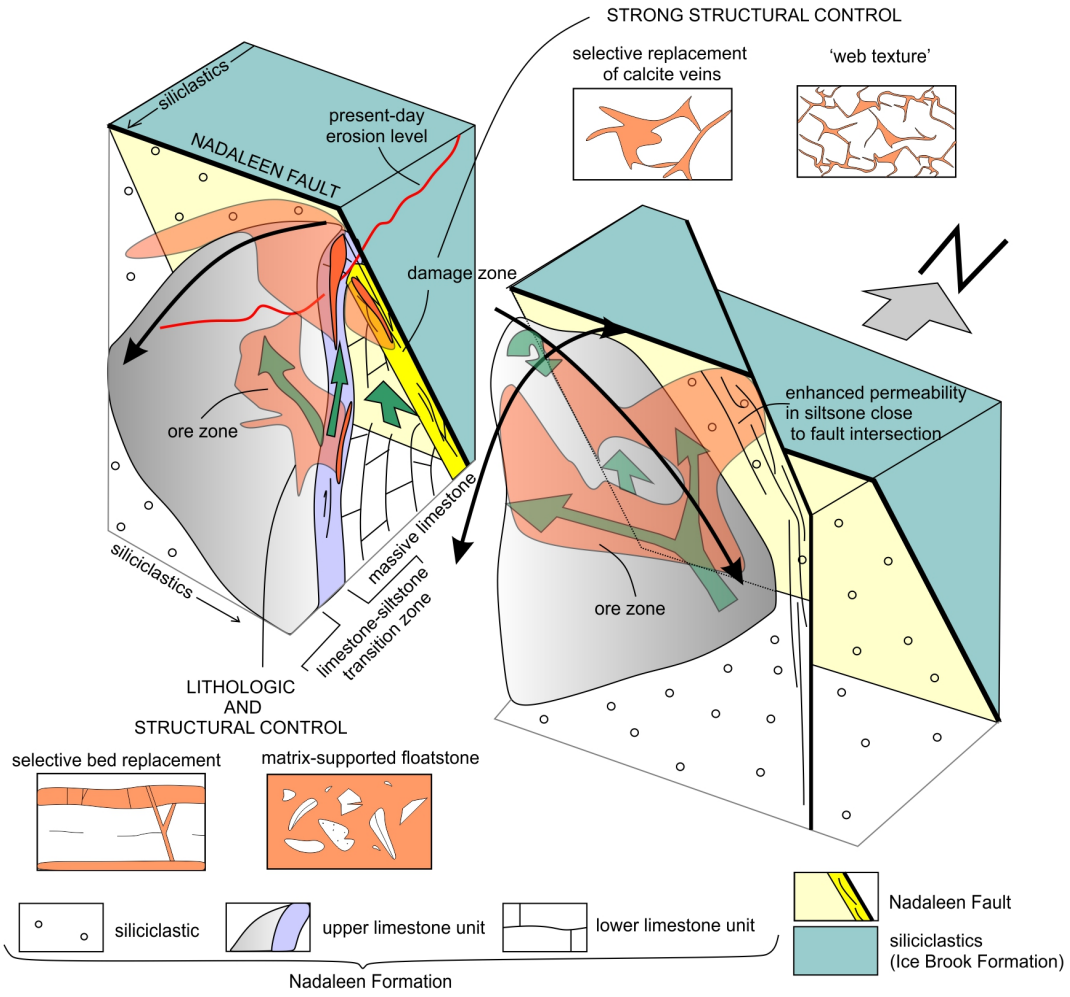

Figure 3. Schematic 3D view of the Conrad prospect. The shape of ore bodies (in orange) are schematic and mineralizing fluid pathways (green arrows) are interpretative. The internal geometry of the limestone unit is simplified and second order structural features are omitted for clarity.

References

Cline, J.S., Hofstra, A.H., Muntean, J.L., Tosdal, R.M., Hickey, K.A. (2005) Carlin-type gold deposits in Nevada: critical geologic characteristics and viable models. Econ. Geol., 100:451–484.

Davis, W.J., Pinet, N., Pettes, D.C., Jackson, S.J., Mercier-Langevin, P. (2019) U-Pb ages of hydrothermal calcite associated with Carlin-type mineralization, Nadaleen trend, north-central Yukon. Abstract, Geol. Ass. Canada annual meeting.

Moynihan, D. (2016) Bedrock geology compilation of the eastern Rackla Belt, NTS 105N/15, 105N/16, 105O/13, 106B/4, 106C/1, 106C/2, east-central Yukon. Yukon Geological Survey Open File 2016-2, scale 1:75 000.

Moynihan, D., Strauss, J.V., Padget, C.D., Nelson, L.L., in press, Upper Windermere Supergroup and the transition from rifting to continent-margin sedimentation, Nadaleen River area, northern Canadian Cordillera: Geol. Soc, Am. Bull.

Muntean, J., (2018) The Carlin gold system: Applications to exploration in Nevada and beyond. In Muntean, J. (ed) Diversity of Carlin-style gold deposits, Reviews in Economic Geology v. 20. Soc. Econ. Geol., p. 39-88.

Pinet, N., Sack, P. (2019) Macroscopic control on Carlin-type gold mineralization in north-central Yukon. In: Targeted Geoscience Initiative: 2018 report of activities, N. Rogers (ed), Geological Survey of Canada Open File 8549, p. 89-103.

Pinet, N., Sack, P., Mercier-Langevin, P., Lavoie, D., Dubé, B., Lane, J., Brake, V. (2018) Breccia styles and controles on carbonate replacement type ('Carlin type') gold zones, Rackla belt, east-central Yukon. In Rogers, N. (ed.), Targeted Geoscience Initiative – 2017 Report of Activities: Geological Survey of Canada, Open File 8358, p. 163–168.

Sack, P., Cline, J., Ren, M., Pettes, D., Pinet, N. (2019) Gold bearing pyrite in Carlin-type gold prospects of the Nadaleen trend, Yukon. Geol. Ass. Canada annual meeting.

Steiner, A., Hickey, K., Coulter, A.B. (2018) The structural framework for Carlin-type gold mineralization in the Nadaleen trend, Yukon. In MacFarlane K.E. (ed) Yukon Exploration and geology 2017, Yukon Geological Survey, p. 139-149.

Tucker, M.J., Lane, J.C., Hart, C.J.R. (2018) Overview of Carlin-type prospects of the Nadaleen trend: a Yukon analogue to Carlin-type gold mineralization of the Great Basin. In Muntean J. (ed) Diversity of Carlin-style gold deposits: Reviews in Economic Geology v. 20. Soc. Econ. Geol., p. 235-256.

Structural controls on ore formation at the Zaozigou gold-antimony deposit, West Qinling, China

Duncan C. McIntire[1], Kunfeng Qiu[1,2], Haocheng Yu[2], Zongyang Gou[2], Richard J. Goldfarb[1,2], Zhaoshan Chang[1]
[1]*Colorado School of Mines*
[2]*China University of Geosciences*

Abstract. Assessing the structural evolution of the large Zaozigou gold-antimony deposit in the context of the tectonic evolution of the Triassic West Qinling orogen can resolve important gaps in our understanding of the deposit formation.

Porphyritic ca. 250-215 Ma dacite intrusions intruded Triassic slates along existing planar features. Reaction skarns within the compositional layers of the slates, along with the loss of macroscopic foliation and genetic textures indicate contact metamorphism caused by the intrusions. As a the slates proximal to the intrusions became increasingly brittle and notably susceptible to faulting and fracturing.

Field relationships of local structures at the mine-scale indicate initial brittle faulting in a N-S orientation under a compressive regime, Shallow E-W striking faults are cut by steeply dipping ENE-striking faults, which in turn are cut by NE striking shallow faults, which are cut by a generation of NW striking shallow faults. All four fault generations are significant ore-bearing structures.

The relative timing of faults in the context of the northward convergence of the South China Block relative to the North China Block suggests that the ore-hosting structures at Zaozigou evolved through progressive counterclockwise rotation of the local principal stress axis. This was facilitated by dextral strike-slip movement along the regional Xiahe-Hezuo fault.

1 Introduction

The Zaozigou gold-antimony deposit in Gansu Province, China, is the largest actively producing gold deposit (118 t Au) in the southwestern domain of the West Qinling Orogen (Qiu and Deng 2017; Sui et al. 2019; Yu et al. 2019). The deposit is hosted by Triassic slates and, to a lesser degree, intrusive porphyritic dacite dikes. Gold is hosted within fault-hosted quartz+stibnite±dolomite lodes as well as in wallrock alteration haloes up to 20m wide. Wallrock alteration is dominantly sericitic, with illite and muscovite as the main alteration minerals. Chlorite and carbonate minerals are less abundant and minor wallrock silicification is common. Wallrock alteration also includes disseminated arsenopyrite, pyrite, and stibnite, typically as selvages to quartz±sulfide veinlets. Textural evidence indicates that disseminated mineralization precipitated through sulfidation reactions between hydrothermal fluids and iron-rich mineral phases (biotite, chlorite).

Previous studies have described the meta-sedimentary ore-hosting rocks as silicified slates, as these rocks retain their compositional layering, but are notably more competent and less fissile than their unaltered slates located 2 km from the mine site. The "silicified" slates are only found in proximity to the Triassic dacite dikes in the area, which could suggest that magmatic-hydrothermal fluids had been responsible for the silicification of the slates. However, bulk rock geochemistry shows no significant increase in silica concentration over unaltered slates. Additionally, petrographic and infrared studies indicate of cordierite, scapolite, and andalusite are present solely in the "silicified" slate. It is therefore more likely that the influence of the Triassic intrusions was a thermal pulse leading to contact metamorphism of the slates and ultimately increasing the propensity for brittle deformation.

2 Structural controls on mineralization

The six most significant orebodies (M4, Au9, Au1, M7, M6, and M9) are manifest as quartz+stibnite±dolomite reverse fault-hosted lodes and veins. The hosting structures have been extensively measured and organized in the present study according to field observations of crosscutting relationships. The main faults are irregular,and typically 1-3m in width, although associated with narrower subsidiary faults with similar strike orientation but extremely variable dips. The fault margins commonly are characterized by brecciation. Primary quartz+stibnite±dolomite is hosted discretely within the bounds of major and minor faults and related veinlets. Mineralization is manifest as massive quartz and stibnite laminated lode veins with minor sulfidation of wallrock breccia clasts found within faults. The lode veins are juxtaposed with bleached wallrock alteration haloes up to 20m wide. Alteration is associated with disseminated arsenopyrite, pyrite, ±stibnite which is found in the highest proportions immediately adjacent to the primary-ore-hosting faults.

The orientation of structures follows a counter-clockwise rotation from initial E-W striking structures to eventually NW-SE oriented structures (Fig. 1), in total representing a rotation of strike of 140°. However, the youngest generation of faulting may be associated with a separate tectonic event. If this is the case the fault orientations would have progressively rotated ~60° in a counter-clockwise direction. Microtextural relationships of stibnite within primary fault-hosted orebodies indicates syn-kinematc precipitation of stibnite. This would indicate ongoing sulfide mineralization of faults during the rotation of the major axis of compression.

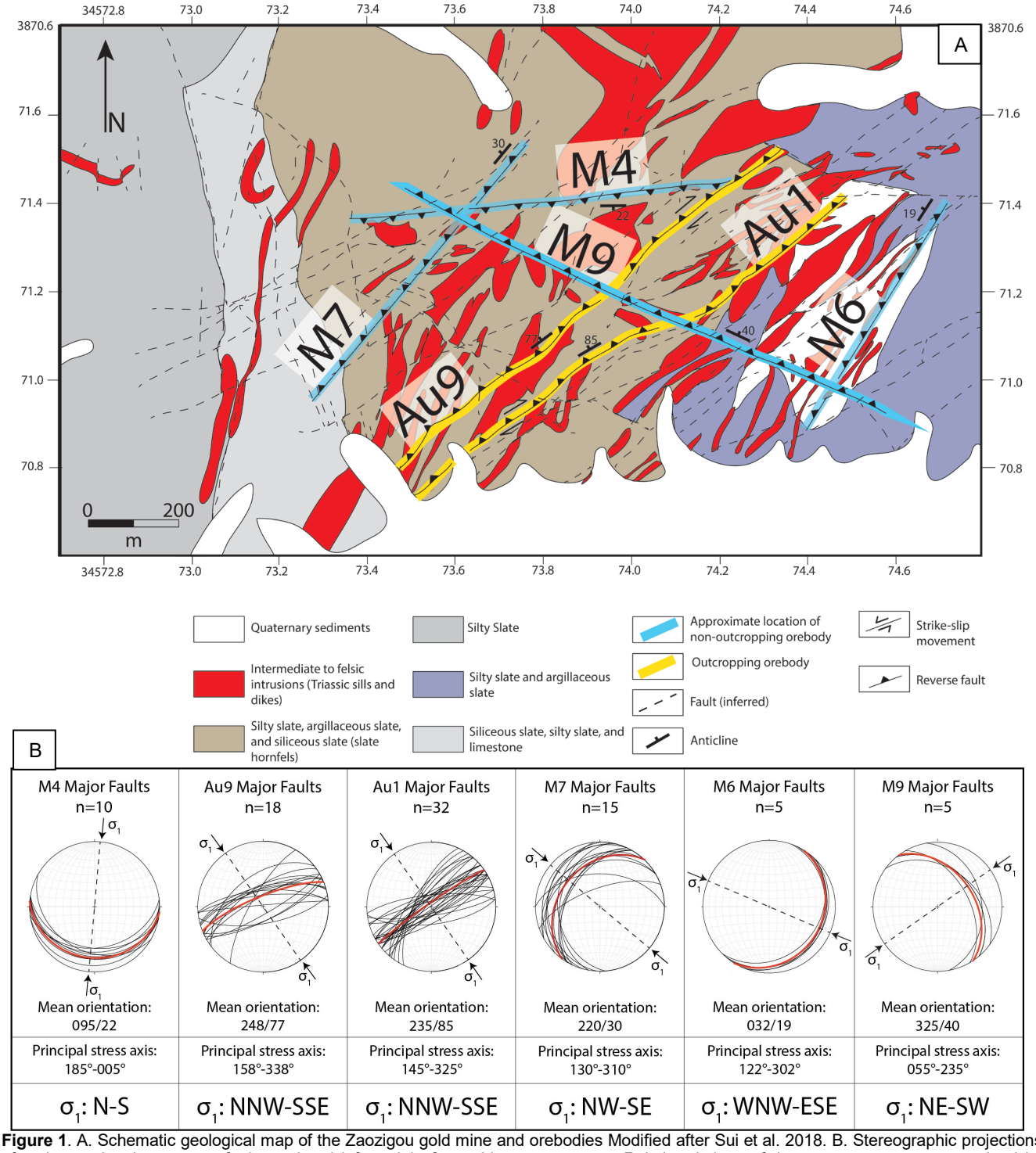

Figure 1. A. Schematic geological map of the Zaozigou gold mine and orebodies Modified after Sui et al. 2018. B. Stereographic projections of major ore-hosting reverse faults, ordered left to right from oldest to youngest. Relative timings of these structures are constrained by observed field crosscutting relationships.

The implications of syn-kinematic precipitation of primary fault-hosted sulfides suggest that mineralization occurred in pulses during the progressive deformation of Zaozigou, as described by Sibson (1988)'s fault valve model for quartz vein formation.

3 Tectonic evolution of Zaozigou in the context of the West Qinling Orogen

The tectonic history of the West Qinling Orogen in the Triassic is not universally accepted. Workers in the region generally favor a tectonic evolution in which the South China Block experienced northward subduction below the North China block (Kröner et al. 1993, Zhang

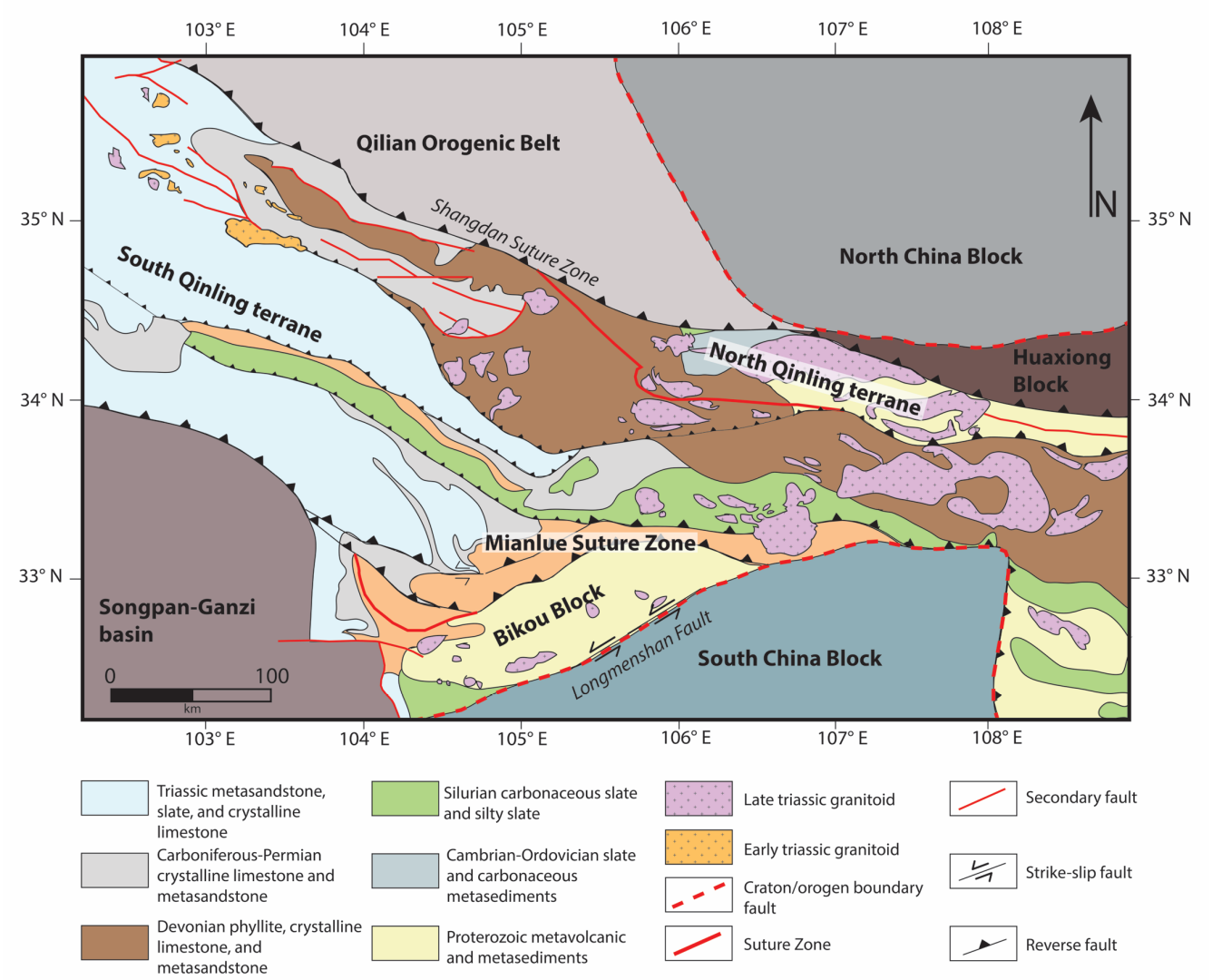

Figure 2. Schematic map of tectonic terranes of the West Qinling Orogen. Modified after Goldfarb et al. (2018).

et al. 2004, Zhang et al. 2001), however Dong et al. (2011) suggest the South China Block was moving towards ~30° northeast, while the North China Block was largely stationary. Both interpretations of the West Qinling tectonics could have produced structure and geometry observed at Zaozigou.

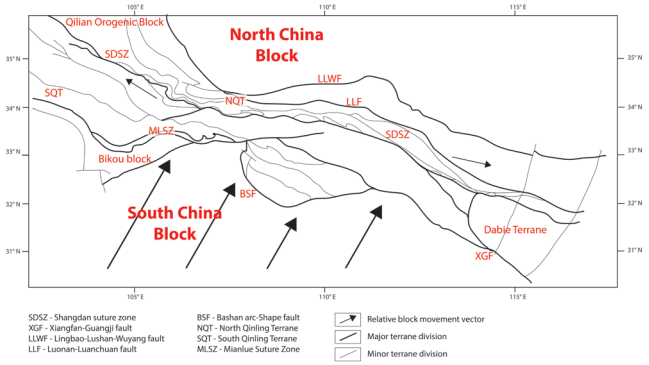

Figure 3. Schematic map of tectonic units involved in the evolution of the West Qinling Orogen.

1). Purely northward movement of the South China Block colliding with the North China Block would have likely produced high angle reverse faults in the North Qinling terrane (Fig. 2). However, this would be at an angle with the Shangdan Suture Zone, likely resulting in dextral oblique reverse motion along the Shangdan Suture Zone, Guanyindazhuang-Lishishan Fault, and Xiahe-Hezuo Fault. Locally at Zaozigou, the dextral movement sense along the Xiahe-Hezuo fault would result in NW-SE primary compression. As collision between the South China Block and North China Block continued, the angle between the Shangdan Suture Zone and South China Block would decrease, resulting in a counter-clockwise rotation of local compressional axis at Zaozigou.

2). Movement of the South China Block toward 30° NE (Fig. 3) would result in a primary stress axis (σ_1) trending 30° NE to 210° SW. Secondary stress axis (σ_2) and minimum stress axis (σ_3) would be oriented perpendicular to σ_1. It is logical to conclude that σ_3 would

have been vertical, therefore σ_2 would be oriented such that the secondary stress axis would trend 120° SE to 300° NW. East-west striking reverse fault, M4 may have been produced by the initial N-S block movement, however as the resultant high-angle reverse faulting became progressively over-steepened, there would be a gradual transition from purely reverse faulting at the block convergence to oblique and eventually strike slip motion along the suture zone. The secondary stress axis related to the northeastern migration of the South China Block in the northwest and southeast West Qinling, would therefore become the local axis of greatest stress in the 120° SE to 300° NW orientation. The resulting strain would be shortening in a SE-NW direction, producing NE-SW striking reverse faults in brittle terranes.

4 Implications for exploration

High angle reverse faults striking NW-SE in proximity to the Xiahe-Hezuo fault should be considered highly prospective for economic gold mineralization. At Zaozigou faulting represents a dilational jog and transpressional environment at a major change in strike of the Xiahe-Hezuo fault. The Xiahe-Hezuo fault is likely a deep, regional scale fault which may be an important fluid conduit for metal-carrying metamorphic fluids. Rotation of the primary stress axis allows for multiple reactivation events along this shear zone in varying orientations. This allows for significant fracturing of rocks along the trend, and therefore increased fluid permeability, brecciation of basement rocks, and increased surface area for hydrothermal fluids to react with.

Acknowledgements

This research was financially supported by the National Natural Science Foundation of China (41702069), and the Fundamental Research Funds for the Central Universities China (292018125, 292018141). We must also thank Zhaojin gold company and the Zaozigou mine staff for their hospitality and logistical support.

References

Dong Y, Zhang GW, Neubauer F, Liu XM, Genser J, and Hauzenberger C (2011) Tectonic evolution of the Qinling orogen, China: Review and synthesis. Journal of Asian Earth Sciences, 41:213-237.

Kroner A, Zhang GW, Sun Y (1993) Granulites in the Tongbai area, Qinling belt, China: geochemistry, petrology, single zircon geochronology, and implications for the tectonic evolution of eastern Asia. Tectonics, 12(1):245-255.

Goldfarb RJ, Qiu KF, Deng J, Chen YJ, and Yang LQ (2019) Orogenic Gold Deposits of China. Economic Geology. SEG Special Publications, 22, 1-000. UNPUBLISHED

Sibson R (1988) High-angle reverse faults, fluid-pressure cycling, and mesothermal gold-quartz deposits. Geology, 16(6):551-555.

Sui JX, Li JW, Jin XY, Vasconcelos P, and Rui Z (2018) $^{40}Ar/^{39}Ar$ and U-Pb constraints on the age of the Zaozigou gold deposit, Xiahe-Hezuo district, West Qinling orogen, China: Relation to early Triassic reduced intrusions emplaced during slab rollback. Ore Geology Reviews, 101:885-899.

Qiu KF, Deng J (2017) Petrogenesis of granitoids in the Dewulu skarn copper deposit: implications for the evolution of the Paleotethys ocean and mineralization in western Qinling, China. Ore Geology Reviews, 90:1078-1098.

Yu HC, Guo CA, Qiu KF, McIntire D, Jiang GP, Gou ZY, Geng JZ, Pang Y, Rui Z, Li NB (2019) Geochronological and geochemical constraints on the formation of the giant Zaozigou Au-Sb deposit, West Qinling, China. Minerals, 9:37.

Zhang GW, Zhang BR, Yuan XC, Xiao QH (2001) Qinling orogenic belt and continental dynamics. Science Press, Beijing.

Zhang T (2015) The Geochemistry characteristics and metallogenic series of Gangcha pluton in Tongren, Qinghai Province. PhD Thesis, China University of Geoschiences, Beijing.

Metabasalts as sources of gold in Archean greenstone belts

Iain Pitcairn, Alexandre Peillod
Department of Geological Sciences, Stockholm University, Sweden

Clifford Patten
Institute for Applied Geosciences Geochemistry and Ore Geology Group,, Germany

Jean Goutier
Ministère de l'Énergie et des Resources naturelles, Canada

Carl Guilmette, Georges Beaudoin
E4m, Département de géologie et de génie géologique, Université Laval, Québec, Canada

Abstract. Abundant volcanic rocks in Archean greenstone belts have been suggested as potential sources of metals in Archean orogenic gold deposits. However, the behaviour of gold during the metamorphism of these rocks is poorly known. We present ultra-low detection limit gold analyses from a suite of variably metamorphosed samples from the La Grande subprovince, Québec, Canada. The median mass change value in the amphibolite and upper amphibolite facies sample sets compared to the greenschist facies samples is -56% and -79% respectively and 1 km^3 of greenschist facies metavolcanic rock metamorphosed to amphibolite facies would produce around 2 tonnes of Au. These rock types are therefore potentially important metal sources for Archean orogenic gold deposits.

1 Introduction

Th sources of metals in Archean orogenic gold deposits have long been debated. Suggested metal sources are wide ranging and include metamorphic devolatilisation of metasedimentary and metavolcanic rocks (Groves et al. 1998; Beaudoin and Pitre 2005; Gaboury et al. 2013), magmatic hydrothermal fluids (Burrows and Spooner 1985), meteoric fluids (Nesbitt 1991), the lower crust and sub-continental lithospheric mantle (Hronsky et al. 2012). In Phanerozoic orogenic gold systems, metasedimentary rocks are thought to be the main metal source with metal-bearing fluids being produced from these rocks during prograde metamorphic devolatilisation (Pitcairn et al. 2006a; 2015; Tomkins 2010). Archean deposits are hosted in granite-greenstone belts that are comparatively poor in metasedimentary rocks. These belts contain far greater abundances of volcanic than sedimentary rocks but it is unclear whether volcanic rocks have compositions appropriate for producing Au-rich metamorphic fluids during orogenesis. Tomkins (2010) showed that metamorphism of mafic rocks produces considerably less H_2S, the ligand which is required to transport Au during metamorphic devolatilization, and over a much smaller temperature window than sedimentary shales. Furthermore, mafic volcanic rocks are relatively poor in other elements such as As which are ubiquitously enriched in orogenic gold deposits (Tomkins 2010; Pitcairn et al. 2014; Patten et al. 2016).

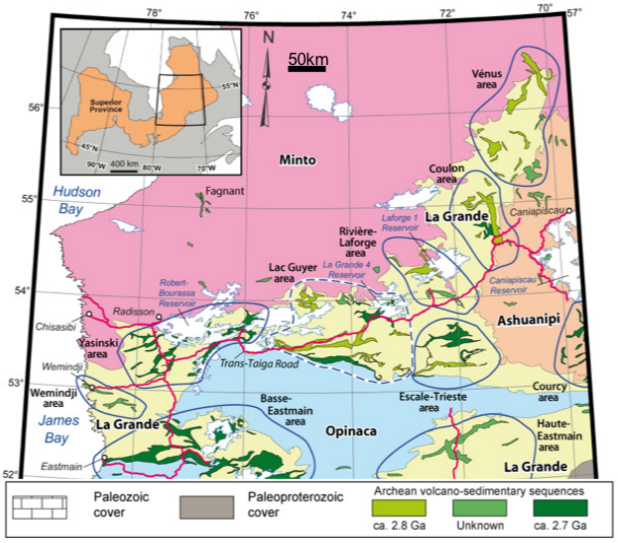

Figure 1. Geological map showing the location of the La Grande subprovince in northern Québec, Canada. Samples were collected from the metavolcanic units in the Yasinski, Lac Guyer, and Rivière-La Forge areas. Modified from Sappin et al. (2018).

We report a set of major and trace element analyses including ultra-low detection limit Au analyses from a suite of metavolcanic rocks from the La Grande subprovince, Québec, Canada (Fig. 1). The metavolcanics rocks in this area show a strong metamorphic gradient from lower greenschist facies in the west of the terrane towards upper amphibolite facies in the east (Goutier et al. 2003; Gauthier et al. 2007). The results show the capability of metavolcanics rock to produce Au-bearing fluids during metamorphism and therefore the potential for these lithologies to be the sources of metals in Archean greenstone-hosted orogenic gold deposits.

2 Geological setting

The La Grande subprovince is located in the east-central

Superior Province, Canada (Fig. 1) and is composed of multiply deformed sequences of Archean volcano-sedimentary and plutonic rocks (Houlé et al. 2015). The La Grande subprovince comprises submarine volcanic sequences including 2820-2806 Ma Guyer Group (Goutier et al. 2002; David et al. 2012), the 2751-2732 Ma Yasinski Group (Goutier et al. 2001), and sedimentary sequences overlying tonalitic gneiss basement (3452−2788 Ma; Davis et al. 2014), all of which is intruded by intermediate to felsic plutonic rocks (~2716−2709 Ma; Mercier-Langevin et al. 2012). The rocks in the La Grande area were subject to four major Archean-aged compressional deformation events (Goutier et al. 2001, 2003), and 3 associated metamorphic episodes (Goutier et al. 2003). A steeply dipping ENE trending D_2 foliation is dominant in the area. The subprovince hosts the world-class Roberto gold deposit (~8.8 Moz Au; Fontaine et al. 2015) and several other gold and base metal mineral deposits.

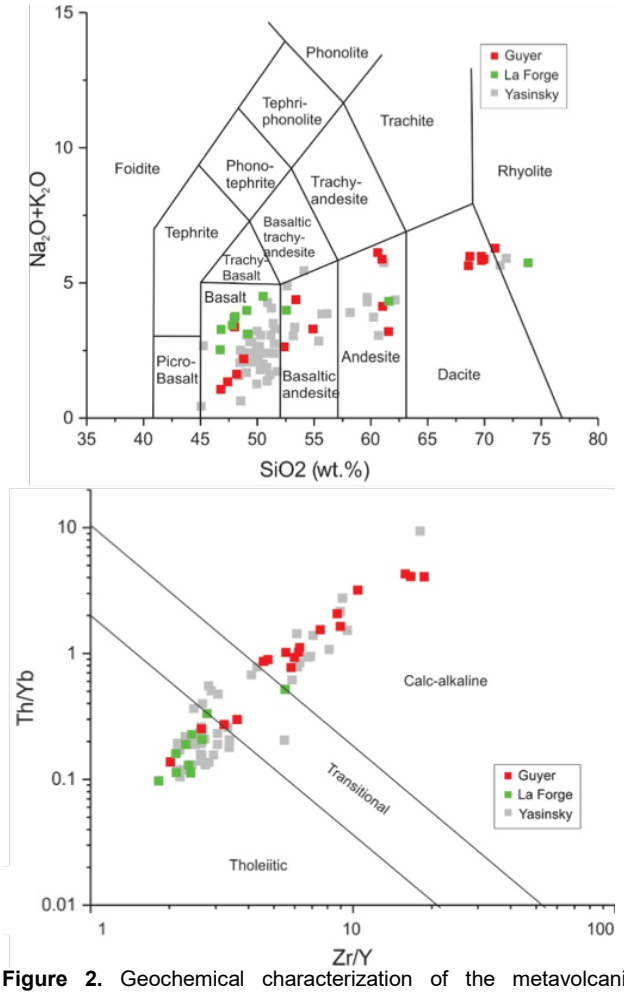

Figure 2. Geochemical characterization of the metavolcanic samples from the Yasinski, Guyer and La Forge groups from the La Grande subprovince, Québec, Canada. 2A: $Na_2O+K_2=$ vs SiO_2 diagram, 2B: Th/Yb vs Zr/Y diagram.

3 Sampling and analytical methods

A suite of 90 samples was collected dominantly from the Yasinski, Guyer and La Forge groups. Weathered and mineralised samples were avoided. Precise metamorphic temperatures are not well constrained and so samples are grouped according to the metamorphic facies based on the bulk silicate mineralogy. The Yasinski Group samples comprise 4 subgreenschist, 32 greenschist and 16 amphibolite facies samples, the 18 Guyer Group samples are all amphibolite samples and the 10 La Forge Group samples are all upper amphibolite facies. Major and trace elements were analyzed by ALS Global and Au was analysed at Stockholm University following the ultra-low detection limit method of Pitcairn et al. (2006b) that has a 3σ detection limit of 0.02 ppb.

4 Geochemical classification of samples

The Yasinski Group samples comprise basalts (n=37; 45.1-53.2 wt.% SiO_2), basaltic andesites (n=7; 48.6-56.1 wt.% SiO_2), andesites (n=7, 58.2-62.1 wt.% SiO_2), and dacite/rhyolites (n=2, 71.4-71.9 wt.% SiO_2). The basalts show a tholeiitic to transitional affinity (Zr/Y<6.1 and Th/Yb<1.4, Fig. 2), the basaltic andesites and andesites a transitional to calc-alkaline affinity (Zr/Y>4.11 and Th/Yb>0.2), and the dacite/rhyolites a calc-alkaline affinity (Zr/Y>9 and Th/Yb>2.2; Fig. 2a). The Guyer Group samples contain basalts (n=5, 46.8-48.8 wt.% SiO_2), basaltic andesites (n=3; 48-54.9 wt.% SiO_2), andesites (n=4, 60.6-61.6 wt.% SiO_2), and dacite/rhyolites (n=6, 68.6-70.9 wt.% SiO_2). The basalts have a tholeiitic affinity (Zr/Y<3.6 and Th/Yb<0.8) and the basaltic andesites, andesites and dacite/rhyolite all have a calc-alkaline affinity (Zr/Y>4.7 and Th/Yb>0.9, Fig. 2). The La Forge Group is dominated by basalts (n=8; 46.7-50.5 wt.% SiO_2) with one basaltic andesite (52.6 wt.% SiO_2) and one andesite (61.6 wt.% SiO_2) sample, and all except one are of tholeiitic affinity (Zr/Y<2.8 and Th/Yb<0.3; Fig. 2).

The volcanic rocks of the La Grande subprovince are suggested to have formed by interaction between a differentiated crust and Mg-rich magmas rising from a depleted mantle source (Seymour and Francis 1987; Skulski et al. 1988; Richer-LaFlèche et al. 2000; David et al. 2011; Sappin et al. 2018). The tholeiitic MORB-like basaltic samples are interpreted to be the erupted volcanic products of Mg-rich magmas emplaced at subcrustal levels with limited interaction with the differentiated crust (Sappin et al. 2018). The transitional to calc-alkaline magmatic series are interpreted to have formed from interaction between the Mg-rich magmas and the differentiated crust leading either to crustal contamination and assimilation fractionation processes or mixing between mantle-derived and lower crust anatectic melts (Skulski et al. 1988, Richer-LaFlèche et al. 2000; Sappin et al. 2018). There is no sharp transition between the tholeiites and the crustal contaminated calc-alkaline magmatic series but rather a continuum with increasing crustal components.

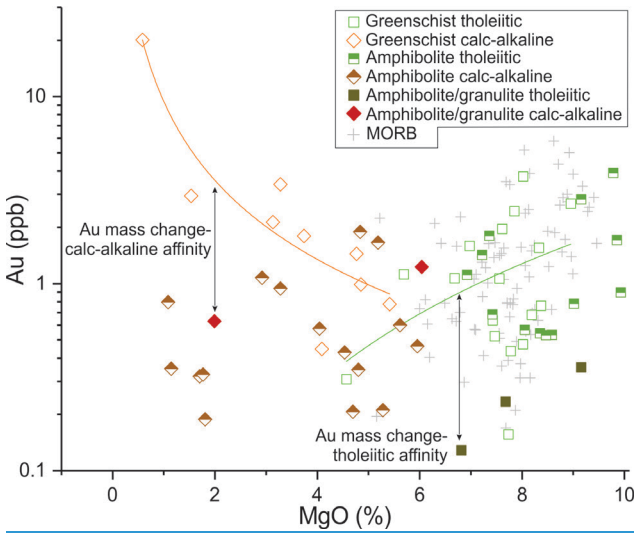

Figure 3. Magmatic differentiation trends for the calc-alkaline and tholeiitic series determined from the Yasinski sub-greenschist and greenschist samples and method for calculating Au mass change for higher metamorphic grade samples.

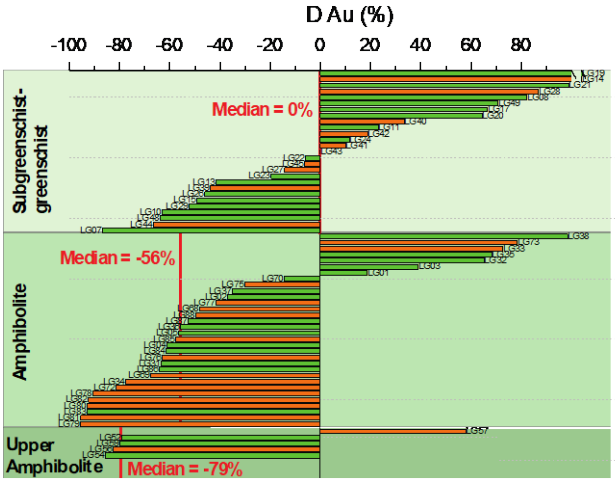

Figure 4. Mass change values for Au calculated for individual samples (named LG10, LG11 etc) relative to the respective calc-alkaline (orange) and tholeiitic (green) magmatic differentiation trends. Median mass change values for the amphibolite and upper amphibolite samples are -56% and -79% respectively.

5 Discussion

5.1 Protolith composition and mass change during metamorphism

The metavolcanic rocks from the La Grande subprovince have undergone different magmatic processes and their primary Au content and therefore their potential for producing Au-bearing metamorphic fluids may vary significantly. The sub-greenschist and greenschist facies Yasinski Group samples are used to calculate the protolith metal contents for both the tholeiitic and calc-alkaline affinities. The tholeiitic basalts have median Au concentrations of 1.06 ppb, (range = 0.16-3.75 ppb) similar to modern day fresh MORB (median = 1.17 ppb, range 0.17-5.77 ppb). The decreasing Au content with decreasing MgO implies that Au behaves as a compatible element during the magmatic differentiation and suggests that the melt is sulphide saturated. The calc-alkaline series have higher Au content (median = 1.62 ppb, 0.45-20.1 ppb) and different distribution than the greenschist tholeiitic basalts and fresh MORB (Fig. 3). Gold concentration in the calc-alkaline magmatic series increases with decreasing MgO implying an incompatible behavior during magma-crust interaction by assimilation fractional crystallisation.

Magmatic differentiation curves for Au are calculated both for the tholeiitic and the calc-alkaline series from the greenschist samples of the Yasinski group. These magmatic trends are used to calculate mass variation associated with metamorphism for the Yasinski, Guyer and La Forge Group samples. The mass change in Au relative to these magmatic differentiation curves is calculated for each sample using the method described in Jowitt et al. (2012) using the following relationship:

$$\Delta Au = Au_c - Au_s$$

where ΔAu is the Au mass change, Au_c the calculated protolith Au composition based on the MgO composition and position on the magmatic differentiation curve and Au_s the measured Au value (Fig. 4). The median mass change value in the amphibolite and upper amphibolite facies sample sets compared to the greenschist facies samples is -56% and -79% respectively (Fig. 4). Both tholeiitic and calc-alkaline series rocks show significant depletions in Au in the amphibolite and upper amphibolite facies samples. Assuming an average composition of 1.3 ppb Au (based on a composition of 50% tholeiitic and 50% calc-alkaline affinity), an average density of 2.8 g/cm^3, and an Au mass loss of -56%, 1 km^3 of greenschist facies metavolcanic rock metamorphosed to amphibolite facies would produce around 2 tonnes of Au. Of the other elements commonly enriched in orogenic gold deposits such as S, As, Sb, Bi, Te, none of them show any significant mobility during metamorphism with the exception of As which shows slight decreases in concentration with increasing metamorphism. However, the As concentrations in the greenschist facies metavolcanic rocks of 0.45 ppm are more than an order of magnitude lower than concentrations in metasedimentary rocks of the same metamorphic grade (e.g. Pitcairn et al. 2017).

5.2 Implications for sources of metals in Archean greenstone-hosted orogenic gold deposits

Their abundance in greenstone belts combined with the observed mobility of Au in these rocks during metamorphism indicate that metavolcanic rocks can be important potential sources of Au in Archean greenstone belt hosted orogenic gold deposits. In large Archean greenstone belts such as the Abitibi belt in Canada that comprise around 40% metavolcanic rocks on surface, more than 100000 km^3 of higher metamorphic grade metavolcanic rocks are interpreted to occur at depth (e.g. Kerrich and Ludden 2000). The fertility of the metavolcanic rock with respect to Au may vary

considerably. Our results show different fertilities for Au between the calc-alkaline and tholeiitic series in the La Grande subprovince. The behaviour of S during magmatic differentiation also strongly controls the availability of chalcophile elements for later metamorphic remobilization with sulfur undersaturated volcanic rocks commonly showing higher Au concentrations (Patten et al. 2016. Plume-related volcanic rocks are also known to have higher concentrations of gold (Webber et al. 2013; Pitcairn et al. 2014). The mass change for Au in other more fertile terranes may be considerably greater than reported here for the La Grande.

The lack of mobility of other elements enriched in orogenic gold deposits such as As and Sb indicates that metavolcanic rocks are unlikely to be the only source rock. Metasedimentary rocks are likely to be important sources of Au and the main source of As, Sb and S (Pitcairn et al. 2017). Magmatic hydrothermal fluids may be important local sources of metals in deposits enriched in Mo, Bi and Te (Pitcairn et al. 2017). Deposits formed from predominantly metavolcanic source rock should therefore show distinct compositions such as having much higher Au:As than deposits formed from metasedimentary source rocks. Interestingly, orogenic gold deposits in Archean greenstone belts that are As and Sb rich tend to be sediment hosted (e.g. the Roberto deposit) whereas those that are hosted in volcanic rocks are commonly relatively As and Sb poor.

Acknowledgements

We acknowledge funding from Natural Resources Canada and Fonds de Recherche du Québec Nature et Technologies (FRQ-NT).

References

Beaudoin G, Pitre D, 2005. Stable isotope geochemistry of the Archean Val-d'Or (Canada) orogenic gold vein field: Min Dep 40:59-75

David, J, et al., 2012. Datations U-Pb effectuées dans les provinces du Supérieur et de Churchill en 2010-2011. Ministère de l'Énergie et des Ressources naturelles, Report RP-2012-01, 33 p.

Davis, DW et al., 2014. Datations U-Pb effectuées dans les provinces du Supérieur et de Churchill en 2011-2012 – Ministère de l'Énergie et des Ressources naturelles Report RP 2014-05, 61 p.

Fontaine, A, Dubé, B, Malo, M, McNicoll, VJ, Brisson, T, Doucet, D, Goutier, J, 2015. Geology of the metamorphosed Roberto gold deposit (Éléonore Mine), James Bay region, Quebec: diversity of mineralization styles in a polyphase tectonometamorphic setting, Geological Survey of Canada, Open File 7852:209–225

Gaboury, D, 2013. Does gold in orogenic deposits come from pyrite in deeply buried carbon-rich sediments? Insights from volatiles in fluid inclusions. Geology 41, 1207-1210

Gauthier, M, Trepanier, S, Gardoll, S, 2007. Metamorphic gradient: A regional-scale area selection criterion for gold in the northeastern Superior province, eastern Canadian Shield: SEG Newsletter 69:10−15

Goutier, J, et al., 2000. Geologie de la region des lacs Guillaumat et Sakami (SNRC 33F/02 et 33F/07): Ministère des Ressources naturelles, Québec, Report RG 99-15:37.

Goutier, J, et al., 2001. Geologie de la colline Masson (SNRC 33F/09, 33F/10. 33F/15 et 33F/16): Ministère des Ressources naturelles, Québec, Report RG 2000-10:67.

Goutier, J, et al. 2003. Synthese geologique de la region des lacs Sakami (33F) et Guyer (33G), Baie-James: Ministère des Ressources naturelles, Québec, Report DV 2002-12:11−13.

Goldfarb RJ, Groves DI, 2015. Orogenic gold: Common or evolving fluid and metal sources through time. Lithos 233:2–26

Groves DI, Goldfarb RJ, Gebre-Mariam M, Hagemann SG, Robert F, 1998. Orogenic gold deposits—a proposed classification in the context of their crustal distribution and relationship to other gold deposit type: Ore Geol Rev 13:7–27

Houlé, M.G., Goutier, J., Sappin, A.-A., McNicoll, V.J., 2015. Regional characterization of ultramafic to mafic intrusions in the La Grande Rivière and Eastmain domains, Superior Province, Québec. Geological Survey of Canada, Open File 7856:125–137.

Hronsky, JM, Groves, DI, Loucks, RR, Begg, GC, 2012. A unified model for gold mineralisation in accretionary orogens and implications for regional-scale exploration targeting methods: Min Dep 47:339–358

Jenner FE, O'Neill HSC, 2012. Major and trace analysis of basaltic glasses by laser-ablation ICP-MS. Geochemistry, Geophys Geosystems 13

Jowitt SM, Jenkin GR, Coogan LA, Naden J, 2012. Quantifying the release of base metals from source rocks for volcanogenic massive sulfide deposits: effects of protolith composition and alteration mineralogy. J. Geochem. Explor. 118:47–59

Kerrich, R, Ludden J, 2000. The role of fluids during formation and evolution of the southern Superior Province lithosphere: an overview: Can J Earth Sci 37:135–164

Patten CGC, Pitcairn IK, Teagle DAH, Harris M, 2016. Mobility of Au and related elements during the hydrothermal alteration of the oceanic crust: implications for the sources of metals in VMS deposits. Min Dep 51:179–200

Pitcairn IK, Teagle DAH, Craw D, et al 2006a. Sources of metals and fluids in orogenic gold deposits: insoghts from the Otago and Alpone schists, New Zealand. Econ Geol 101, 1525–1546

Pitcairn IK, Warwick PE, Milton JA, Teagle DAH 2006b. Method for ultra-low-level analysis of gold in rocks. Anal Chem 78:1290–1295

Pitcairn IK, Craw D, Teagle DAH 2014. Metabasalts as sources of metals in orogenic gold deposits. Miner Depos 50:373–390

Pitcairn, IK, Skelton, ADL, Wohlgemouth-Ueberwasser, CC, 2015. Mobility of gold during metamorphism of the Dalradian in Scotland: Lithos 233:69-88

Pitcairn, IK, Leventis, N, Beaudoin, G, Faure S, Dubé, B, 2017. A metasedimentary source of Au for the Abitibi? 15th Biennal SGA Conference, 20-23rd August 2017, Quebec, Canada

Richer-Laflèche, M, Moorhead, J, Goutier, J, Fallara, F, 2000. Géochimie des roches volcaniques et des formations de fer du Groupe de Yasinski, sous-province de La Grande. MERN Report 2000-13:59.

Sappin, A-A, Guilmette, C, Goutier, J, Beaudoin, G, 2018. Geochemistry of MesoArchean felsic to ultramafic volcanic rocks of the Lac Guyer Area, La Grande Subprovince, Canada: Evidence for plume related magmatism in a rift setting. Precamb. Res. 316:83-102

Skulski, T, Hynes, A, Francis, D, 1988. Basic lavas of the Archean La Grande greenstone belt: products of polybaric fractionation and crustal contamination. Contributions to Min and Pet 100:236–245

Tomkins, AG, 2010. Windows of metamorphic sulfur liberation in the crust: Implications for gold deposit genesis: Geochim et Cosmochim Acta 74:3246–3259

Webber AP, Roberts S, Taylor RN, Pitcairn IK, 2013. Golden plumes: Substantial gold enrichment of oceanic crust during ridge-plume interaction. Geology 41:87–90

Geochemical paragenesis of pyrite associated with orogenic gold at Curraghinalt, Northern Ireland

James P. Stratford and Sean H. McClenaghan
Department of Geology, Trinity College Dublin, Ireland;
Irish Centre for Research in Applied Geosciences, Dublin, Ireland

Abstract. The Neoproterozoic-Cambrian Dalradian Supergroup in Northern Ireland is host to significant Au mineralization: the largest deposit discovered to date is Curraghinalt (>6 Moz*, SRK Consulting (Canada) Inc., 2018), 17km NE of Omagh, characterized by WNW-ESE trending pyritiferous quartz-carbonate veins dipping c. 55-70° to the north. Petrographic examination of vein pyrite and analysis by Laser Ablation Inductively Coupled Plasma – Mass Spectroscopy (LA-ICP-MS) reveals four distinct generations of pyrite (Py_{1-4}) that record a history of emplacement and modification during the Grampian orogeny (475-460 Ma). Py_1 within early veins is broadly aligned with regional S_2/S_3 Grampian fabrics and records an early Zn-Ni signature (Median Zn 5,030 ppm; Ni 2,410 ppm). Py_2 overgrowths have an entrained schistosity indicating growth during prograde development of S_2/S_3 fabrics; Au is elevated in Py_2 with a median of 3.69 ppm (IQR 2.02-10.1 ppm) and is coincident with elevated Co and Ni. Py_3, occurring within the vein swarm cutting the host penetrative fabric, exhibits elevated Ni (median 134 ppm, IQR 20.4-395 ppm). Electrum is encountered along fractures of Py_3 that have been healed by auriferous pyrite (Py_4) that exhibits a Bi-Te signature. Geochemically constrained pyrite can be a useful tool for targeting of Au mineralization across orogenic belts.

1 Geological context

Vein-hosted auriferous deposits occur in Ireland and in central Scotland, constrained within rocks of the Dalradian Supergroup

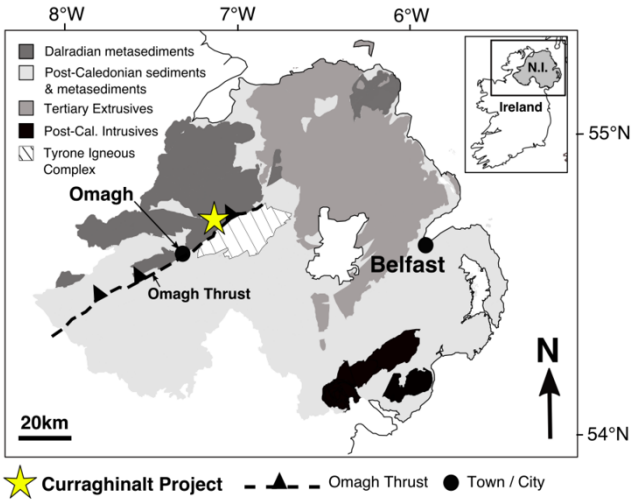

Figure 1. Location of Curraghinalt gold deposit, with generalized regional geology of Northern Ireland (inset map: location of N.I.)

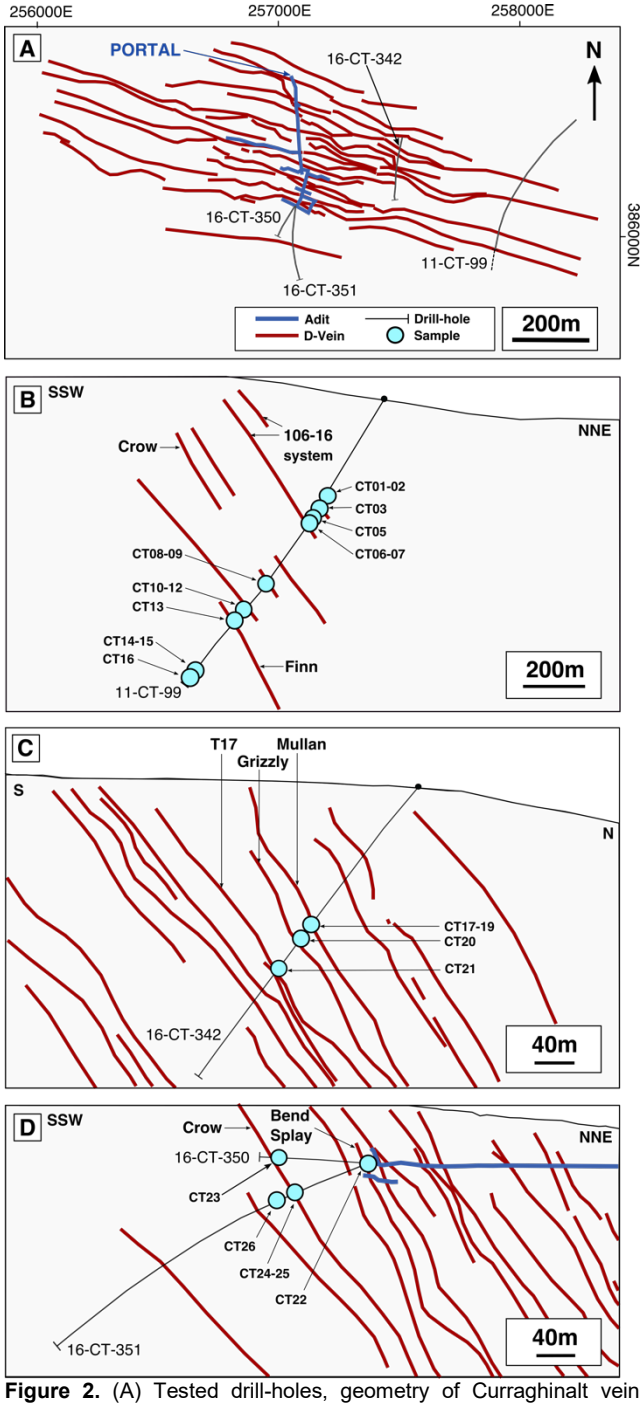

Figure 2. (A) Tested drill-holes, geometry of Curraghinalt vein swarm (resource-associated 'D' vein zones). (B-D) Cross-sections of drill-holes and locations of samples in the context of the main swarm. Co-ordinates use the Irish National Grid.

which occur within the SW-NE trending Grampian

tectono-stratigraphic terrane. This late Neoproterozoic to Cambrian succession is composed of siliciclastics, limestones and mafic volcanics which were deposited on the Laurentian margin between the late Neoproterozoic and Cambrian (c. 800-510 Ma; Daly et al, 2009).

During the Grampian Orogeny, an arc-continent collisional phase of the Caledonian Orogenic Cycle (475-405 Ma) which ultimately led to the closure of the Iapetus Ocean, the Dalradian Supergroup underwent polyphase deformation, reaching upper-greenschist to amphibolite facies metamorphic conditions (Fettes, 1979). Peak pressures and temperatures at upper greenschist facies were recorded in the Sperrins region of Northern Ireland at approximately 468 Ma (Chew and Stillman, 2009). The southern extent of the terrane is demarcated by a major SW-NE trending structure known in Ireland as the Fair Head – Clew Bay Line (FH-CBL), which is contiguous with the Scottish Highland Boundary Fault (HBF).

Occurrences along strike to the SW and NE of Curraghinalt are being actively explored, while active mining is taking place at Cavanacaw, approximately 30km to the south-west. Stratigraphically contiguous gold occurrences in Ireland are also recognized along the belt in the Ox Mountains of Co. Sligo.

Gold distribution in the Sperrin mountains region is considered to be influenced by the presence of three principle regional structures: the SSW-NNE trending Omagh Lineament, the SW-NE trending Omagh Thrust and the Sperrin fold (ESE-WNW to SE-NW axial trace), an F_2 recumbent antiform (Earls et al, 1996); at Curraghinalt, E-W trending dextral strike-slip structures control the distribution of auriferous quartz veins.

2 Petrography

2.1 Pyrite

The sulfide mineralogy across the Curraghinalt deposit is dominated by pyrite, accompanied by chalcopyrite and galena. Of these, pyrite is the most abundant sulfide mineral and is observed within all vein types and in altered wallrock. A variety of pyrite morphologies ranging from 10 microns to over 1mm in size have been recognised, these include euhedral grains, overgrowths and healed fractures. Specific generations of pyrite have been recognised using petrographic and microanalytical criteria, herein designated as Py_1-Py_4; Py_{3-4} are ore-stages associated with discrete phases of visible gold in the form of electrum.

Py_1 with distinct overgrowths (Py_2) (see Fig. 3A) are identified within angular, subhedral grains located within veinlets dominated by carbonate, sulfide and minor quartz. Growth of Py_2 with entrained minerals developing along the S_2/S_3 fabric suggests that these veins are the earliest recognised at Curraghinalt. Py_1-Py_2 grains are sub-millimetric in scale and bear late cross-cutting fractures. Py_1 is largely homogenous in appearance while close inspection reveals micro-inclusions of galena and sphalerite occurring as clusters or aligned trails, suggestive of metasomatic alteration and distortion of the host crystal lattice. Within Py_2, inclusions of ankerite and silicates exhibiting alignment to the crystal boundary and enveloping schistosity are observed. Visible gold is encountered in microfractures associated with major fractures cross-cutting both Py_1 and Py_2.

Py_3 occurs within 'D' quartz veins (see Fig. 3B) cutting the penetrative S_2/S_3 fabric of the host rock and is associated with post-peak metamorphic conditions. Grains are euhedral to anhedral, may have angular or rounded edges and are coarse grained (<1 mm in size). In many observed veins, Py_3 occurs as large (millimetric), cataclastic masses characteristic of abrupt brittle deformation. This phase carries irregular electrum inclusions within the grains themselves, observed at <30 µm in diameter, or as elongate blebs along boundaries and within micro-fractures. Microfractures appear to have been healed by pyrite (Py_4), though this is petrographically indistinguishable from Py_3.

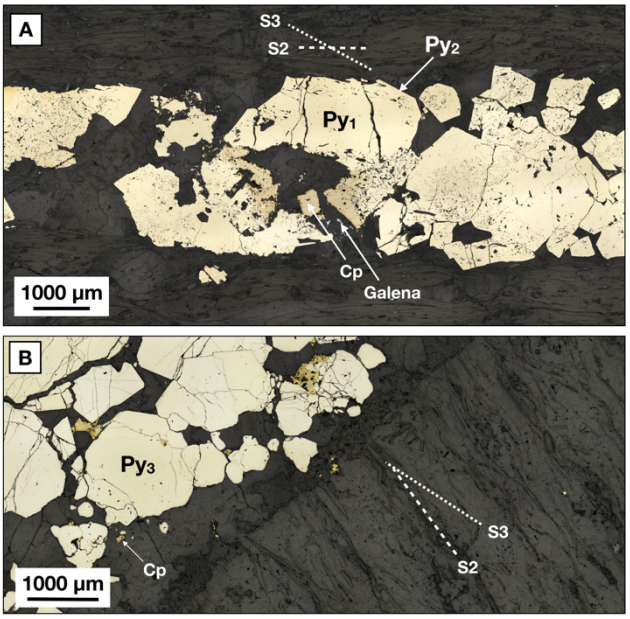

Figure 3. (A) Reflected light image of Py_1 and Py_2 overgrowth phase in S_2/S_3 fabric-parallel vein comprised of ankerite and quartz (sample CT12, drill-hole 11-CT-99, 819.04-819.24m); (B) oblique spatial relationship of quartzose vein hosting ore-phase Py_3 with the S_2/S_3 fabric of the host rock in sample CT20 (drill-hole 16-CT-342, 'Grizzly' vein zone, 199.83-199.93m).

Disseminated pyrite porphyroblasts (<50 µm) are also observed in the wallrock, in close alignment with fabrics, occurring proximal to auriferous veins hosting Py_3. Fabric relationships and trace element geochemistry suggest that this phase is Py_2.

2.2 Visible gold

Energy dispersive spectroscopic analyses (EDS/EDX) (n=23) of electrum associated with ore-stage Py_3 in samples from the central and lower veins reveal mean concentrations of 86.05 wt.% Au and 11.12 wt.% Ag. Where inclusions are observed which may be associated with late healing phase Py_4 (within micro-fractures), concentrations of gold are close to the overall mean for the sample set, at 86.14 wt.% Au, with 10.88 wt.% Ag.

Inclusions of electrum tend to be more argentiferous in central vein sampling (with average concentrations of 76.18 wt.% Au, 19.45 wt% Ag), than those observed in the lower swarm (averaging 87.20 wt% Au, 11.89 wt.% Ag).

Electrum was also encountered along the boundaries of Py3 grains within more brecciated vein samples in the lower swarm, where inclusions are less common. Concentrations for this type averages 87.9 wt.%, with a narrow range of between 87.9 to 88.1 wt.%.

Zoned inclusions (see Fig. 4) are observed within the central veins containing a Bi-telluride and electrum component, while a Ag-Te rim is also visible for some Bi-tellurides (averaging 60.24 wt.% Ag). This inclusion type is most common in samples from the central part of the deposit. In lower swarm samples, such inclusions are less common, and electrum tends to be most pervasive at junctions of fractures and along grain edges. Observations suggest a coeval relationship between Au, Ag, Bi and Te, particularly within central veins where tellurides are more common.

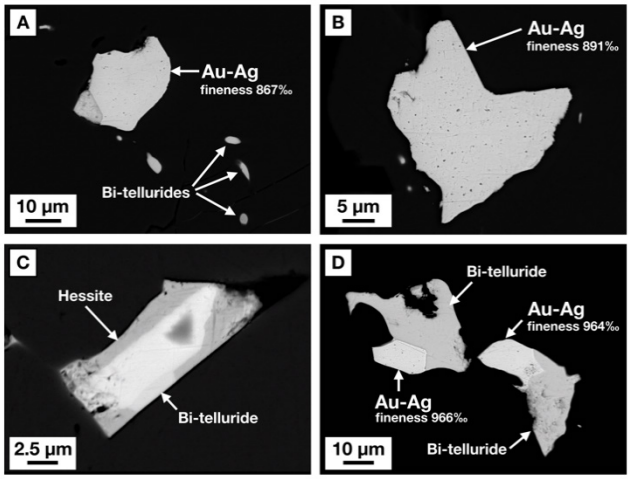

Figure 4. SEM images of ore-stage electrum (Au-Ag) and Bi-tellurides (sample CT20, drill-hole 16-CT-342, 'Grizzly' vein zone, 199.83-199.93m). Analyses were conducted in backscattered mode at a working distance of 18.5mm using a voltage of 20kV.

3 Geochemical paragenesis

3.1 Early Py_1 development

A diagnostic feature of Py_1 is the presence of micro-inclusions of sphalerite and galena; in-situ Laser Ablation ICP-MS analyses (n=30) show elevated Zn (median = 5,030 ppm, IQR = 4,000-7,400) and Ni (median 2,410 ppm, IQR = 1,850-3,420) (see Fig. 5). A positive correlation (n=16) is observed for Zn in Py_1 with Bi (0.88), Mo (0.82), Ga (0.71) and Ag (0.65). The homogeneity of Zn within Py_1 was confirmed using Laser Ablation ICP-MS elemental mapping (>1,000 ppm Zn) (see Fig. 6). This tested sample (CT12, see Fig. 2D) was retrieved from drill-hole 11-CT-99 at a down-hole depth of >800m, which may suggest a Zn-Ni bearing system at deeper crustal levels. Py_1 also has a Co/Ni ratio of 0.04, an order of magnitude lower than Py_2 (0.55) which suggests a distinct origin for the early Py_1 phase.

3.2 Py_2 development

A bimodal distribution of Au is recognized within in-situ data collected, with a median value across the Py_{1-3} dataset (n=149) of 0.23 ppm Au (IQR 0.09-0.98). The highest median value of Au is observed within Py_2 (3.69 ppm Au, IQR 2-10.1 ppm, n=34), with a maximum recorded value of 39.1 ppm Au. Conversely, ore-stage Py_3 exhibits relatively low Au contents.

The presence of Au within Py_2 confirms that an auriferous fluid was active within the system prior to mineralization within ore-stage Py_3, constrained by previous workers to a maximum 10 Myr interval (462.7 - 452.8 Ma; Rice et al., 2016). This interval post-dates peak metamorphism contemporary with the final stages of Grampian arc-continent collision at 468 Ma.

LA ICP-MS depth profiles for spot analyses show homogenous levels of trace elements, lacking distinct spikes in Au supporting the presence of lattice bound Au in Py_2.

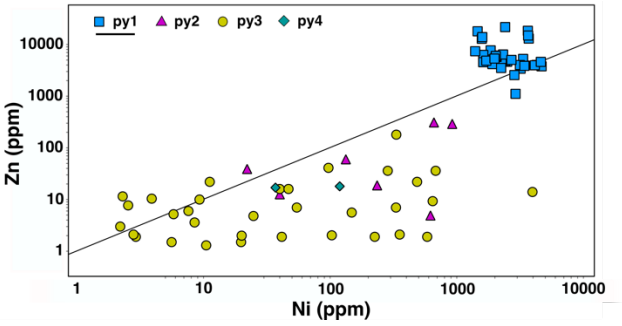

Figure 5. Zn vs. Ni concentrations reported for in-situ LA ICP-MS analyses (n=77). Values for Py_1 (n=35) show relative enrichment (sample CT12, drill-hole 11-CT-99, 819.04-819.24m).

3.3 Ore-stage: growth of Py_3-Py_4

LA-ICP-MS element mapping of Py_3 grains (see Fig. 7) reveals enrichment of Ni (median = 134 ppm, n=137) and oscillatory element variations for both Ni and Co; in-situ analyses record interquartile ranges of 20.4-395 ppm for Ni and 10.2-260 ppm for Co. This record of compositional zonation suggests varying physio-chemical conditions during pyrite growth in this phase.

Elevated Au levels and coincident Bi and Te along with discrete electrum occur independently of lattice bound signatures (Ni-Co) in Py_3 and cross-cut oscillatory growth zones. Such enrichments are found within fractures and cataclastic zones healed by pyrite (Py_4), cross-cutting Py_1, Py_2 and Py_3. This phase is petrographically indistinguishable from earlier phases, but is indicated by local enrichments in Au, Bi and Te along linear features.

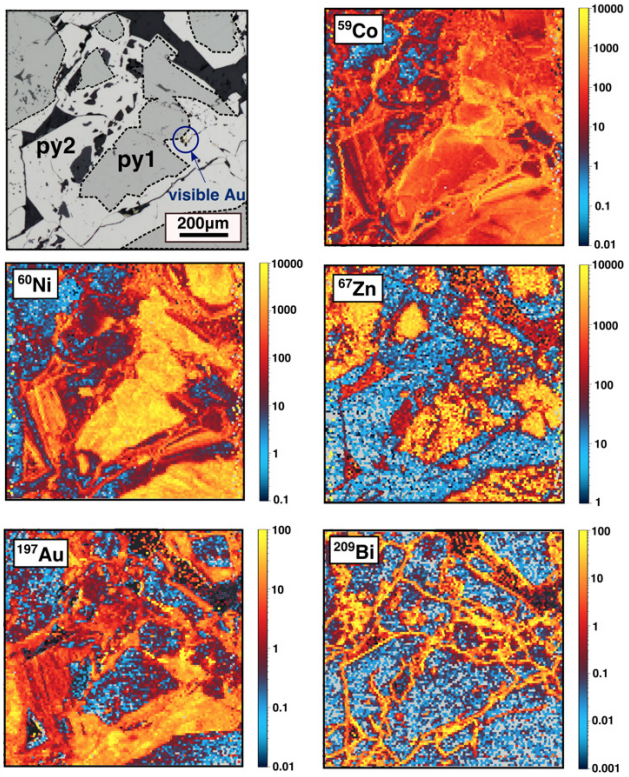

Figure 6. LA-ICP-MS element mapping reveals an early Zn-Ni signature in Py_1, while enrichment in Au is observed in Py_2. Late fractures exploiting the boundary of Py_1 and cross-cutting both phases are enriched in Bi, along which minor electrum is observed in reflected light. All values are in ppm.

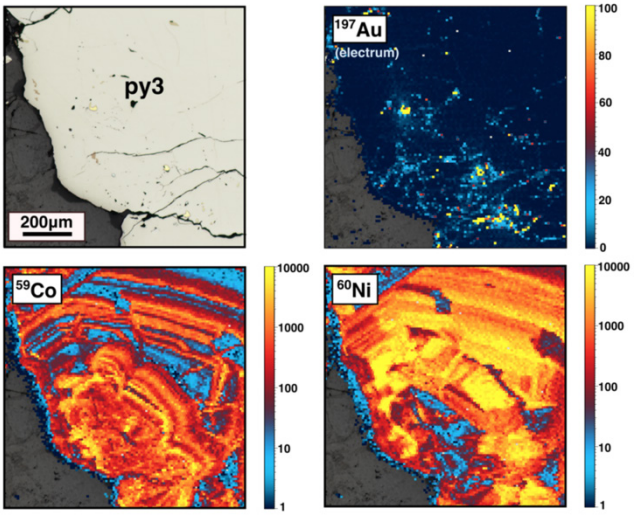

Figure 7. Compositional zonation of ore-stage Py_3 is observed through mapping of Co and Ni. Au is observed within late fractures. All values are in ppm.

4 Summary of findings

This study demonstrates that multiple phases of metalliferous deposition are recorded at Curraghinalt and that a change from a Zn-Ni fertile source (Py_1) to one bearing a Au signature is recorded early (Py_2) in the paragenetic sequence of pyrite. We propose that Au was mobilized with Bi and Te coincident with post-peak metamorphic conditions into late fractures which cross-cut Py_{1-3}.

The timing of auriferous fractures post-Py_3 suggests metamorphic devolatilization reactions, which release H_2O, S, CO_2 and Au during orogenesis, as a likely mechanism for the mobilization of Au into these fractures; such fluids migrate preferentially into pre-existing shears and fracture zones (Phillips and Powell, 2010). We propose that paragenetically constrained pyrite in Dalradian strata records a geochemical fingerprint (Au-Bi-Te) of orogenic fluids depositing Au across the Grampian orogen and may have practical use as an exploration tool for the prediction of Au emplacement.

Acknowledgements

We are grateful to Dalradian Gold Ltd. for access to the Curraghinalt drill-core inventory, for their contributions, feedback and support. At the Trinity College Dublin Geology Department, we would particularly like to thank Cora McKenna, Gary O'Sullivan, Thomas Riegler, Paul Guyett, David Chew, Colin Reid and Leona O'Connor whose advice was much appreciated. This study is funded through the Irish Centre for Research in Applied Geosciences (iCRAG) by Science Foundation Ireland (SFI) (grant number 13/RC/2092) together with European Developments Funds and industry funding partners.

References

Chew, D. M. & Stillman, C. J. 2009. Late Caledonian orogeny and magmatism. In: Holland, C. H. & Sanders, I. S. (eds.) Geology of Ireland. Edinburgh: Dunedin Press.

Daly, J., Holland, C. & Sanders, I. 2009. The Geology of Ireland. Earls, G., Hutton, D., Wilkinson, J., Moles, N., Parnell, J., Fallick, A. & Boyce, A. 1996. The gold metallogeny of northwest Northern Ireland. Geological Survey of Northern Ireland Technical Report, 96:107.

Fettes, D. 1979. A metamorphic map of the British and Irish Caledonides. Geological Society, London, Special Publications, 8:305-321.

Phillips, G. & Powell, R. 2010. Formation of gold deposits: a metamorphic devolatilization model. Journal of Metamorphic Geology, 28:689-718.

Rice, C. M., Mark, D. F., Selby, D., Neilson, J. E. & Davidheiser-Kroll, B. 2016. Age and Geologic Setting of Quartz Vein-Hosted Gold Mineralization at Curraghinalt, Northern Ireland: Implications for Genesis and Classification. Economic Geology, 111:127-150.

SRK Consulting (Canada) Inc. (2018) Technical Report for the Curraghinalt Gold Project, Northern Ireland. Online

* The 2018 resource update (SRK Consulting (Canada), 2018) reports 6.35 Mt at 15.02 g/t for 3.066 Moz contained Au in the indicated categories, with 7.72 Mt at 12.24 g/t for 3,038 Moz contained Au in the inferred category. Further details are available at https://dalradian.com/curraghinalt-project/resources/

Gold mineralization in the Mesoproterozoic Karagwe-Ankole belt (Byumba, Rwanda): new insights from petrography and trace element mapping

Sander Wouters, Philippe Muchez
KU Leuven, Department of Earth & Environmental Sciences, Belgium

Stijn Dewaele
Ghent University, Department of Geology, Belgium

Pim Kaskes, Philippe Claeys
Vrije Universiteit Brussel, Department of Chemistry, Analytical, Environmental and Geo-Chemistry, Belgium

Abstract. A recent increase of interest in the various mineral deposits of the Central African Karagwe-Ankole belt (KAB) has led to many new discoveries and exciting research. Gold deposits in the KAB still have many unanswered questions concerning their formation conditions. The aims of this research are to determine the controlling factors on gold distribution at the Byumba deposit (Rwanda) and to resolve the relationship between the different vein generations and the tectonic evolution of the area. To achieve this, drill cores from the Byumba deposit were logged and sampled for further petrographic research and major and trace element mapping. Micro X-ray fluorescence (μXRF) is used for the identification and distribution of gold and of different types of alteration/mineralization. Five main phases of quartz veining are identified which can be linked to the different phases of deformation that are recognized in the KAB. Important phases of folding and shearing are distinctly present at Byumba and associated with sericitization and chloritization. Sulfides are predominantly present in the form of pyrite, with minor associations of arsenopyrite, chalcopyrite, pyrrhotite and covellite. Primary gold mineralization seems to be correlated to chlorite-rich shear veins. Gold occurs within an early quartz phase and not associated with pyrite.

1 Introduction and geological setting

Gold mineralization in the Central African Karagwe-Ankole belt (KAB) has been the subject of much debate (Brinckmann et al. 1994; Pohl et al. 2013; Koegelenberg et al. 2016). Notwithstanding decades of research, uncertainties concerning the metal source, fluid evolution and timing of the gold mineralization remain. In addition to gold, the Mesoproterozoic KAB is known for hosting spatially associated Nb-Ta, Sn and W deposits, making it an important metallogenic province in Central Africa (Pohl and Günther 1991; Fernandez-Alonso et al. 2012). It encompasses the eastern part of the Democratic Republic of Congo (DR Congo), northwest Tanzania, southwest Uganda, Burundi and Rwanda. Investigations after the metal source for the Nb-Ta-Sn-W mineralization hosted in pegmatites, greisens and peribatholitic quartz veins revealed a genetic link between the Nb-Ta-Sn-W mineralization and the early-Neoproterozoic leucogranites (Dewaele et al. 2011; Hulsbosch et al. 2016).

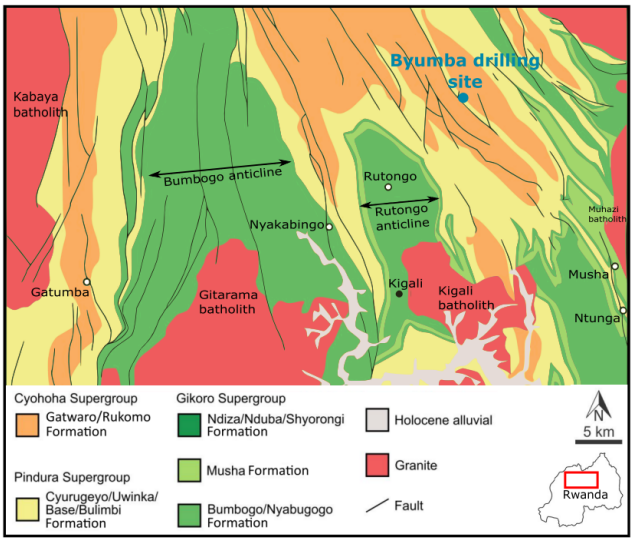

Figure 1. Geological map of central Rwanda with indication of the Byumba drilling site and the neighboring Nyakabingo W and Rutongo Sn type-localities for Kibaran granite-related deposits (after Fernandez Alonso, 2007).

Central African orogenic gold mineralization has in general been linked to fold-and-thrust belt formation (Brinckmann et al. 1994; Koegelenberg et al. 2016). An exact age for this deformation stage and associated gold mineralization is however still under debate. Koegelenberg et al. (2015) defined an age of ~ 1326 Ma in the eastern domain of the KAB, where gold mineralization in north-western Tanzania is clearly not associated with magmatic intrusions (Koegelenberg et al. 2016). In contrast, a late Mesoproterozoic (1000-950 Ma) deformation is proposed by many different studies (Tack et al. 2010; Fernandez-Alonso et al. 2012; Pohl et al. 2013). The overlap in timing between deformation and G4 granite magmatism at 986 ± 10 Ma (U-Pb SHRIMP on zircons from the DR Congo; Tack et al., 2010) may suggest a possible genetic link. Important pegmatite Nb-Ta-Sn mineralization is associated with the latter

magmatism (Hulsbosch et al., 2016); as well as the W-Sn vein-type deposits (Dewaele et al. 2015). Fluid inclusion studies of Sn, W and Au quartz veins by Pohl and Günther (1991) suggest that as opposed to Sn and W, Au mineralization is not caused by the 986 ± 10 Ma G4 magmatism, but related to deep crustal metamorphism. The latter would have been induced by crustal thickening immediately preceding granitoid magmatism and associated mineralization. In addition, there are ferruginous breccia zones which have been dated at 640 ± 28 Ma and are linked to Pan-African events (Rb-Sr muscovite-tourmaline; Brinckmann et al. 1994). Also Ar-Ar dating of muscovite from quartz-sulfide-gold saddle reefs at the Twangiza deposit (Kivu, DRCongo) gives a Pan-African age of 522 ± 15Ma (Ar-Ar; Walemba 2001). To resolve this long-lasting discussion, the study of the gold occurrence at the Byumba deposit (Rwanda) forms a great opportunity to investigate the gold distribution and its relationship with the typical veins, minerals and tectonic evolution of the KAB. In this study, µXRF element mapping is used for the identification and distribution of gold and the relationship with different types of alteration/ mineralization.

2 Methodology

The Byumba gold deposit is situated ~40 km NNE of Kigali in the northern part of Rwanda, and was recently discovered by Desert Gold Ventures Inc. (Figure 1). Detailed core logging was performed on explorative drillings from the Byumba site with a focus on lithological variations, alteration, deformation structures, different vein generations and their relation to the ore grade. In total 9 drill cores (± 1800 m) were logged and sampled for further petrographic investigation with thin and polished sections.

The major and trace element distributions and semi-quantitative abundance within thick, thin and polished sections were mapped using the Bruker M4 Tornado Micro X-ray fluorescence (µXRF) scanner, available at the Vrije Universteit Brussel (de Winter et al. 2017). The measurements were executed using a Rh source and two XFlash 430 Silicon Drift detectors under vacuum conditions (20 mbar), with short acquisition times per spot size (1 ms per 25µm) and maximized source energy settings (600µA, 50kV). No sample coating is required and the method is fully non-destructive. This high-resolution technique offers the opportunity to search for “invisible gold”, which is gold that could not be detected by means of standard petrographic microscopy.

3 Results and discussion

3.1 Lithology, vein generations and tectonic setting

Lithologically, the drill cores of the Byumba deposit consist of alternations of sand- to siltstones with organic-rich shales. Multiple quartz vein generations are

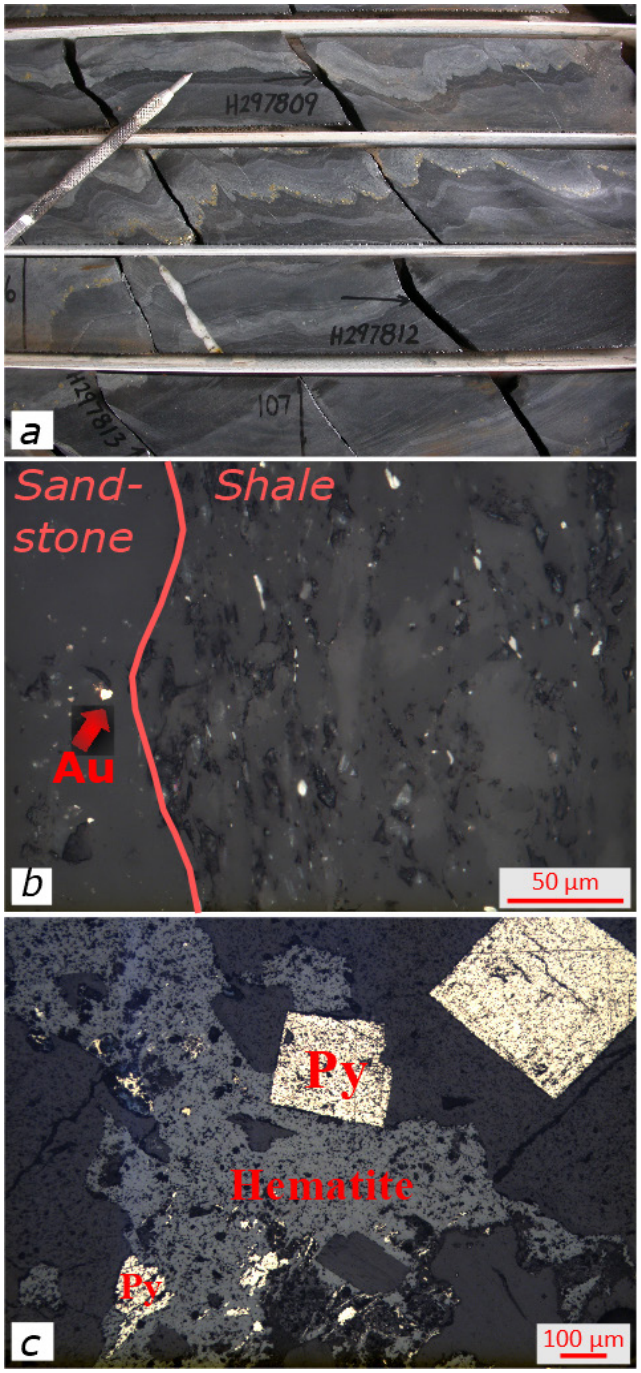

Figure 2. a) General overview of a core from the Byumba deposit. Notice the folded and sheared lithology with an early generation of pyrite and a boudinaged shear vein parallel to the foliation. Incident light microphotographs: Hardness stick of 15cm for scale. b) Host rock with gold mineralization at the contact between a sandstone and shale lithology. b) Early anhedral generation of pyrite (Py) which is replaced by euhedral pyrite and intensely hematized.

identified within these metasediments, which underwent intense folding and shear deformation (see Figure 2a). Cleavage is well developed and dominantly axial planar. In mica-rich phyllites the cleavage can be crenulated. Alteration at the Byumba deposit is present in the form of pervasive chloritization, some sericitization, silicification and carbonatization.

The first quartz vein generation in the paragenesis of

the Byumba deposit is parallel to and folded along with the bedding, which is indicative of a pre-folding origin. Massive quartz veins, concentrated in the hinge zones of folds, are associated with massive pyrite and represent a second generation of veining, which is related to folding. In addition, some irregular and thin chlorite-rich veins also occur in fold hinges, but they have a more widespread distribution in the metasedimentary rocks. A third generation of quartz veins is found in fault-related fractures or along the faults themselves. Fourth generation quartz veins occur parallel to the cleavage and may occasionally be boudinaged, which indicates formation after folding and cleavage development. This quartz vein generation also crosscuts the sandstones at an angle of 45°-60°. This orientation gives these quartz veins, in combination with the cleavage parallel-nature of the veins, a sigmoidal geometry. Based on mineralogical variations, a minimum of two distinct sigmoidal quartz vein generations can be identified. The earliest generation is primarily composed of quartz, chlorite and sericite. Sigmoidal quartz and Fe-rich carbonate veins crosscut the former, implying a younger age. The presence of shear zones and sigmoidal quartz veins are an expression of a distinct shearing phase which post-dates folding and cleavage development. Intense chloritization and silicification and the occurrence of C'-type shear bands are related to this shearing. Meter-thick massive quartz veins which crosscut the folds, cleavage and the aforementioned quartz generations represent a final vein generation. Host-rock fragments are frequently enclosed inside these veins, which therefore embody a brecciation phase.

3.2 Mineralization

The main sulfide mineral at the Byumba deposit is pyrite. Other sulfides include arsenopyrite, chalcopyrite, pyrrhotite and covellite. Numerous pyrite generations occur in the metasediments and quartz veins. Many of these pyrites show evidence of resorption and sieve textures. Early pyrite generations are anhedral and contain inclusions of chalcopyrite. The presence of quartz-filled pressure shadows surrounding some of these pyrites is evidence for a pre-deformation origin. Euhedral pyrites are younger and associated with inclusions of pyrrhotite (see Figure 2c). Several of the later pyrite generations are associated with folding and shearing deformation phases. A distinct correlation between the late shear-related carbonatization and large euhedral pyrites illustrates this relationship.

Logging of the gold grade distribution revealed a correlation between shear zones and the gold content. This is further evidenced by µXRF results which show that the gold is hosted by an early dark grey quartz phase inside chlorite-rich shear veins (see Figure 3). Gold is often present in the form of invisible gold inside quartz but has very occasionally been microscopically observed as small disseminated blebs. The dark grey quartz phase which hosts the gold is an early expression of silicification in the generation of shear quartz veins. The milky white quartz is a later quartz phase of the same shear vein generation. None of the different pyrite generations present in the shear veins show an enrichment in gold on the element maps. No gold has been microscopically observed in the sulfides. In addition, µXRF shows a correlation between the gold and arsenic content of enriched zones inside the quartz veins and the host rocks. The latter may also be expressed by the presence of arsenopyrite inside the shear veins.

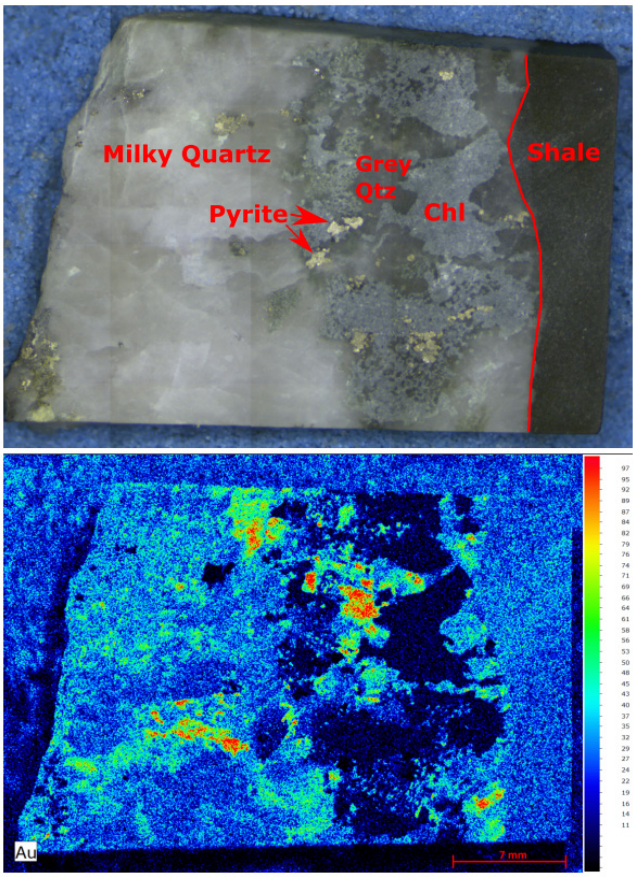

Figure 3. (Top): Chlorite-rich shear vein with indication of a relatively early dark grey quartz phase and a later milky white quartz phase. (Bottom): µXRF Au heat map of the chloritized shear vein which shows an enrichment in the early grey quartz phase.

Gold blebs are also found at sandstone/shale lithological contacts (see Figure 2b). These are difficult to place in the paragenesis of mineralization due to their disseminated nature and non-association with a specific mineral phase. A secondary gold enrichment stage may be proposed by the presence of the high ore grade at the oxidation/reduction zone boundaries at specific depths in the studied drill cores.

4 Conclusion

The relative timing, paragenesis and character of the different quartz vein generations at the Byumba deposit can be compared with quartz veins studied at other deposits in Rwanda. At the Nyakabingo W-deposit, three different types of quartz veins are identified (Dewaele et al. 2016), which may correspond to the pre-folding and the often massive cleavage parallel shear veins observed in this study. The folding of the metasediments and early

quartz vein generations indicate a pre- to early orogenic origin for the latter. After folding and cleavage development a pervasive phase of shearing causes the formation of the cleavage parallel or sigmoidal quartz veins. The aforementioned shearing, which is also associated with brecciation, is recognized in various deposits around the KAB (Pohl and Günther 1991). W and Sn mineralization thus shows similar pre- and syn- to post-deformation veins as found at the Byumba gold deposit, but a direct correlation is still difficult to make.

Gold occurs in the form of invisible gold and in the form of small disseminated blebs. The presence of gold is accompanied by an enrichment in the arsenic content of the quartz and the presence of arsenopyrite. The observed textures of the pyrite point to sulfide recrystallization and remobilization which is often associated with low gold content in orogenic-type and metamorphosed gold deposits (Cook et al. 2009). Supergene enrichment of gold is identified at oxidation/reduction zone boundaries based on the ore grade variation inside the boreholes. Secondary gold mineralization is also identified by Brinckmann et al. (1994), which links the redistribution of the gold to Pan-African structural reactivation.

Acknowledgements

We would like to thank Desert Gold Ventures Inc., Francis Gatare and Alain Ntenge from the Rwanda Mines, Petroleum and Gas Board for their collaboration and contribution. This research is financially supported by Research Grant C14/17/056 of the KU Leuven Research Fund. P. Claeys thanks Research Foundation Flanders - Hercules Program for financing the Micro-XRF instrument

References

Brinckmann J, Lehmann B, Timm F (1994) Proterozoic gold mineralization in NW burundi. Ore Geol Rev 9:85–103

Cook NJ, Ciobanu CL, Mao J (2009) Textural control on gold distribution in As-free pyrite from the Dongping, Huangtuliang and Hougou gold deposits, North China Craton (Hebei Province, China). Chem Geol 264:101–121

Dewaele S, Henjes-Kunst F, Melcher F, et al (2011) Late Neoproterozoic overprinting of the cassiterite and columbite-tantalite bearing pegmatites of the Gatumba area, Rwanda (Central Africa). J African Earth Sci 61:10–26

Dewaele S, Muchez P, Burgess R, Boyce A (2015) Geological setting and timing of the cassiterite vein type mineralization of the Kalima area (Maniema, Democratic Republic of Congo). J African Earth Sci 112:199–212

de Winter NJ, Sinnesael M, Makarona C, Vansteenberge S, Claeys P (2017) Trace element analyses of carbonates using portable and micro-X-ray fluorescence: performance and optimization of measurement parameters and strategies. Journal of Analytical Atomic Spectrometry *32*(6):1211-1223

Fernandez-Alonso M, (2007) Geological Map of the Mesoproterozoic Northeastern Kibara Belt. Royal Museum for Central Africa, Tervuren, Belgium

Fernandez-Alonso M, Cutten H, De Waele B, et al (2012) The Mesoproterozoic Karagwe-Ankole Belt (formerly the NE Kibara Belt): The result of prolonged extensional intracratonic basin development punctuated by two short-lived far-field compressional events. Precambrian Res 216–219:63–86

Hulsbosch N, Boiron MC, Dewaele S, Muchez P (2016) Fluid fractionation of tungsten during granite-pegmatite differentiation and the metal source of peribatholitic W quartz veins: Evidence from the Karagwe-Ankole Belt (Rwanda). Geochim Cosmochim Acta 175:299–318

Koegelenberg C, Kisters AFM, Harris C (2016) Structural controls of fluid flow and gold mineralization in the easternmost parts of the Karagwe-Ankole Belt of north-western Tanzania. Ore Geol Rev 77:332–349

Koegelenberg C, Kisters AFM, Kramers JD, Frei D (2015) U-Pb detrital zircon and ^{39}Ar-^{40}Ar muscovite ages from the eastern parts of the Karagwe-Ankole Belt: Tracking Paleoproterozoic basin formation and Mesoproterozoic crustal amalgamation along the western margin of the Tanzania Craton. Precambrian Res 269:147–161

Pohl W, Günther MA (1991) The origin of Kibaran (late Mid-Proterozoic) tin, tungsten and gold quartz vein deposits in Central Africa: a fluid inclusions study. Miner Depos 51–59

Pohl WL, Biryabarema M, Lehmann B (2013) Early Neoproterozoic rare metal (Sn, Ta, W) and gold metallogeny of the Central Africa Region: a review. Appl Earth Sci 122:66–82

Tack L, Wingate MTD, De Waele B, et al (2010) The 1375 Ma “Kibaran event” in Central Africa: Prominent emplacement of bimodal magmatism under extensional regime. Precambrian Res 180:63–84

Walemba KMA (2001) Geology, geochemistry, and tectono-metallogenic evolution of neuproterozoicgold deposits in the Kadubu area, Kivu, Democratic Republic of Congo.Faculty of Science,University of the Witwatersrand

The source of Au in Paleoproterozoic orogenic gold deposits: insight from the Central Lapland Greenstone Belt, Finland

Patten C.G.C., Kolb J.
Institute for Applied Geosciences, Department of Geochemistry and Ore Geology, KIT, Karlsruhe, Germany

Molnár F.
Geological Survey of Finland, Espoo, Finland

Pitcairn I.K.
Department of Geological Sciences, Stockholm University, Stockholm, Sweden

Abstract. Paleoproterozoic greenstone belts are prospective terranes for orogenic Au deposits worldwide and yet the source areas of the metals enriched in these deposits are not well characterized. In this study we investigate the role of metavolcanic rocks as the potential source of Au in the Paleoproterozoic Central Lapland Greenstone Belt, Finland. The metavolcanic rocks in this belt show mainly MORB and WPB character. The WPB have higher primary Au content than MORB due to a plume component. Using fresh MORB and WPB data as proxy for protolith composition, mass variation calculation shows that up 68±39% of the initial metavolcanic Au content is lost during upper amphibolite facies metamorphism (>550 °C). Mass balance calculation indicates that up to ~2640 t of Au has been mobilized during metamorphism which is one order of magnitude higher than the ~280 t Au endowment in the deposits. Metavolcanic rocks appears thus as fertile sources for Au in Paleoproterozoic greenstone belts. Moreover, this study highlights the importance to consider the type of metavolcanic rocks present within greenstone belts as they partly control the Au fertility of the source areas.

1 Introduction

Orogenic gold deposits are the product of complex large-scale processes which include the production of metal-rich fluids, the transport of these metal-rich fluids through the Earth's crust, and the precipitation of the metals in structurally controlled sinks at various degree of metamorphism (Pitcairn et al. 2006a; Kolb et al. 2015; Goldfarb and Groves 2015). Recognition of geological formations as sources of metals, ligands or ore-forming fluids is an important step for understanding hydrothermal ore deposit formation. Although the mechanisms responsible for Au precipitation in orogenic gold deposits are fairly well constrained, the sources of the metals are still debated (Goldfarb and Groves 2015). In Phanerozoic orogenic gold deposits, metasedimentary units are the principal Au source (Pitcairn et al. 2006a, 2015) but in Precambrian greenstone belts, the scarcity of metasedimentary rocks and the abundance of metavolcanic rocks hint that the latter could also be a potential Au source (Goldfarb and Groves 2015; Augustin and Gaboury 2017). However, this has not been clearly demonstrated yet.

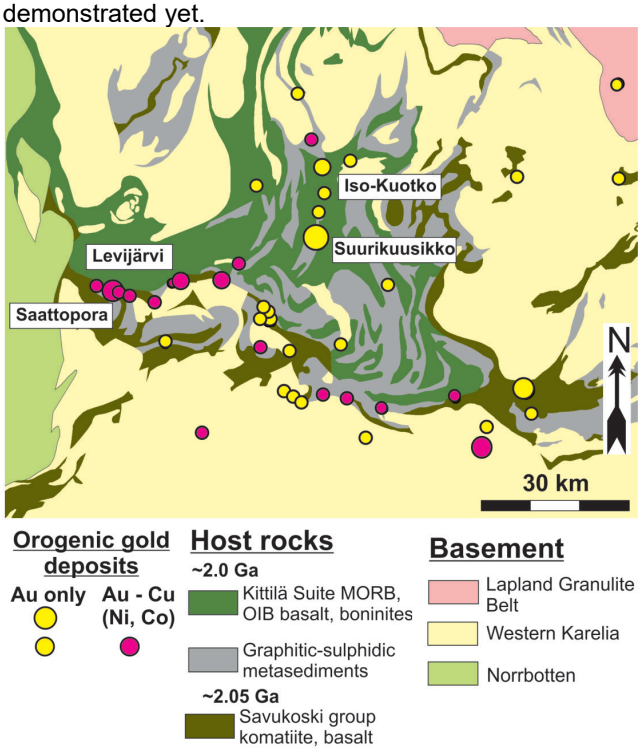

Figure 1. Geological map of the CLGB and associated orogenic Au deposits.

The Central Lapland Greenstone Belt (CLGB), in Northern Finland, consists of a sequence of metamorphosed mafic-ultramafic and marine sedimentary rocks related to the rifting of the Karelian craton (Fig 1). The CLGB is one of the largest known Paleoproterozoic greenstone belt (Hanski and Huhma 2005) and is an excellent target to study the source of Au in Paleoproterozoic orogenic Au deposits. The most voluminous mafic-ultramafic volcanic units occur in two main groups: the Kittilä and Savukoski groups (Fig. 1). The Kittilä group (gp) is dominated by mid-oceanic ridge basalts (MORB) and within plate basalts (WPB) with minor high magnesian basalts. It is interpreted as the remaining of thrusted oceanic crust (Hanski and Huhma 2005). The Savukoski gp is dominated by

metasedimentary rocks and the metavolcanic rocks are characterized by komatiites, WPB and minor MORB. It is interpreted that these rocks were deposited in the continental margin rift zones of the Karelian craton (Hanski and Huhma 2005). The CLGB displays a relatively complex metamorphic pattern but it can be simplified into a zonation where the core of the belt is metamorphosed to greenschist facies while the borders are metamorphosed to mid-amphibolite facies up to granulite facies (Hanski and Huhma 2005).

The CLGB hosts numerous orogenic gold deposits, which are characterized by typical (Au-only) and atypical (Au-Cu ± Co, Ni, Mo, U) metal associations (Eilu et al. 2007). Most of the deposits formed under similar pressure-temperature conditions at 300-450 °C and 1-3 kbar and in similar lithological and structural settings.

In this study we investigate the potential role of metavolcanic rocks as the source for the Au and other elements enriched in the orogenic Au deposits. We specifically focus on the source of Au in the Kittilä group and on metal mobilization from MORB and WPB samples during metamorphism.

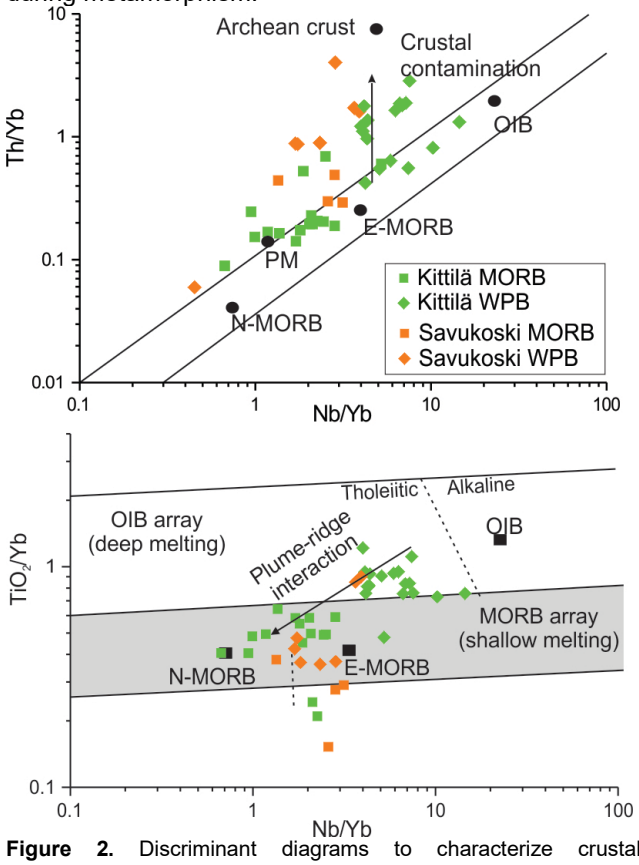

Figure 2. Discriminant diagrams to characterize crustal contamination and plume component in CLGCB metavolcanics. Modified from Pearce (2008).

2 Methodology

Sixty eight metavolcanic rock samples from 26 unmineralised drill cores from the archives of the Geological Survey of Finland (GTK) have been collected for the purpose of this study. The drill core locations are widespread throughout the CLGB and the samples are representative of the various lithologies and metamorphic facies present in the Kittilä and Savukoski groups ranging from greenschist facies (~250 °C) to upper amphibolite facies (>550 °C). Major and trace elements were analyzed by ALS Global. Major elements were analyzed by XRF, trace elements by ICP-MS or ICP-AES and S and C by Leco Furnace. Ultra-low detection limit Au method (Pitcairn et al. 2006b) was carried out at Stockholm University. The CANMET reference material TDB-1 and USGS reference material CH-4 were analyzed for data quality control and yield accuracy of 3.3 % and 10.5 % and precision of 11.8 % and 26.3 % respectively.

3 Whole rock data

Metavolcanic rocks from the Kittillä and Savukoski groups are characterized by mid-oceanic ridge basalt (MORB, n=19), within plate basalt (WPB, n=25), komatiites (n=16) and boninites (n=6). The Kittilä MORB samples are basalts (40-52 wt.% SiO_2) and basaltic andesites (52-57 wt.% SiO_2) with tholeiitic to transitional affinity (Zr/Y<3.86 and Th/Yb<0.69) and have relatively flat REE profiles (La/Yb_{pm}=1.72±0.7). Similarly, Savukoski MORB samples are basalts with tholeiitic to transitional affinity (Zr/Y<3.24 and Th/Yb<0.49) and have relatively flat REE profiles (La/Yb_{pm}=1.91±1.81). The MORB samples from the Kittilä gp and Savukoski gp have a median value of 0.61 ppb Au (0.15-8.39 ppb), 1420 ppm S (26-6520 ppm) and 0.99 ppm As (0.20-82.1 ppm).The WPB samples from the Kittilä gp are also basalts and basaltic andesites but have slightly higher Na_2O+K_2O content than the MORB samples (3.9±1.1 wt.%). They have transitional to calc-alkaline affinity (Zr/Y>4.61 and Th/Yb>0.42), LREE enrichment (La/Yb_{pm}=5.91±2.75) and significant Ta and Nb negative anomalies (Ta/Th_{pm}=0.24±0.09 and Nb/Th_{pm}=0.38±0.43). Similarly, the Savukoski WPB samples have transitional to calc-alkaline affinity (Zr/Y>4.61 and Th/Yb>0.42), LREE enrichment (La/Yb_{pm}=6.3±1.81) and significant Ta and Nb negative anomalies (Ta/Th_{pm}=0.69±0.36 and Nb/Th_{pm}=0.76±0.45). The WPB samples have a median of 0.75 ppb Au (0.19-17.1 ppb), 946 ppm S (26-6050 ppm) and 2.11 ppm As (0.63-77 ppm).

4 Discussion

4.1 Tectonic setting

Although the MORB and WPB samples from the Kittilä and Savukoski groups formed sin different tectonic environments and timing (Hanski and Huhma 2005) the similarities in major and trace element chemistry imply similar magmatic processes. The tholeiitic affinity of MORB samples from the Kittilä gp and their relatively flat REE profiles indicate a transitional MORB affinity corresponding to the Vesmajärvi formation (Hanski and Huhma 2005). The MORB samples are likely sourced from the primitive mantle (Fig. 2). The Savukoski MORB samples have a slight Th/Yb anomaly implying little crustal contamination while Kittilä MORB do not (Fig. 2).

In the KIttilä gp, the transitional to calc-alkaline affinity and the LREE enrichment of WPB samples are

characteristic of the Kautoleskä formation (Hanski and Huhma 2005). The WPB samples show significantly higher Th/Yb anomaly relative to MORB implying a stronger crustal contamination (Fig. 2). The WPB basalts are likely sourced from an enriched mantle source and high TiO_2/Yb values imply a plume component for the WPB samples (Fig. 2). This indicate gradual evolution from plume-related and continental crust-contaminated volcanic rocks (Savukoski, komatiite and WPB dominated) to primitive mantle-related volcanic rocks (Kittilä, MORB dominated) during the transition from the latest rifting stages of the Karelian craton to oceanic crust type environment (Hanski and Huhma 2005).

4.2 Metavolcanic protolith composition

To determine the potential of mafic metavolcanic rocks as the source of Au it is paramount to constraining their primary magmatic content and the possible differences between MORB and WPB. We use 128 fresh glass data from Tatsumi et al. (1999) and Jenner and O'Neill (2012) along with our samples in order to better characterize Au behavior during magmatic evolution. Two different magmatic trends are calculated for MORB and WPB using Zr/Y ratios (Fig. 3) and these are used as proxy for Au protolith composition (Jowitt et al. 2012; Patten et al. 2016). Gold is strongly compatible during differentiation in MORB melts due to sulfide segregation (Fig. 3). In WPB, on the contrary, Au content is higher due to plume component (Webber et al. 2013) and constant during melt differentiation due to limited sulfide segregation (Fig. 3; Tatsumi et al. 1999).

During oceanic crust migration from the ridge to the orogen, the oceanic crust sustains seafloor alteration, mostly at greenschist facies. Seafloor alteration leads to Au re-distribution within the volcanic section and partial depletion in the sheeted dyke and plutonic complexes (Patten et al. 2016). Sulfur and As, unlike Au, are highly mobile elements during seafloor alteration and significant remobilization or enrichment can occur (Patten et al. 2016). The effect of seafloor alteration is highlighted by the wide S range (200-6500 ppm S) and high As concentrations (median=10.3 ppm) of MORB and WPB greenschist facies samples relative to fresh ones (640-1890 ppm S and median=0.18 ppm As; Jenner and O'Neill 2012). Magmatic differentiation trends, thus, cannot be used as proxies for protolith composition and median values of greenschist facies samples (1350 ppm S and 10.3 ppm As) are used instead.

4.3 Mobilization during metamorphism

To accurately quantify the Au variation due to metamorphism it is necessary to account for the protolith variation. To do so we use the method described in Jowitt et al. (2012) and mass changes are calculated from the magmatic differentiation curves using the following relationship:

$$\Delta Au = Au_c - Au_s$$

where ΔAu is the Au mass change, Au_c the calculated protolith Au composition and Au_s the measured Au value (Fig. 4). The Au mass variation uncertainty ($\delta\Delta Au$=±37.7 %) is the quadrature addition of the MORB and WPB mass variation uncertainty which in turn is the quadrature addition of the normalized root mean square deviation of the magmatic trends (δAu_c=±19.7 and ±31.8 % for MORB and WSP respectively) and analytical uncertainty (δAu_S=±3.3%, using TDB-1). This mass balance uncertainty is high but is inherent to the uncertainty of Au distribution in the primary volcanic rocks.

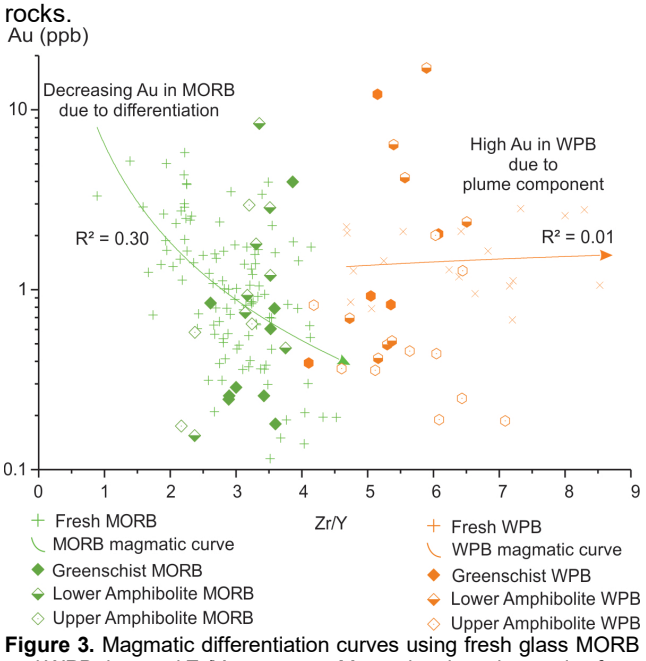

Figure 3. Magmatic differentiation curves using fresh glass MORB and WPB data and Zr/Y as a proxy. Metavolcanic rock samples from the CLGB are plotted according to their metamorphic grade.

Gold mass change in the greenschist facies samples (median=-37%, Fig. 5) and in the lower amphibolite facies (median=40%. Fig. 5) are too close to the Au mass variation uncertainty to be considered meaningful. For instance the apparently low value of the greenschist facies samples is strongly affected by 5 MORB samples with low Au content (0.18-0.39 ppb) but which are nevertheless within the MORB compositional array (Fig. 5). On the opposite, the apparently high value of the lower amphibolite facies samples is positively skewed by 5 samples with high Au content (2.85-17.1 ppb) most likely due to Au remobilization and local enrichment during seafloor alteration (Patten et al., 2016) or later overprint. Only the upper amphibolite facies samples show important enough mass variation (median=-68%) to be significant (Fig. 5). Additionally upper amphibolite facies samples have smaller Au range (0.17-2.95 ppb) than the greenschist and lower amphibolite facies samples (0.18-12.2 ppb and 0.15-17.1 ppb respectively) characteristic of Au mobilization during metamorphism (Pitcairn et al. 2006a, 2015). The S and As concentrations in upper amphibolite facies samples (median = 500 ppm S and 0.87 ppm As) are significantly lower than in the greenschist facies samples and yield depletion of 63 % and 92 % respectively due to metamorphism.

Combination of the Au, S and As mass variations and 3D modeling of the Kittilä terrane (Niiranen et al. 2015) enables to better constrain elemental fluxes during metamorphism in the CLGB. Niiranen et al. (2015) estimated that up to 1500 km^3 of the Kittilä gp base has

been metamorphosed to upper amphibolite facies (>550 °C). The metavolcanic proportion in the Kittilä gp is estimated at 85% (Niiranen, pers. com.) which correspond to $3.6*10^6$ Mt of rocks using a density of 2700 kg.m³. Mass balance calculation using a protolith composition of 1.06 ppb Au (median value of both fresh MORB and WPB) indicates that up to ~2640 t of Au (~84 Moz) has been mobilized during metamorphism. This estimation is lower than that estimated by Niiranen et al. (2015) of 4425-7080 t Au but still one order of magnitude higher than the total reported Au endowment of the CLGB orogenic Au deposits (~280 t). Mass balance calculation of S and As indicates that up to $3.1*10^3$ Mt S and 34 Mt As are also mobilized. The metavolcanics, thus, can also be the source of the S and As despite the presence of S and As rich metasedimentary rocks in the CLGB, which are also potential sources for these elements. The metavolcanic rocks, however, do not show systematic depletion in the metals enriched in orogenic gold deposits with atypical metal association (e.g. Au + Cu, Ni, Co, Mo, U) pointing toward an alternative source and a bi-modal source area system for the metals enriched in the orogenic Au deposits of the CLGB.

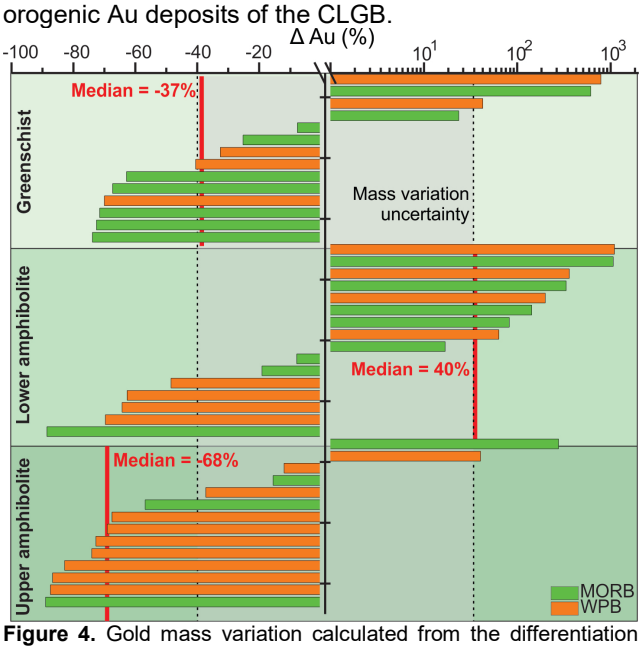

Figure 4. Gold mass variation calculated from the differentiation curves. Only the upper amphibolite samples show meaningful depletion.

4.4 Implication for Paleoproterozoic orogenic Au deposits

This study confirms that metavolcanic rocks can be the source of the Au enriched in Paleoproterozoic orogenic Au deposits (Augustin and Gaboury 2017) on the contrary to Phanerozoic ones where metasedimentary rocks are the dominant source of gold (Pitcairn et al. 2006a, 2015). Additionally, this study highlights the importance of considering the type of metavolcanic rocks present in the greenstone belts and their primary Au fertility. The presence of plume-related WPB in the CLGB significantly increases the primary Au fertility of the metavolcanics. Similarly Augustin and Gaboury (2017) argued that the Au endowment in the Mana district of Man-Leo shield in the West Africa craton, one of the best endowed Paleoproterozoic Au province, is related to the presence of plume-related metavolcanic rocks in the source. Alternatively, calc-akaline magmatic series (andesite to rhyolite) are enriched in Au relative to MORB and can also increase the Au fertility of greenstone belts such as in the Abitibi greenstone belt (Pitcairn et al. this issue).

Acknowledgement

This study was partly funded by the Academy of Finland supported MinSysPro #281670 project and by the Academy of Finland and DAAD travel grant.

References

Augustin J, Gaboury D (2017) Plume-related basaltic rocks in the Mana gold district in western Burkina Faso , West Africa : Implications for exploration and the source of gold in orogenic deposits. J African Earth Sci Paleoproterozoic 129:

Eilu P, Pankka H, Keinänen V, et al (2007) Characteristics of gold mineralisation in the greenstone belts of northern Finland. Geol Surv Finland, Spec Pap 44:57–106

Goldfarb RJ, Groves DI (2015) Orogenic gold: Common or evolving fluid and metal sources through time. Lithos 233:2–26

Hanski E, Huhma H (2005) Central Lapland greenstone belt. In: Lehtinen M, Nurmi PA, Rämö OT (eds) Precambrian Geology of Finland - Key to the Evolution of the Fennoscandian Shield. Elesvier B. V., pp 139–194

Jenner FE, O'Neill HSC (2012) Major and trace analysis of basaltic glasses by laser-ablation ICP-MS. Geochemistry, Geophys Geosystems 13:

Jowitt SM, Jenkin GR, Coogan LA, Naden J (2012) Quantifying the release of base metals from source rocks for volcanogenic massive sulfide deposits: effects of protolith composition and alteration mineralogy. J Geochemical Explor 118:47–59

Kolb J, Dziggel A, Bagas L (2015) Hypozonal lode gold deposits : A genetic concept based on a review of the New Consort , Renco , Hutti , Hira Buddini , Navachab , Nevoria and The Granites deposits. Precambrian Res 262:20–44

Niiranen T, Lahti I, Nykänen V (2015) The Orogenic Gold Potential of the Central Lapland Greenstone Belt, Northern Fennoscandian Shield. In: Mineral Deposits of Finland. Elsevier, pp 733–752

Patten CGC, Pitcairn IK, Teagle DAH, Harris M (2016) Mobility of Au and related elements during the hydrothermal alteration of the oceanic crust: implications for the sources of metals in VMS deposits. Miner Depos 51:179–200

Pearce JA (2008) Geochemical fingerprinting of oceanic basalts with applications to ophiolite classification and the search for Archean oceanic crust. Lithos 100:14–48

Pitcairn IK, Craw D, Teagle DAH (2015) Metabasalts as sources of metals in orogenic gold deposits. Miner Depos 50:373–390

Pitcairn IK, Teagle DAH, Craw D, et al (2006a) Sources of metals and fluids in orogenic gold deposits: insoghts from the Otago and Alpone schists, New Zealand. Econ Geol 101:1525–1546

Pitcairn IK, Warwick PE, Milton JA, Teagle DAH (2006b) Method for ultra-low-level analysis of gold in rocks. Anal Chem 78:1290–1295

Tatsumi Y, Oguri K, Shimoda G (1999) The behaviour of platinum-group elements during magmatic differentiation in Hawaiian tholeiites. Geochem J 33:237–247

Webber AP, Roberts S, Taylor RN, Pitcairn IK (2013) Golden plumes: Substantial gold enrichment of oceanic crust during ridge-plume interaction. Geology 41:87–90

The paragenesis of veining and Au mineralisation at the Barsele Au deposit, Sweden

Evelina Rann, Iain Pitcairn
Department of Geological Sciences, Stockholm University, Sweden

Marcello Imaña, Kåre Höglund
Agnico Eagle Sweden AB

Abstract. The Paleoproterozoic Barsele Au deposit located in Västerbotten, Sweden is a granodiorite hosted deposit with Au mainly associated with multiple phases of quartz veins. The aim of this study is to constrain the sequence of veining and identify the mineralogical and textural host for Au in the veins. Based on form, texture, mineralogy, metal association and trace element concentrations, we identify 2 main vein generations. An early magmatic hydrothermal phase where irregular blue colour quartz with an Au-Mo-Bi metal association gives formation temperatures from titanium-in-quartz geothermometry of 625 ± 75ºC. The main-stage quartz which hosts the bulk of the Au shows textures and trace element concentrations consistent with formation at <350ºC. The Au in the main-stage veins is hosted in areas of recrystallised quartz associated with carbonate and sulphides which possibly formed late or post main-stage veining.

1 Introduction

The Barsele deposit occurs at the junction between the world-class mineralised Skellefte District in the east and the NW-SE "Gold Line" trend that includes the Knaften, Fäboliden, Svartliden, Stortjärnshobben and Blaiken gold deposits (Bark & Weihed, 2007). The Barsele area contains a number of different mineralised zones including the Norra VMS deposit, and three clusters of quartz-Au veins that form the Avan, Central and Skiråsen deposits all of which are hosted in a 1.876 Ga ± 10 Ma early orogenic granodiorite (Thomas et al., 2019).

The aim of this project was to constrain the paragenesis of veining and gold mineralisation in the Qtz-Au vein deposits. We investigate vein textures, cross cutting relationships and the location of gold to identify the temporal evolution of Au mineralisation at the deposit. Vein samples collected from drill cores were further investigated by polarising microscopy and scanning electron microscopy (SEM). Trace elements in quartz were quantified using electron microprobe (EMPA) and used to differentiate between quartz vein generations and possibly constrain the temperature of mineralisation using the titanium-in-quartz geothermometer (Wark & Watson, 2006).

2 Regional geology

The Barsele deposit is located within Palaeoproterozoic 1.9–1.8 Ga supracrustal and related intrusive rocks (Fig. 1) that were deformed and metamorphosed during the Svecokarelian orogeny (Lundström et al., 1997; Mellqvist et al., 1999; Kathol & Weihed, 2005). The lowest stratigraphic unit in the area is the Bothnian Supergroup and consists of metasedimentary and intercalated volcanic rocks (Kathol & Weihed, 2005; Skyttä et al., 2012) and also metadacite dated to an age of 1959±14 Ma (Eliasson et al., 2001). The Bothnian Supergroup forms the basement to the Skellefte Group (1.89-1.88 Ga), of mainly felsic volcanic rocks (Allen et al., 1996) that formed during crustal extension event (**D_1**) by using syn-extensional normal and transfer faults for emplacement (Bauer et al., 2011). The Skellefte Group of volcanic rocks are overlain by the Vargfors group, a dominantly sedimentary unit (1.88 - 1.87 Ga) and the local stratigraphy is comparable to some of the volcanic domains of the Skellefte District. The oldest intrusive rocks in the Barsele area are early orogenic, 1.89-

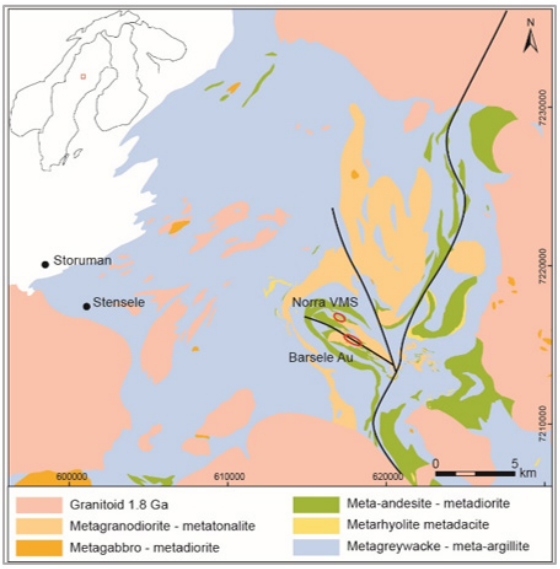

Figure 1. Geological map of the Storuman area. Modified after Kathol et al. (2005) and Krispinsson (2018). Coordinates in SWEREF99. Thick black lines represent major structures in the area. From Bauer et al., 2019).

1.87 Ga, granitoids, diorites and gabbros and these are proposed to be coeval with the volcanic rocks of the Skellefte Group. Younger phases of intrusive rocks including the late- to post-Svecokarelian GSDG-type of the Transscandinavian Igneous Belt (1.82-1.78 Ga) have intruded through the Skellefte, Vargfors and Bothnian Groups (Kathol & Weihed, 2005). At 1.88-1.87 Ga the main compressional deformation event (**D_2**) occurred and caused re-activation of syn-extensional faults and folding

(Bauer et al. 2011). The latest deformation event ($\mathbf{D_3}$) at 1.82-1.80 Ga (Weihed et al., 2002) caused east-west crustal shortening and reactivation of main syn-extensional high-strain zones with reverse kinematics (Bergman Weihed et al., 1996; Bauer et al., 2011; Skyttä et al., 2012) that has generated the classified orogenic gold deposits at 1.80 Ga (Bark & Weihed, 2007).

3 Vein characteristics and trace element analysis

The quartz veins at Barsele have been previously categorised based on mineralogy, texture and accompanying alteration into five types (Unpublished report, Imaña, 2016); Qtz-0 - irregular wormy shaped vein types, often with a distinct blue colour that are cross-cut by all other veins (Fig. 2A), Qtz-1 - sinuose quartz ± carbonate veins, 0.5 to 30 cm in width (Fig. 2C), Qtz-2 - planar quartz veins with distinct alteration selvages from chlorite, biotite and centreline carbonate infill, Qtz-3 - show some of the characteristics of Qtz 1 and 2 but contain visible Au and/or scheelite, and Qtz-4 – polymetallic quartz-carbonate veins that are very sulphide rich containing mainly sphalerite, pyrrhotite and galena with rare pyrite (Fig. 2G).

Based on our microscopy we can distinguish 2 main vein generations; ***early-stage*** and "***main-stage***" veining. The early-stage veins (Qtz-0) have a distinct form and colour and comprise fine grained polycrystalline quartz with irregular grain boundaries formed by grain boundary migration (Passchier & Trouw, 2005). They contain visible Au as electrum which is spatially associated with molybdenite, chalcopyrite, BiPbS minerals and native Bi (Fig. 2B). Based on similarities in vein form, cross-cutting relationships, texture and mineralogy we suggest that Qtz-1 to Qtz-4 vein groups at Barsele represent a continuum of vein injection which due to being the most abundant veins in the deposit we refer to as main-stage veining. There are differences between these vein groups, such as the sulphide content in the Qtz-4 veins (Fig. 2G and H), but the quartz textures are consistent. These veins are composed of fragments of older quartz showing undulose extinction and strain lamellae. The older quartz is separated by areas of finer grained polycrystalline quartz formed during dynamic recrystallisation (Fig. 2E). In the main-stage quartz veins Au is hosted in arsenopyrite grains as sieve texture (Fig. 2D) or in fine grained recrystallised quartz (Fig. 2F) both spatially associated with carbonate. The Qtz-4 veins were poor in visible Au which was observed only in one sample as an inclusion within pyrite.

Electron microprobe analysis (EMPA) was conducted on 18 thin sections at University of Oslo with Cameca SX100 with 5 spectrometers for in-situ trace element analyses on quartz. Elements analysed were Mg, K, Al, Ti and Fe. Hydrothermal quartz has a wide variation of trace elements which can be used as evidence for the chemical and physical conditions for formation of types of ore deposits (Rusk, 2012). Titanium-in-quartz method (TitaniQ) has been tested and can be used as a geothermometer for quartz according to previous studies (Wark & Watson, 2006; Rusk et al., 2008). Qtz-0 veins had an average Ti concentration of 110 ± 33 ppm with a range from 40 to 215 ppm. Concentrations of Ti were below the detection limit of 16 ppm in all other vein types. Aluminium concentrations are also systematically higher in Qtz-0 veins (average = 286 ± 220 ppm, range 28 to 814 ppm) compared to other vein types where analyses range up to 600 ppm but 36% of analyses are below the DL of 18 ppm.

4 Discussion

4.1 Early magmatic hydrothermal phase

The early-stage veins are clearly distinct in terms of form, mineralogy, and metal association compared to the other vein types. The trace element contents are also distinct with early-stage veins having higher Ti and Al contents than the other main-stage veins (Fig. 3). Applying the titanium-in-quartz (TitaniQ) geothermometer developed by Wark and Watson (2006), and assuming 1) the presence of rutile in the granodiorite, and 2) pressures of 4 ± 2 Kbar, yields temperatures of formation of 625 ± 75ºC. Previous work on Ti-in-quartz geothermometry reports higher Ti concentrations in higher temperature quartz, particularly that from magmatic hydrothermal systems (Wark & Watson, 2006; Rusk et al. 2008). We suggest that based on the trace element association, the vein orientation and distribution and the temperatures from Ti-in-quartz thermometry that early-stage veins represent an early magmatic-hydrothermal stage of veining and Au mineralisation.

4.2 Main-stage quartz veining at Barsele

Titanium concentrations in quartz of less than 10 ppm are suggested to indicate temperatures of <350ºC (Rusk et al. 2008; Rusk 2012). We suggest that the main-stage veins at Barsele show textures and compositions consistent with formation at less than 350ºC. The main-stage veins show distinct zones of recrystallisation of older quartz into finer-grained polycrystalline quartz with associated carbonate (calcite) and sulphides (arsenopyrite and pyrite). The visible Au in the main-stage veins at Barsele occurs within these zones of hydrothermal recrystallisation, either within the sulphides (Fig. 2D) or within the recrystallised fine-grained quartz (Fig. 2F). This indicates that the main-stage of Au mineralisation occurred either late relative to the emplacement of main-stage veins or post emplacement and most likely contains Au remobilised from early-stage mineralisation. The planar nature of the main-stage quartz veins most likely facilitated their recrystallisation during later deformation. In summary we observe 3 main mineralisation and veining events at Barsele; 1) early-stage magmatic hydrothermal quartz Au-Mo-Bi mineralisation that formed at 625 ± 75ºC, 2) the main-stage quartz veining that formed at <350ºC, and 3) the recrystallisation event that produced qtz-carbonate-sulphide-Au mineralisation that may represent the later stages of the main-stage veining or a separate hydrothermal event.

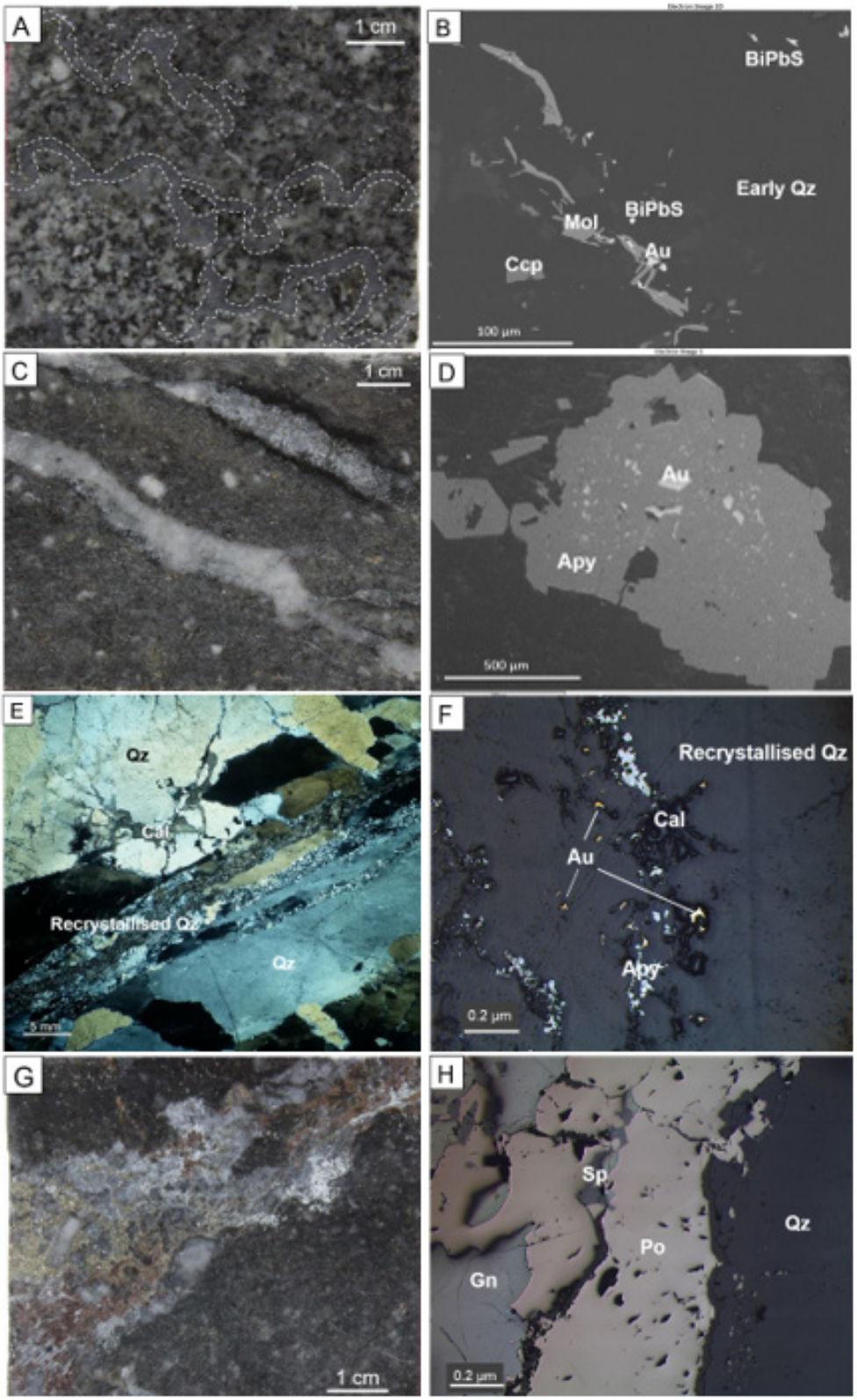

Figure 2. Quartz veins and textures A) Blue early-stage veins (Qtz-0) with irregular structure, in AVA022ER. B) Electron backscatter image of early-stage vein in sample AVA022ER, showing native gold beside molybdenite and an unknown BiPbS mineral in quartz. C) Main-stage veins (Qtz-1) without alteration rim and with alteration rim (Qtz-2) in SKI035ER D) Electron backscatter image of arsenopyrite with gold inclusions, in host rock, close to main-stage vein (Qtz-1). Sample CNT029ER E) Transmitted light image of SKI025ER with large quartz cut by recrystallised younger quartz with calcite. F) Reflected light image of main-stage vein (Qtz-3) in SKI013ER. Au associated with calcite, arsenopyrite and recrystallised quartz. G) CNT031ER with a Qtz-4 vein characterised by sulphides (Sp, Po, Gn, Py, Apy). H) Reflected light image of sulphide rich main-stage vein (Qtz-4) in CNT031ER.

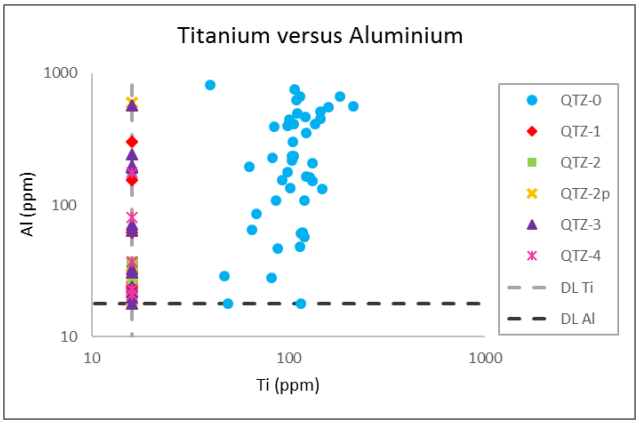

Figure 3. Plot of Ti vs Al concentrations in quartz from veins at Barsele from EMPA. The detection limit at 16 and 18 ppm for Ti and Al respectively. Qtz-0 veins are compositionally distinct from the others with higher Ti and Al.

Acknowledgements

We thank Agnico Eagle Sweden AB for access and discussions. We thank Tobias Bauer, Glenn Bark and Helen Thomas for discussions. Muriel Erambert at University of Oslo is thanked for assistance with EMPA.

References

Bark, G. & Weihed, P., 2007: Orogenic gold in the new Lycksele-Storuman ore province, northern Sweden; the Paleoproterozoic Fäboliden deposit. Ore Geology Reviews 32:431-451.

Bauer, T.E., Skyttä, P., Allen, R.L. & Weihed, P., 2011: Syn-extensional faulting controlling structural inversion – Insights from the Palaeoproterozoic Vargfors syncline, Skellefte mining district, Sweden. Precambrian Research 191:166-183.

Bauer, T.E., Skyttä, P., Hermansson, T., Allen, R.L., Weihed, P. 2014 Comparison of provenance, ore body shape and regional deformation patterns of VMS deposits for mapping the prospectivity in the Skellefte district, Sweden. Mineralium Deposita 19:555-573.

Bauer, T. E., Imaña, M., Höglund, K., Thomas, H. V., 2019: The structural setting of the Barsele Au Deposit. 15th Biennial SGA conference, 27-30 August 2019, Glasgow.

Eliasson, T., Greiling, R.O., Sträng, T. & Triumf, C.-A., 2001: Bedrock map 23H Stensele, scale 1:50 000. Sveriges geologiska undersökning Ai 126–129.

Kathol, B. & Weihed, P., 2005: Description of regional geological and geophysical maps of the Skellefte district and surrounding areas. Geological Survey of Sweden SGU, Ba 57.

Krispinsson, J., 2018: A GIS-based re-evaluation of the surface geology of the Storuman area, northern Sweden. BSc-thesis, Luleå University of Technology.

Lundström, I., Vaasjoki, M., Bergström, U., Antal, I. & Strandman, F., 1997: Radiometric age determinations of plutonic rocks in the Boliden area: the Hobergsliden granite and the Stavaträsk diorite. In: Lundqvist T (ed) Radiometric dating results 3, Sveriges geologiska undersökning C 830:20–30.

Passchier, C. W., Trouw, R. A. J., 2005: Microtectonics. Second edition. Springer.

Rusk, B., Lowers, H., Reed, M., 2008: Trace elements in hydrothermal quartz; relationships to cathodoluminescent textures and insights into hydrothermal processes. Geol 36:547–550

Rusk, B., 2012. Chapter 14: Cathodoluminescent textures and trace elements in hydrothermal quartz. In: J. Götze and R. Möckel (eds.), Quartz: Deposits, Mineralogy and Analytics, Springer Geology, DOI: 10.1007/978-3-642-22161-3_14.

Skyttä, P., Hermansson, T., Andersson, J. & Weihed, P., 2011: New zircon data supporting models of short-lived igneous activity at 1.89 Ga in the western Skellefte District, central Fennoscandian Shield. Solid Earth 2:205-217.

Thomas, H. V., Imaña, M., Höglund, K., Riegler, T. Mark, C., Ansberque, C. F., Bauer, T. E., Bark, G., 2019: Mineralization, alteration and age of the Barsele Au deposit, Sweden. 15th Biennial SGA conference, 27-30 August 2019, Glasgow.

Wark, D.A., Watson, E.B., 2006: The TitaniQ: a titanium-in-quartz geothermometer. Contrib Mineral Petrol 152:743–754

Weihed, P., Billström, K., Persson, P.-O. & Bergman Weihed, J., 2002: Relationship between 1. 90–1.85 Ga accretionary processes and 1. 82–1.80 Ga oblique subduction at the Karelian craton margin, Fennoscandian Shield. GFF 124:163-180

Polyphased gold mineralization at the Yaou deposit, French Guiana

Vincent Combes
Université de Lorraine-CNRS, laboratoire GeoRessources, Nancy, France / Auplata SA

Aurélien Eglinger, Anne-Sylvie André-Mayer, Yoram Teitler
Université de Lorraine-CNRS, laboratoire GeoRessources, Nancy, France

Christophe Scheffer, Arnauld Heuret
Université de Guyane, France

Pierre Gibert
Auplata SA

Didier Béziat
Géosciences Environnement Toulouse (GET), Université Paul Sabatier, France

Abstract. The Yaou deposit, located in French Guiana within the Guiana Shield, is hosted by the Paramaca Paleoproterozoic greenstone belt. The deposit displays multiple intrusive bodies aligned along a shear zone. The local deformation stages show a progressive evolution from the ductile regime to the brittle one. The $D_{1/2}$ event is responsible for the main penetrative foliation with associated ductile veining while the D_3 phase is related to a sinistral shearing. An intrusive event affects the district and is identified as being syn-D_3. The following phase D_4 represents a transitional to brittle veining set located preferentially within intrusive bodies and along the shear zone. A local D_5 brecciation event is offsetting the D_4 veins and is overprinted by late D_5 veinlets. A multi-stage model for the formation of the gold mineralization is presented focusing on gold-bearing pyrite. At the macroscopic scale, the gold mineralization is polyphased with the D_3 shearing and the D_4 brittle events being auriferous. A total of 6 generations of pyrite are defined. Results of in situ analyses using LA-ICP-MS on pyrite show that pyrite Py_3 exhibits an Au-As correlation with a cobalt and arsenic rhythmic zonation. Diagenetic pyrite Py_0 are a potential primary source of submicroscopic gold having a low contribution to the total budget. Pyrite Py_3 shows some gold content due to remobilization of Au_{D0}. Gold in pyrite Py_4 is found as submicroscopic gold, as micro-inclusions and as infilling fractures in association with other elements such as Te, Ag and Bi. Most contribution to the Au system is from micro-inclusions and relatively few from both free gold and submicroscopic. Pyrite Py_5 shows some late remobilization.

1 Introduction

Defining the monophase or polyphase character of an auriferous mineralized system in an orogenic gold deposit is a key factor for exploration targeting. Various gold deposits have been identified as having a polyphase release of gold with protracted history of precipitation, remobilization and new input, as evidenced by Meffre et al. (2016), Fougerouse et al. (2017), Le Mignot et al. (2017) and Augustin et al. (2018).

The Yaou deposit, owned by the gold exploration and mining company Auplata, is located in French Guiana, South America, within the Precambrian Guiana Shield. Ore bodies are currently identified along a 4.5 km long structure, giving an average tonnage and grade of 22.9 Mt at 2.1 g/t (data published on stock market, Auplata 2018).

The aims of this study are (i) to establish the link between deformation stages, quartz-carbonate vein generations, gold-bearing sulfide generations, alteration styles, gold types/behaviors/concentration and gold events, (ii) to understand the role of the different units including intrusions and mylonite, and (iii) to discuss about the polyphase character of the auriferous gold system.

2 Geological settings

The Amazonian Craton consists of the Guiana Shield to the north and the Guapore Shield to the south and constitutes one of the largest pieces of the Columbia 'puzzle' (Bispo-Santos et al., 2014 and references therein). The nature and the distribution of gold deposits within the Guiana Shield are intimately controlled by the Transmazonian geodynamic evolution occurred between ca. 2.25 Ga and 1.95 Ga (Enjolvy et al., 2008) and subdivided in two main periods, a period of crustal growth followed by a period of crustal recycling (Vanderhaerghe et al., 1998). The Yaou deposit is located within the southern branch of the Paramaca Greenstone Belt at the border with the Central TTG Complex (Delor et al., 2003). The deposit consists in a rheologically controlled mineralized system associated with quartz-carbonate veins located mainly in intrusive bodies aligned in a 4.5 km structure striking N60° along a shear zone. Gold is itself carried by pyrite with rare free gold. Mineralized veins are hosted by (i) fine grained dioritic intrusive rocks, composed of hydrothermal albite, ankerite, sericite and

pyrite, and (ii) a mylonitized metasedimentary unit composed of quartz, chlorite and sericite. The surrounding area is characterized by a metabasite unit. Studies carried out by Milési et al, 2003, define gold mineralization associated to quartz-albite veins, to disseminated sulfides along strata and to folded and unfolded veins hosted by Paramaca volcaniclastic rocks.

3 Results

The observed deformation stages show a progressive evolution from the ductile regime to the brittle one. Phases D_1 and D_2 are well marked in the host lithologies (metabasites). The veins associated with D_1 and D_2 are boudinaged and folded. Quartz grains within these veins display evidences of recrystallization with Grain Boundary Migration (GBM). The D_3 deformation stage is characterized by transcurrent shearing (NE-trending sinistral shear zone) and intrusions of intermediate magmas. A C/S_3 fabric is observed together with a mylonitic gradient and millimeter scale hydrothermal pyrite with quartz-chlorite-calcite fringes. The D_4 brittle deformation stage is characterized by quartz veins mostly hosted by dioritic intrusions, and more rarely cross-cutting the sheared metasediments and metabasites. A late brecciation stage D_5 affects the intrusive unit and the metabasite. The combination of drillcores observation, petrographic data and trace elements analysis allows to discriminate generations of vein and associated pyrite linked to deformation stages. Py_0 pyrite is interpreted as diagenetic core within Py_3 pyrite, the latter being associated with D_3 deformation. Py_4 pyrite occurs within D_4 veins as well as in their alteration haloes. Py_5 pyrite is developped within the D_5 breccia cement. When comparing deformation stages, vein stages and alteration phases (including pyrite) data with auriferous zones along drill cores obtained from whole-rock gold analyses, it is clear that D_4 veins and associated Py_4 are responsible for high gold grade (average values of 1 to 4 g/t), although $Py_{0/3}$ pyrites associated with D_3 shearing may significantly contributes to the gold budget (up to 1.5 g/t). The D_2 event is not auriferous (below 0.1 g/t). D_5 brecciation (less than 0.5 g/t when no D_4 vein associated) hardly contributes to the whole mineralization. Gold releases are therefore associated with the D_4 veining event and, to a lesser extent, with the D_3 shearing event. The combined occurrence of $Py_{0/3}$ and Py_4 results in the highest gold grades zones (e.g. in the F_{75} drill core with meters intervals grading > 9 g/t). Ore shoots are mostly located in intrusive bodies and in the mylonite because of the high frequency of the D_4 veins. Importantly, rare D_4 in the metabasite return positive Au grades (about 0.5 g/t) but are not frequent enough to build an ore zone.

LA-ICP-MS analyses of trace elements within pyrite show that highest submicroscopic gold values are found in pyrite Py_0 with a median of 1.1 ppm with outliers above 50 ppm. These outliers correspond to analyses conducted within As-rich zones of Py_0 pyrites. Pyrite Py_0 exhibits variably high arsenic content, above 200 ppm with a median value of 2800 ppm. Gold concentrations of analyzed pyrite Py_2 are below the detection limits confirming that the formation of these pyrite was not related to any gold mineralizing event. This generation is characterized by elevated Ni concentrations (mean value of 8000 ppm). Py_3 pyrites are arsenian pyrite with As content ranging from 25 ppm to 3000 ppm, high variations corresponding to As-rich rims and As-depleted rims. A positive correlation between Au and As signals is observed. The median Au content in Py_3 pyrites, corresponding to invisible gold, is about 0.2 ppm. Cobalt displays variable concentrations ranging from 40 to 4800 ppm. The gold content in pyrite Py_4 ranges from 0.3 to 7.5 ppm, with a median value of 0.75 ppm. Such a large variability in the gold content related to the presence of gold nano- to micro-inclusions within pyrite. Pyrite Py_4 displays lower As and Co and higher Te and Bi contents compared to other pyrite generations. Gold micro-inclusions larger than 30 µm, associated with Py_4, were also analyzed using LA-ICP-MS. These micro-inclusions are associated with Te, Ag, Bi, Pb (plus minor As, Ni and Co). The lattice is depleted in Au near gold micro-inclusions. Pyrite Py_5 has trace elements composition relatively similar to that of the Py_4 generation but with lower gold contents (median value of 0.4 ppm) and higher Ni content (median value of 190 ppm). Trace element analysis of pyrites shows that Py_0, Py_3, Py_4 and Py_5 are gold-bearing. Positive correlation for Au-Ag-Te-Bi in pyrite associated to D_4 and positive correlation for Au-As in pyrite associated to D_0 and D_3 are evidenced. Pyrite exhibits a remarkable Te enrichment from generation Py_2 to Py_5, together with the decrease of the As content when building the deposit.

4 Discussion

4.1 Function and contribution of each event to the model: a polyphased mineralization at the macroscopic scale

Each event documented in the present study has a specific role on the formation of the deposit. The relative amount of gold attributed to each event is shown in figure 1. First at D_0, a stratabound diagenetic pyritization, located in a metasediment, is evidenced as being a primary source of gold.

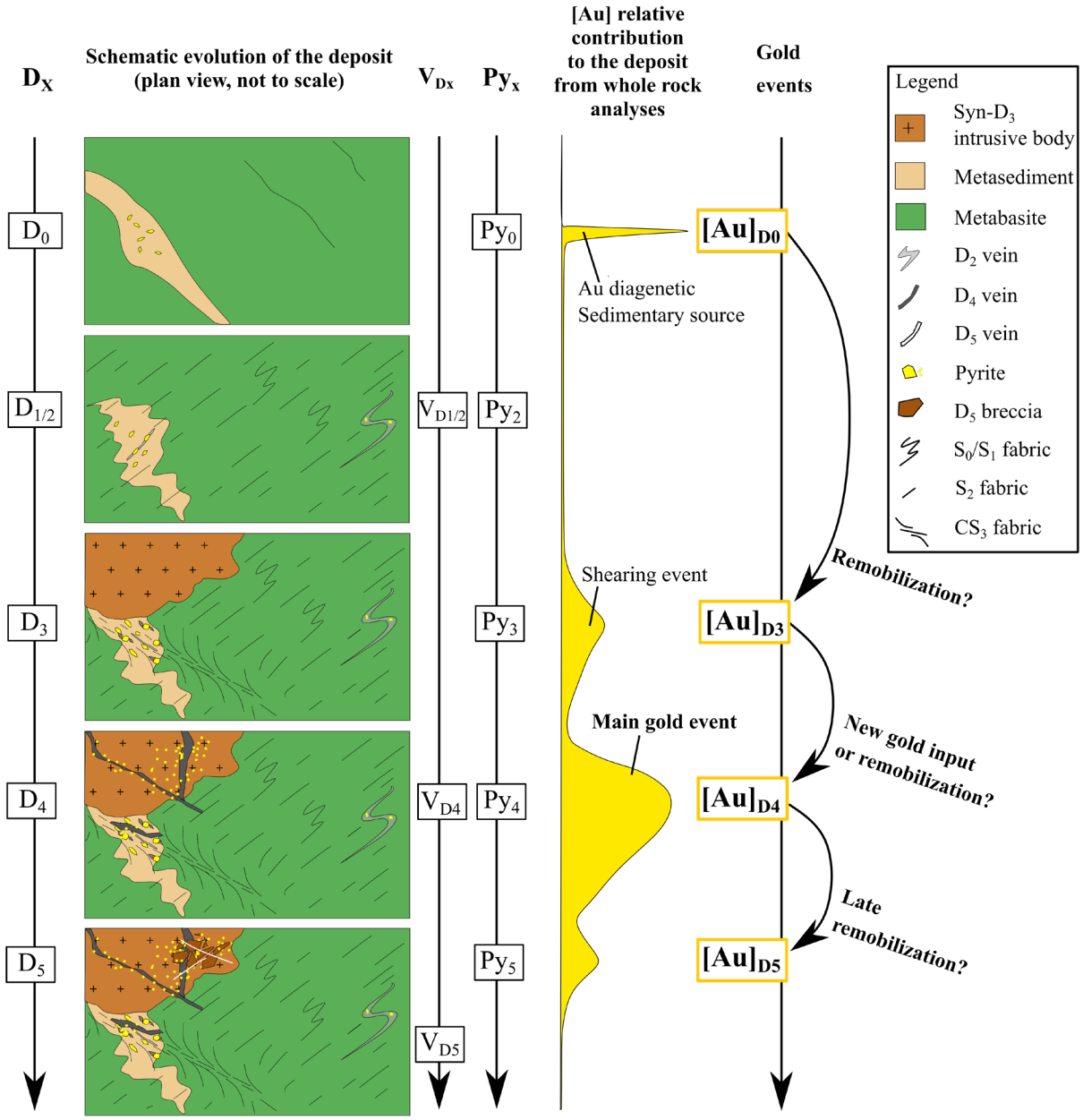

Figure 1. Polyphased model for the formation of the deposit with interpreted contribution of each events. The main gold phase is related to the D_4 deformation stage.

A relatively weak contribution to the system is defined as the hosting unit is poorly developed in the area and pyrite Py_0 are not statistically abundant from core observation. The D_0 can be defined as an early gold phase but gold in Py_0 is not high enough to support a single source of gold. The ductile $D_{1/2}$ compression phase, giving the main penetrative foliation, shows no evidence of any contribution to the deposit formation. The importance of the D_3 shearing event in the gold mineralization is multiple. The intrusive bodies are spatially associated with the shear zone, having the same N60° trend with a less than 200 m spacing between the aligned intrusion/ dykes and the shear corridor. Secondly, the D_3 shearing provides hydrothermal fluids to the system: the mineralization D_3 is controlled by the localized shearing, acting as a pathway for the circulation of fluids forming the Py_3 rims around pyrite Py_0. Locally the sheared metasediment host D_4 veins along the N60°E trend. The contribution of D_3 to the deposit formation is major whereas the contribution of Au_{D3} to the budget from Py_3 is relatively weak as pyrite Py_3 is only present within the 30 m large D_3 band.

The role of the intrusion highlights the rheologically controlled aspect of the deposit, as auriferous D_4 veins are preferentially located within the intrusion. Due to rheological contrasts, veins are more likely to develop in the intrusions which are a favorable environment for fracturation, forming traps for auriferous fluids. The intrusive event may be associated with new gold input to the system, although the observation that rare D_4 veins

within others lithologies are auriferous, argue against such interpretation

In contrast, the epigenetic D_4 event represents the main gold mineralization stage with a high frequency of both D_4 veins and associated pyrite Py_4 together with strong ankeritization. It is most likely associated with a new gold input, related to new hydrothermal fluids (ankerite rich) together with some remobilization of previous gold releases.

The D_5 event is related to a late remobilization, within breccia due to both hydrothermal fluids and brittle deformation. The relative contribution to the system is weak, Py_5 are auriferous but when no D_4 brecciation is observed, gold assays are low (below 0.5 g/t).

A polyphased deposition of gold is therefore evidenced with at least 4 events. This is critical for exploration as gold can be located in various settings (Py_0 in metasediments, D_3 shear zone, D_4 veins in intrusions and D_5 breccia) by multiple remobilization and possible new gold inputs. The ore shoot locations are lithology controlled for Au_{D0} (metasediments), structurally controlled (shearing N60°) for Au_{D3} and rheology/lithology controlled for the Au_{D4}.

4.2 Gold evolution, behaviors and speciation at the microscopic scale

The early gold Au_{D0} in diagenetic pyrite Py_0 is present both as nano-inclusions and as solid solution in the lattice of the sulfide, as evidenced by LA-ICP-MS spectra patterns. Invisible gold is the only gold species in the initial sulfidation stage, closely associated to arsenic. Au_{D3} is also classified as invisible. Three gold species associated to the main event D_4 are defined, namely, (1) anhedral micro-inclusions in Py_4, (2) gold infilling deformation cracks in Py_4 and (3) free gold grain situated in the D_4 vein at the edge of Py_4. The visible gold could be secondary, coming from remobilization of primary, invisible gold.

We identify two main positive correlation: invisible gold is linked to arsenic and visible gold is linked to silver, tellurium and bismuth. The contribution of invisible gold is relatively low (below 1 ppm in pyrite lattice). Most of the gold is identified as micro-inclusion and infilling fractured gold. We define an early low-grade enrichment (Au_{D0} to Au_{D3}) followed by a later high-grade episode (Au_{D4}).

5 Conclusions

Our data demonstrate that the gold mineralization is polyphased with a total of 4 auriferous events. Most of the mineralization is associated with one set of hydrothermal veins, (brittle D_4 event). Gold micro-inclusions within Py_4 pyrites predominantly contribute to the Au system, together with minor contribution from both free and submicroscopic gold. The ore shoot locations are lithology controlled for Au_{D0} (metasediments), structurally controlled (shearing N60°) for Au_{D3} and rheology/lithology controlled for the Au_{D4}.

Acknowledgements

This study is part of Vincent Combes's Ph.D. research at the Université de Lorraine at GeoRessources, Nancy, France. This research was funded by Auplata SA and benefited of the framework of the CREGU. This study greatly benefited from discussions and friendly support from Frédéric Tona. We are grateful to the GET Laboratory in Toulouse, France, for LA-ICP-MS analyses.

References

Augustin J, Gaboury D (2018) Multi-stage and multi-sourced fluid and gold in the formation of orogenic gold deposits in the world-class Mana district of Burkina Faso - Revealed by LA-ICP-MS analysis of pyrites and arsenopyrites. Ore Geol Rev 104:495-521

Bispo-Santos F, D'Agrella-Filho MS, Janikian L, Reis NJ, Trindade, RIF, Reis, MAAA (2014) Towards Columbia: Paleomagnetism of 1980–1960 Ma Surumu volcanic rocks, Northern Amazonian Craton. Precambrian Res 244:123–138

Delor C, Lahondère D, Egal E, Lafon, Cocherie A, Guerrot C, Rossi P, Truffet C, Theveniaut H, Phillips P, Avelar VG (2003a) Transamazonian crustal growth and reworking as revealed by the 1:500000 scale geological map of French Guiana. Géol de la France 2-3-4:5–57

Enjolvy R, (2008) Processus d'accrétion crustale et régimes thermiques dans le bouclier des Guyanes : signatures géochimiques et thermochronologiques au transamazonien (2250-1950 Ma) : Phd thesis, Université Montpellier II-Sciences et Techniques du Languedoc 305 p

Fougerouse D, Micklethwaite S, Ulrich S, Miller J, Godel B, Adams D, McCuaig TC, (2017) Evidence for two stages of mineralization in West Africa's largest gold deposit: Obuasi, Ghana. Econ Geol 112:3–22

Gibbs AK, Barron CN (1993) The Geology of the Guiana Shield: Oxford Monographs on Geology and Geophysics 22: 246 p

Le Mignot E, Reisberg L, André-Mayer A-S, Bourassa Y, Miller J, (2017) Re-Os geochronological evidence for multiple Paleoproterozoic gold events at the scale of the West African craton. Eco Geol 112:145–168

Meffre S, Large RR, Steadman JA, Gregory DD, Stepanov AS, Kamenetsky VS, Ehrig K, Scott RJ (2016) Multi-stage enrichment processes for large gold-bearing ore deposits. Ore Geol Rev 76:268–279

Milési J, Lerouge C, Delór C, Ledru P, Billa M, Cocherie A, Egal E, Fouillac A, Lahondère D, Lasserre J, Marot A, Martel-Jantin B, Rossi P, Tegyey M, Théveniault H, Thiéblemont D, Vanderhaeghe O (2003) Gold deposits (gold-bearing tourmalinites, gold-bearing conglomerates, and mesothermal lodes), markers of the geological evolution of French Guiana: geology, metallogeny, and stableisotope constraints. Géologie de la Fr. 2-3-4:257-290

Vanderhaeghe O, Ledru P, Thiéblemont D, Egal E, Cocherie A, Tegyey M, Milési JP (1998) Contrasting mechanism of crustal growth: Geodynamic evolution of the Paleoproterozoic granite–greenstone belts of French Guiana Precambrian Res 92:165–193

Geochemical signature of native gold from various Au-bearing deposits – implications for mineral exploration

Haiming Liu, Georges Beaudoin, Sheida Makvandi
E4m - Centre de recherche sur la géologie et l'ingénierie des ressources minérales, Département de géologie et de génie géologique, Université Laval, Canada

Simon Jackson
Geological Survey of Canada, Ottawa, Canada

Abstract. Native gold is a significant indicator mineral for gold-bearing deposits. The chemical composition of gold in diverse geological settings is a function of the composition of its parental hydrothermal fluids in diverse geological settings. Thus, trace elements contained in native gold could present a particular geochemical signature that can be used to discriminate gold from different mineralization types. This study characterizes the composition of native gold grains from various Au-bearing deposit types and yields discrimination models for application to mineral exploration for gold deposits. Trace element contents of gold from orogenic, epithermal and volcanogenic massive sulfide (VMS) deposits, were measured in-situ by laser ablation ICP-MS (LA-ICP-MS) to identify systematic changes in gold compositions associated with different mineralization environments, and, where possible, to identify the distinctive geochemical signature of Au in each hydrothermal system. The results suggest that Zn, Ni, Sb, Pd, and Te are the most significant discriminator elements to differentiate gold among different gold deposit types.

1 Introduction

Native gold occurs in a great variety of deposit types and its chemical composition is controlled by factors including transport media, fluid chemistry and precipitation processes (Chapman et al. 2009). Thus, the geochemical composition of native gold can fingerprint various Au-bearing deposit types (Chapman et al. 2017). Recent studies have focused on measuring major element concentrations in placer gold grains, which are used as indicators to identify the source of detrital gold in overburden areas (Chapman and Mortensen 2016). Combining morphological information and alloy composition, based on the relative proportions of Au, Ag, Pd and Hg, allowed identification of six genetic alloy types for placer gold in highly oxidizing hydrothermal environments (Chapman et al. 2009). Based on Au, Ag, and Cu components, ternary diagrams were used to distinguish gold from porphyry Cu, porphyry Cu-Au, and epithermal deposits (Townley et al. 2003). However, due to the limited numbers of elements determined, these diagrams were inconclusive for differentiating gold from epithermal deposits and that from orogenic gold deposits (Moles et al. 2013).

The development of the sensitive technique of laser ablation inductively coupled plasma-mass spectrometry (LA-ICP-MS) has allowed for accurate in-situ measurement of trace element concentrations in mineral matrices, which offers deeper insights into ore-forming processes and mineralization events (Cook et al. 2017; Reich et al. 2017). LA-ICP-MS has been used to provide quantitative analyses of trace element concentrations within placer gold. However, in-situ major and trace element analysis of native gold from various Au-bearing deposit types is not well documented and there is a lack of a powerful discriminant model to differentiate gold from different systems. This study characterizes the chemical compositions of gold grains from various geologic settings using LA-ICP-MS in order to build discriminant models that can distinguish different origins of native gold grains.

2 Methodology

A total of 628 gold grains were selected from forty-two Au-bearing deposits or districts worldwide (Figure 1), including orogenic deposits (*e.g.*, Lucien Béliveau/New Béliveau, Sigma, Goldex from Canada, Kittilä from Finland, Sukhoi Log from Russia, St. Ives district, Fosterville from Australia, and Shangxu from China, Cuiabá from Brazil), epithermal deposits (*e.g.*, Little Florence, Ken Snyder, and Golden Arrow from USA, Fruta Del Norte from Ecuador, La India from Mexico), and volcanogenic massive sulfide deposits (VMS) (*e.g.*, Boliden from Sweden, Ming, LaRonde and Quemont from Canada). The samples come from different geological settings, have a wide variety of mineralization ages and are hosted by different rocks. The purpose of the broad scope of samples is to capture the variance that may arise from different gold precipitation conditions, resulting from different hydrothermal fluids forming gold deposits. The deposits selected for this study are typical gold deposits that have been documented by previous researchers thus providing required background information. Petrographic analysis and sample descriptions were conducted using optical microscopy and scanning electron microscopy (SEM).

Gold grains were analyzed for major and minor elements at Université Laval (Canada) using a CAMECA SX-100 electron probe micro-analyzer (EPMA), equipped with five wavelength dispersive spectrometers, both using a 5 µm diameter beam with a voltage of 25KV and a current of 100nA. Trace elements contents in gold were measured using a Photon Machines Analyte 193nm

Excimer laser ablation system coupled to an Agilent Technologies 7700x series quadrupole ICP-MS at the Geological Survey of Canada (Ottawa, Canada) and a Resonetics S-155-LR 193nm Excimer laser ablation system coupled to an Agilent 7700x quadrupole ICP-MS at the University of New Brunswick (Fredericton, Canada). Native gold grains were ablated in spot mode at 10Hz repetition rate, an energy density of 4.2J/cm^2 and a 25 to 45μm spot size depending on the gold size. Data acquisition included 40s for ablation and 20s for background measurement. Trace element concentrations were internally normalized to Ag values determined by EPMA. At GSC, the external standards, GSE-1G, Po726, and the synthetic gold standards (NA-AU-31, NA-AU-30 and AU-RM-2) were used for data calibration and quality control of LA-ICP-MS analyses. At UNB, the external standards, NIST610, MASS1, and the synthetic gold standard (NA-Au-31) were used for data calibration. Following Makvandi et al. (2016) and Barker and Rayens (2003), the imputed centered log-ratio (clr) transformed chemical data of gold, for the elements with less than 40% censored data were investigated by partial least squares-discriminant analysis (PLS-DA).

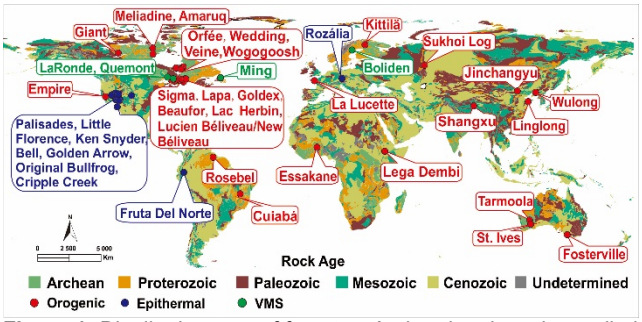

Figure 1. Distribution map of forty-two Au-bearing deposits studied including orogenic, epithermal and volcanogenic massive sulfide (VMS) deposits.

3 Results and discussion

Gold from orogenic gold deposits dominantly occurs as anhedral to subhedral inclusions in pyrite, arsenopyrite, chalcopyrite, and pyrrhotite. Gold also fills in the interstitial space between quartz, tourmaline and calcite grains (Figure 2A). Gold from epithermal deposits is characterized by the mineral assemblage pyrite ± sphalerite ± chalcopyrite ± galena. In some epithermal deposits, gold occurs as electrum with Au rich rims (Figure 2C). Gold can also occur as disseminated grains in equilibrium with bismuthinite in quartz veins (Figures 2B, C, D). Gold from VMS deposits commonly occurs either in veinlets filling fractures, or coarse grains in equilibrium with arsenopyrite, chalcopyrite, pyrite, tellurides, tourmaline, pyrrhotite, bornite, and minor with tennantite-tetrahedrite (Figures 2D, E). In this study, gold grains with a homogeneous distribution of Au and Ag in backscattered-electron images (BSE) and EPMA maps were selected to determine their trace element compositions by LA-ICP-MS (Figures 2D, F, E).

As is shown in Figure 3, gold grains from different deposit types have distinct trace element compositions. For instance, gold from epithermal deposits is characterized by relatively high Te, Se, As, Pb, Zn, and Fe contents, but low Cd, and Cu contents. In contrast, gold from orogenic gold deposits contains relatively high Sb, and Cu concentrations, whereas Cr, Ni, and Fe concentrations are low. Gold from VMS deposits can be distinguished by relatively high Cu and S, but low Zn, Te, Se, Sb, Sn, Pb, and Fe concentrations. Generally, gold from epithermal deposits shows greater variations in Te, Se, Bi, As, Pb, and Zn relative to gold from orogenic gold deposits. However, gold from VMS deposits is characterized by larger variations in Pd, Bi, Sb, Pb, and Cu than those in gold from orogenic gold deposits. Overall, significant variation of amounts for Te, Bi, Sb, As, Pb, and Cu compositions of gold grains is discriminant for VMS, epithermal and orogenic gold deposits. This indicates the potential of trace elements signatures of gold grains in provenance discrimination of gold grains from unknown sources. The variation in chemical compositions of gold from various geological systems may be explained by different chemical compositions and physicochemical conditions of parent fluids and deposit mechanisms.

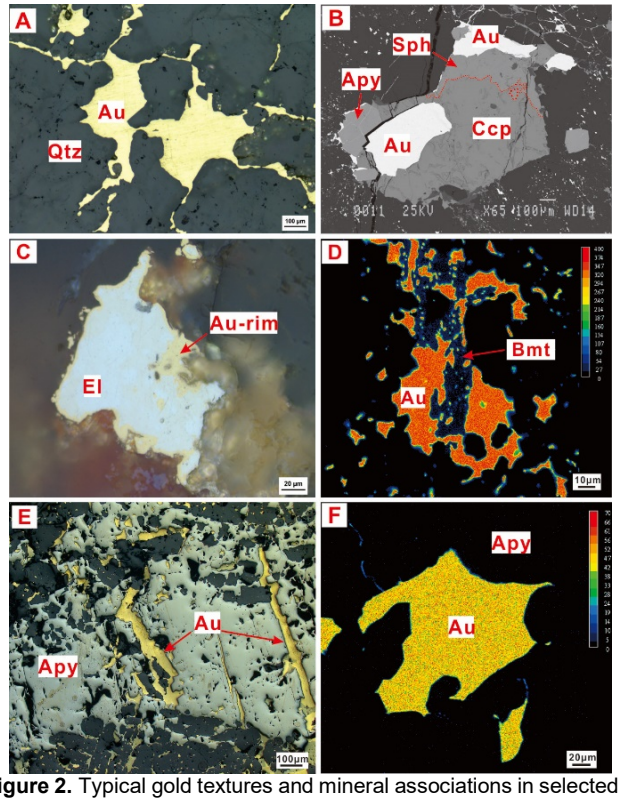

Figure 2. Typical gold textures and mineral associations in selected Au-bearing deposits. (A) Irregular gold veinlets in fractures between quartz grains from Amaruq deposit, Canada, (B) BSE image shows gold inclusion in chalcopyrite and contacts with sphalerite and arsenopyrite from LaRonde, Canada, (C) Gold occurs as electrum with Au-rich rims from Golden Arrow, USA, (D) EPMA mapping shows anhedral gold associated with bismuthinite from Little Florence, USA, (E) Gold occurs as veins cutting arsenopyrite associated with chalcopyrite from Quemont, Canada, (F) EPMA mapping shows homogeneous gold in contact with arsenopyrite from Quemont, Canada. Au-gold, Apy-arsenopyrite, Bmt-bismuthinite, El-electrum, Qtz-quartz, Ccp-chalcopyrite, Sph-sphalerite.

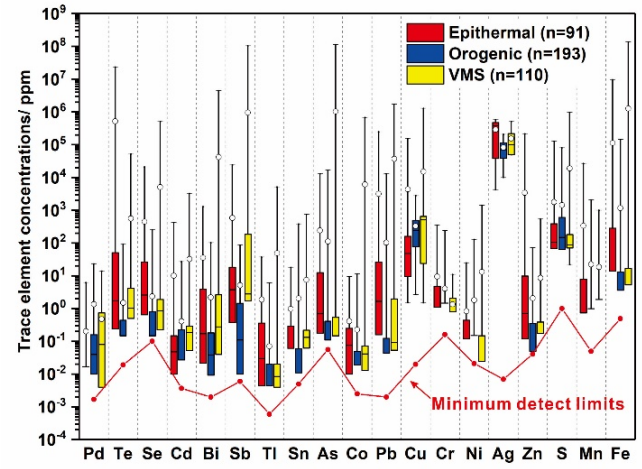

Figure 3. Multi-element box and whisker plots of trace element composition based on LA-ICP-MS data from epithermal, orogenic and VMS deposits. The red line indicates the minimum detection limits for LA-ICP-MS analysis.

PLS-DA is a supervised classification technique that allows discrimination of trace element compositions in gold from the three studied deposit types. The loadings biplot of first and second PLS-DA components (qw*1-qw*2) illustrates correlations among elemental contents and relationships among elements and deposit types. Cadmium, Sn, Bi, and Sb plotted in the positive first principal component (PC1) and positive second principal component (PC2) quadrant, and show a positive correlation. They have negative correlations with Ni, S, Cr, Co, Fe, As, and Zn, which have negative PC1 and negative PC2 scores (Figure 4A). Copper and Pd, plot in negative PC1 and positive PC2 quadrant, are negatively correlated with Pb and Te, which plot in the positive PC1 and negative PC2 quadrant.

Correlations among trace elements define the classification of gold analyses in a PLS-DA first and second scores scatter plot (t1-t2; Figure 4B). Gold from orogenic deposits forms a cluster with negative t1 values because of variably higher S, Ni, Cr, Cu, Fe, As, Zn, Co, As and Pd, and lower Sn, Sb, Te, Pb, and Bi relative to the average of the dataset (Figures 4A-B). Gold from VMS deposits mainly plots in the positive t1 and positive t2 quadrant due to covariation of Cd, Bi, Sb, and Sn (Figures 4A-B). Gold from epithermal deposits can be distinguished from the other two deposit types by positive t1 and negative t2 due to higher Fe, Zn, As, Sb, Te, Pb, and Bi, and lower S, Ni, Cu, Pd and Cd. Furthermore, elements such as Zn, Ni, Sb, Pd, and Te in gold, which plot at the periphery of the loadings biplot (Figure 4A), play a more significant role in distinguishing orogenic, epithermal and VMS deposits based on the gold composition in Figure 4B.

Gold samples plotting in the vicinity of each other in the t1-t2 subspace are characterized by similar trace element compositions. Gold grains carry the chemical characteristics of their parental fluids that are derived from their geologic settings. Thus, the variation in the chemical compositions of gold probably can reflect the differences in the chemistry of ore-forming fluids and geological settings where gold was precipitated. The Hg, Bi, Sb, and Te enrichments in gold from VMS and epithermal deposits are consistent with the composition of fluids related to volcanic systems. The enrichment of S, Ni, Cu, Pd and Zn in gold from orogenic deposits may be related to S-bearing auriferous fluids associated with orogenic belts.

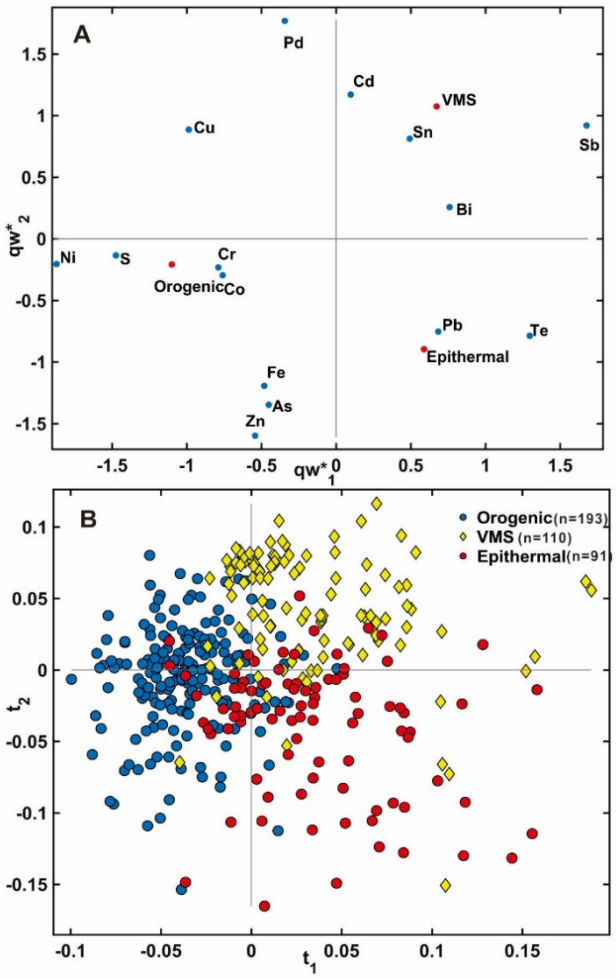

Figure 4. PLS-DA of native gold LA-ICP-MS data classified by the studied deposit types. In this model. (A) The first and second loading plot (qw*1-qw*2) indicates correlations among elemental variables and deposit types. (B) The score plot (t1-t2) shows the distribution of gold samples projected for the first and second components.

To investigate the potential of PLS-DA model in the classification of gold deposit types, the LA-ICP-MS data of native gold from the Hollinger, McIntyre and Aunor orogenic gold deposits (Velasquez 2014) are projected into the t1-t2 subspace. Because S, Cd, Co data were lacking in the literature data, they were excluded in the dataset and a new PLS-DA diagram had to be defined to project the literature data (Figure 5). As illustrated in Figure 5B, the majority of the literature analyses of gold from orogenic gold deposits from literature were projected into the field defined by gold from orogenic deposits from this study. Thus, PLS-DA of gold LA-ICP-MS data yields robust discrimination models for classification of native gold from orogenic, epithermal, and VMS deposits.

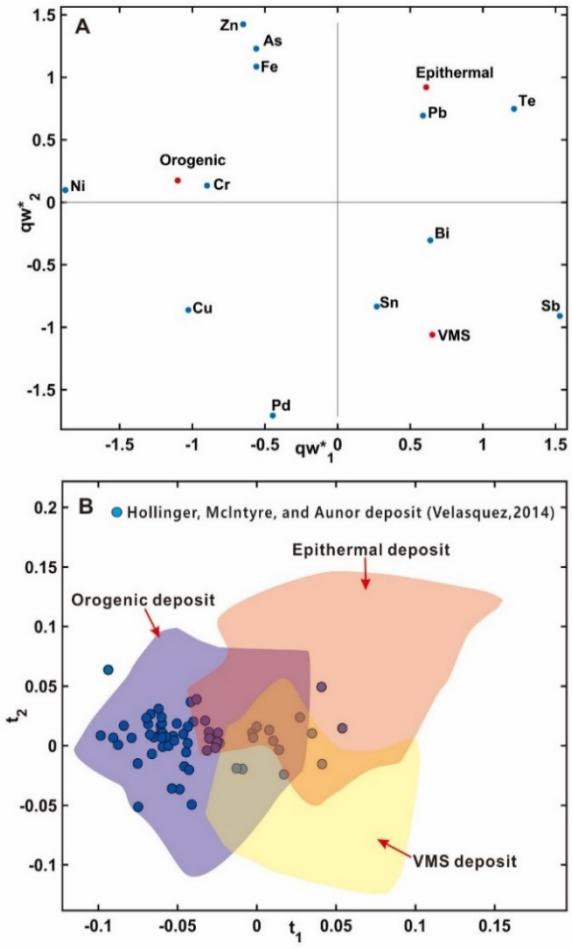

Figure 5. PLS-DA of native gold compared with literature data from Hollinger, McIntyre and Aunor orogenic gold deposits (Velasquez 2014). (A) The loadings plot (qw*1-qw*2) for the first and second components indicates correlations among elemental variables and deposit types. (B) Projection of the compositional data of literature data into the defined discriminant model from this study. The three shade areas were drawn from the first and second components score plots.

4 Conclusion

The differences in composition between the chemical signatures of gold from different deposit types identified by EPMA and LA-ICP-MS are significant. The use of PLS-DA demonstrates the potential for trace elements in gold to be used as discriminators and the ability to build discriminant models to differentiate gold from orogenic, epithermal and VMS deposits. Our PLS-DA results suggest that gold from orogenic gold deposits is characterized by high Ni, S, Cu, and low Sb and Te compared to those from gold in VMS and epithermal gold deposits. Gold derived from VMS Au-rich deposits typically contains higher Pd, Cd, and Sn, and lower Zn, As, Fe, and Ti contents relative to that from the other two deposit types studied. In contrast, gold from epithermal deposits is characterized by high Te, Pb, Zn, Ti, and low Pd, Cu, and Ni. The most effective discriminator elements to classify gold from the three deposit types are Zn, Ni, Sb, Pd, and Te. Discriminant models defined by PLS-DA of trace elements in gold can be used to distinguish gold from orogenic, epithermal and VMS deposit types, which can be a useful tool to determine deposit types for mineral exploration.

Acknowledgements

Many thanks to NSERC and Agnico Eagle Mines Litmited for funding the research. We thank Marc Choquette (Laval U.) and Brandon Boucher (UNB) for their assistance with EPMA and LA-ICP-MS analyses, respectively. Many thanks to Émilie Bédard (E4M) for improvements on this manuscript. Special thanks to Veronica Di Cecco (Royal Ontario Museum, Canada), Larry Pilgrim (Rambler Metals and Mining Canada Ltd), Pia Fagerström (Field Exploration Northern Fennoscandia, Boliden), Peter W. Stewart (The Valley Geological Services Inc.), David Pitre (Agnico Eagle Mines Ltd), Michael W. Ressel (University of Nevada), Stefano Salvi (Géosciences Environnement Toulouse – OMP, France) for providing samples for analyses.

References

Barker, M., Rayens, W. (2003) Partial least squares for discrimination. Journal of chemometrics 17:166-173.

Chapman, R., Leake, R., Bond, D., Stedra, V., Fairgrieve, B. (2009) Chemical and mineralogical signatures of gold formed in oxidizing chloride hydrothermal systems and their significance within populations of placer gold grains collected during reconnaissance. Economic Geology 104:563-585.

Chapman, R., Mortensen, J. (2016) Characterization of gold mineralization in the northern Cariboo Gold District, British Columbia, Canada, through integration of compositional studies of lode and detrital gold with historical placer production: a template for evaluation of orogenic gold districts. Economic Geology.

Chapman, R., Allan, M., Mortensen, J., Wrighton, T., Grimshaw, M. (2017) A new indicator mineral methodology based on a generic Bi-Pb-Te-S mineral inclusion signature in detrital gold from porphyry and low/intermediate sulfidation epithermal environments in Yukon Territory, Canada. Mineralium Deposita, 1-20.

Cook, N.J., Ciobanu, C.L., Ehrig, K., Slattery, A., Verdugo-Ihl, M.R., Courtney-Davies, L., Gao, W. (2017) Advances and Opportunities in Ore Mineralogy. Minerals 7:233.

Makvandi, S., Ghasemzadeh-Barvarz, M., Beaudoin, G., Grunsky, E.C., McClenaghan, M.B., Duchesne, C., Boutroy, E. (2016) Partial least squares-discriminant analysis of trace element compositions of magnetite from various VMS deposit subtypes: Application to mineral exploration. Ore Geology Reviews 78:388-408.

Moles, N., Chapman, R., Warner, R. (2013) The significance of copper concentrations in natural gold alloy for reconnaissance exploration and understanding gold-depositing hydrothermal systems. Geochemistry: Exploration, Environment, Analysis 13:115-130.

Reich, M., Large, R., Deditius, A.P. (2017) New advances in trace element geochemistry of ore minerals and accessory phases. Ore Geology Reviews 81:1215-1217.

Townley, B.K., Hérail, G., Maksaev, V., Palacios, C., de Parseval, P., Sepulveda, F., Orellana, R., Rivas, P., Ulloa, C. (2003) Gold grain morphology and composition as an exploration tool: application to gold exploration in covered areas. Geochemistry: Exploration, Environment, Analysis 3:29-38.

Trace element signature of pyrite from Bagassi gold deposit, western Burkina Faso

Hilaire S. Dakouré, Aurélien Eglinger, Anne-Sylvie André-Mayer
GeoRessources, Université de Lorraine-CNRS-CREGU, France

Naba Seta, Wilfried A.B. Toé
Laboratoire Géosciences et Environnement Minier, Université Ouaga1 Pr Joseph Ki-Zerbo, Burkina Faso

Luc Siebenaller
Université de Toulouse, CNRS, Géosciences Environnement Toulouse, France

Abstract. The Bagassi gold deposit is situated on the Houndé greenstone belt. It is a high-grade (1.8 million tons @ 11.47 g/t) deposit in which mineralization is located at the contact between volcanic mafic rocks and granitoids. Two types of mineralization were observed. (i) gold disseminated within sulfides within host-rock and ankerite-rich veinlets and (ii) as free particles within quartz-rich tension gashes. Two types of pyrite associated to gold events were identified. Py_1 is generally overgrown by Py_2 which contain native gold inclusions. LA-ICP-MS data reveal that Py_1 is enriched in trace elements (Median Au = ~4 ppm, median As = ~9000 ppm) compared to Py_2 which have median Au= 0.01 ppm and median As= ~320 ppm ppm. Py_1 and Py_2 show approximately the same range for Ni, Co, Zn, Te and Se and are both depleted in Cu, Sb, Ag, Bi and Pb (Median < 2 ppm). At 55 Zone gold mineralization refers to a single hydrothermal event associated to remobilized gold (gold fineness > 906). Earlier stage of this event consist of an As-Au rich fluid with incorporation of primary gold into As-rich Py_1 lattice. The later stage implicates an Au-oversaturated fluids forming free gold nuggets in the quartz-rich veins related to second generation Py_2.

1 Introduction

Orogenic gold deposits represent a major source for global gold production (Goldfarb et al., 2001). In these deposits, gold is generally associated to pyrite. Because of its abundance and its role in gold mineralization, textural, chemical and physical properties of pyrite have been extensively studied. (Large et al. 2007, 2009; Thomas et al. 2011 ; Deditius et al.2014 ; Velasquez et al. 2014, 2018 ; Augustin et al. 2019).

In-situ analyzes allow to discuss gold remobilization processes and to interpret hydrothermal evolution of pyrite (Thomas et al. 2011, Velasquez et al. 2014, Fougerouse et al. 2017, Augustin et al. 2018).

This work investigates the distribution of trace elements in pyrite grains related to the different gold event of the Bagassi Gold deposit.

2 Geological setting

2.1 Regional setting

The southern part of West African Craton, the Man-Leo shied consists of an Archean domain (Kénéma-Man domain) to the west and a Paleoproterozoic domain (Baoulé-Mossi domain) to the east separated by the Sassandra fault (Feybesse and Milesi 1994; Kouamelan et al. 1997) (Fig.1a). Geological formations of the Baoulé-Mossi domain also called Birimian formations were affected by a polyphase Eburnean orogeny between ~2150 Ma and 1980 Ma (Baratoux et al. 2011).

In western Burkina Faso, three deformation events have been defined by Baratoux et al. 2011. The first phase D1 (~2160 – 2120Ma) has been distinguished as a penetrative metamorphic foliation S1. This phase corresponds to a shortening and is associated with the emplacement of TTG and granitoids ME1. A second phase D2 (2110-2109 Ma) is characterized by transcurrent shear zones that overprint the structural grain of this area. The late-Eburnean D3 or post-Eburnean (post-2109Ma) is recorded only in some lithologies and is characterized by the development of crenulation cleavage and chevron or kink folds.

For many authors (Milesi et al. 1992; Beziat et al., 2008; Tshibubudze et al. 2013; Le Mignot et al. 2017; Goldfarb et al. 2017) this post-Eburnean phase is most favorable for gold deposits.

2.2 Bagassi gold deposit

The Bagassi gold deposit is situated in the Houndé greenstone belt in the Province of Balé in Western Burkina Faso (Fig.1b). It consists of two main high-grade gold deposits: the 55 Zone, study area of this work, which consists of a fully underground mine which is currently in production, and Bagassi South, whose production has just started. Other orebodies (109 Zone, 117 Zone, Haho, Kaho…) of the Yaramoko permit are economically less important.

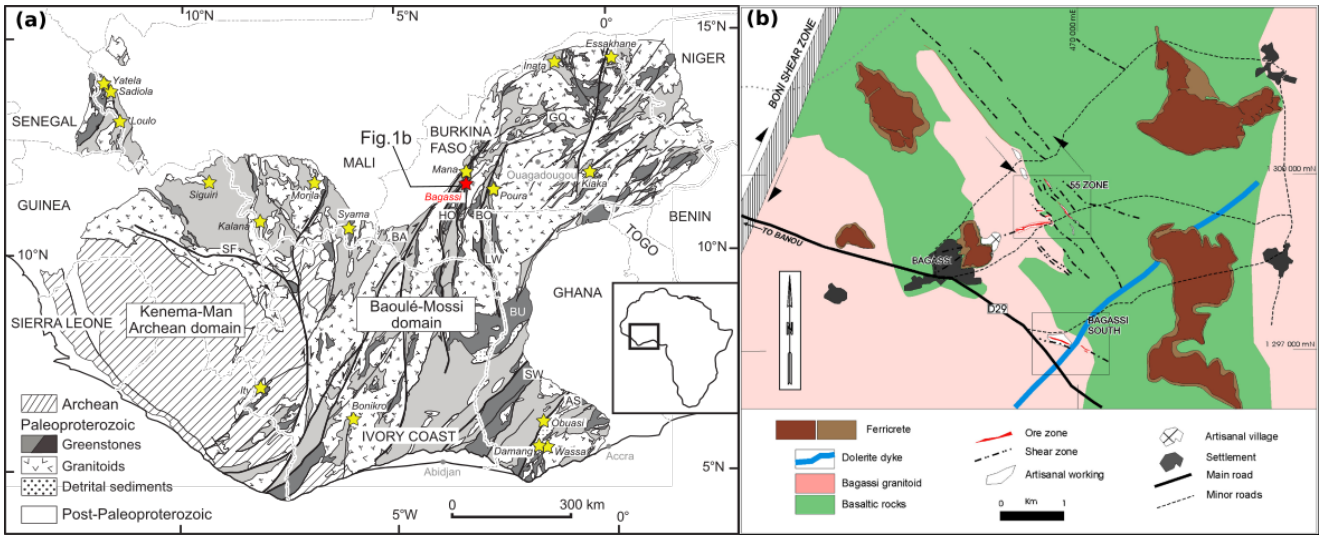

Figure 1: a Simplified map of the southern part of the West African Craton showing the distribution of main gold deposits of the Baoulé-Mossi domain (after BRGM SIG Afrique map, Milesi et al. 2004). Main gold deposit are indicated with yellow stars. Bagassi deposit is outlined by a red star. b Schematic map of the Bagassi deposit showing the main orebodies: 55 Zone and Bagassi South (after Hein 2015).

The 55 Zone has proven and indicative ore reserves to a depth of 750 meters of 1.8 million tons grading 11.47 g/t gold. The mineralization is essentially located at the contact between mafic volcanic rocks and granitoids (Fig.1c) and is marked by a strong structural control (Hein 2015). Two types of mineralization have been observed: (i) disseminated gold associated to pyrite within altered host-rock and ankerite-rich veinlets and (ii) free gold in quartz-rich veins that develop pyrite rich proximal alteration in the host rock.

2.3 Veins System

In 55 Zone, mineralization is associated to dextral shear zones including a vein system which consists of two main vein types.

Type I, early stage ankerite-rich auriferous veinlets. They are made of ankerite (~60%), albite (~15%), quartz (<5%), chlorite (<2%), pyrite (~20%) and gold. Pyrite grains in these veins are characterized by chlorite pressure-shadow fringes.

Type IIa, auriferous laminated quartz-rich veins that show highest gold grades. Their width ranges from decimeter to several meters and they overprint the earlier Type I veins. Albite and ankerite ± calcite are the other main phases in the vein and quartz percentage increases with thickness of the vein. Gold is expressed as individual grains or as particles (1-300µm) at the vicinity of rare pyrite grain found in the vein. Pyrite is predominately located within the altered wall rocks haloes around the veins.

Type IIb, late stage milky quartz veins are the widest veins in 55 Zone and can reach more than 11meters; They are characterized by almost pure quartz and much less gold grains compared to type IIa.

3 LA-ICP-MS analyses on pyrite

LA-ICP-MS was used to obtain quantitative data of pyrite. In order to get the best signal during laser ablation, samples were mounted in epoxy resin and were polished using standard methods. Trace element contents in pyrite were determined at Géosciences Environnement Toulouse by using an ESI NWR193UC Excimer laser coupled to ThermoFinnigan Element XR. Spot diameters of 30 µm associated with repetition rates of 10 Hz with a laser fluency of 4 J.cm^{-2} were used. For each analyze, following 20s of background acquisition, pyrite grain were ablated over the course of at least 60s.

Raw data were processed with the GLITTER® software package (Van Achterbergh et al. 2001) using two external calibrators, Pyrrhotite-Po-726 (Sylvester et al., 2005) and MASS-1 (Wilson et al. 2002) treated as unknowns and ^{57}Fe as internal calibrator. Pyrrhotite-Po-726 was used for Au calibration. For all other elements analyzed in this study, calibration was conducted with the synthetic polymetal sulfide MASS-1. Two other standards, the doped glasses NIST SRM 610 and NIST SRM 612 (Pearce et al. 1997), were used to control the reproducibility and accuracy of the corrections.

4 Chemical and textural features of pyrites

Pyrite is the principal sulfide in the 55 Zone of the Bagassi gold deposit. Two pyrite generation associated to gold mineralization were identified according to petrological and chemical investigations. The division in pyrite generations is arbitrary, based on elemental zoning and textural relationships.

Py_1 is associated to type I veinlets in which it forms coarse-grained crystals and usually occurs as inclusion-rich core of Py_2 where the size is varying from 100 µm to 1,000 µm (Fig. 2a, b). It highlights the 55 Zone shearing event.

Py_2 is the most abundant variety and occurs as two subtypes of coarse-grained crystals of 300 µm to 3 mm (Fig. 2d, e, f). The first subtype of pyrite grains has been deformed and is characterized by chlorite strain fringes. Within these pyrites native gold occurs under different forms: as inclusions or infilling fractures in pyrite. Just like

Py_1, this first type highlights 55 Zone corridor foliations. A second subtype consists of mostly euhedral pyrite grains whose width ranges from 75 µm to 1000 µm. They form clusters and are randomly distributed. No native gold inclusions have been observed in this subtype. However, native gold can be found at the vicinity of these pyrite grains within the in the veins.

Chemical data show that Py_1 is enriched in an enriched in As, Au, Cu and Sb compared to later mostly inclusion-free Py_2 (Fig. 3). As and Au allow the best discrimination between Py_1 and Py_2 with highest As (7,000 to 13,300 ppm) and Au (0.3 to 10 ppm) concentrations found in Py_1 while Py_2 is characterized by much lower values of the same elements, As and Au ranging respectively from 150 to 830 ppm and <0.01 to 0.1 ppm. For other elements, Ni, Co, Cu, Sb, Se, Te, Ag, Zn, Bi and Pb, Py_1 and Py_2 show generally the same contents. The values of Cu, Sb, Ag, Bi and Pb are low in concentration (median <2 ppm).

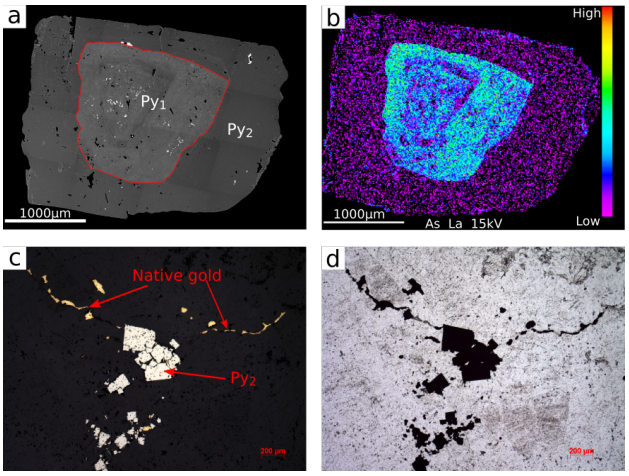

Figure 2. a Backscattered electron images of deformed Py_2. **b** EPMA map showing As distribution between Py1 and deformed Py_2. **c**, **d** Thin section microphotograph of undeformed Py_2 showing relation with native gold in quartz-rich type IIa vein.

5 Pyrite and gold mineralization

Py_1 forms As-rich zones overgrown by Py_2 (Fig. 2a, b). These As-rich bands mark a first fluid stage enriched in As and Au. This first stage is responsible of primary gold event in 55 Zone with invisible gold associated to Py_1 (Fig. 3).

Py_2: Trace element concentrations are less abundant in trace elements than As-rich Py_1. Petrological differences between the two subtypes of Py_2 can be explained by their location in the mineralized zone. In fact, Py_2 with strain fringes are situated along the 55 Zone shear zone corridor. This explains why they are strongly deformed and highlight 55 Zone corridor fabric. The other subtype of Py_2 is principally located in tension gashes associated to the 55 Zone corridor. They are not affected by deformation which explain their mostly euhedral shape (Fig. 2c, d). Py_2 distinguish another ore bearing fluid stage in the 55 Zone. These fluids are depleted in trace elements. Presence of numerous free gold grains in quartz-rich veins suggest an Au-oversaturated fluid. Regular boundaries and lacking of corrosion textures between Py_1 and Py_2 argue against a model of multiple events of sulfide precipitation. Py1 and Py_2 illustrate a single great hydrothermal event with an early stage involving As-Au rich fluids and a later stage with an Au-oversaturated fluid.

In the Bagassi gold deposit, invisible gold can be found in the two generations of pyrite. In As vs Au diagram, all data plot below the Au solubility limit (Fig. 3) of gold in sulfides defined by Reich et al. (2005) for Carlin type deposits. As in pyrite from orogenic deposits controls the behaviour of Au in a similar way to that of Carlin-type systems (Deditius et al. 2014). Several authors (Morey et al. 2008, Velasquez et al. 2014; Li et al. 2018) agree that occurrence of native gold as inclusions in pyrite crystal suggests exsolution/remo-bilization from earlier pyrite matrix. At 55 Zone, Py_2 containing native gold blebs are located along the 55 Zone corridor. Their high gold fineness (>906) may be the result of a remobilization process. As is the most abundant element after Fe and S and notable lack of arsenopyrite in Py_2 means that contribution of remobilized invisible gold from As-rich Py_1 in the 55 Zone deposit, should be low even absent. In this deposit most of gold grains co-precipitated with later Py_2 associated to later Au-oversaturated stage.

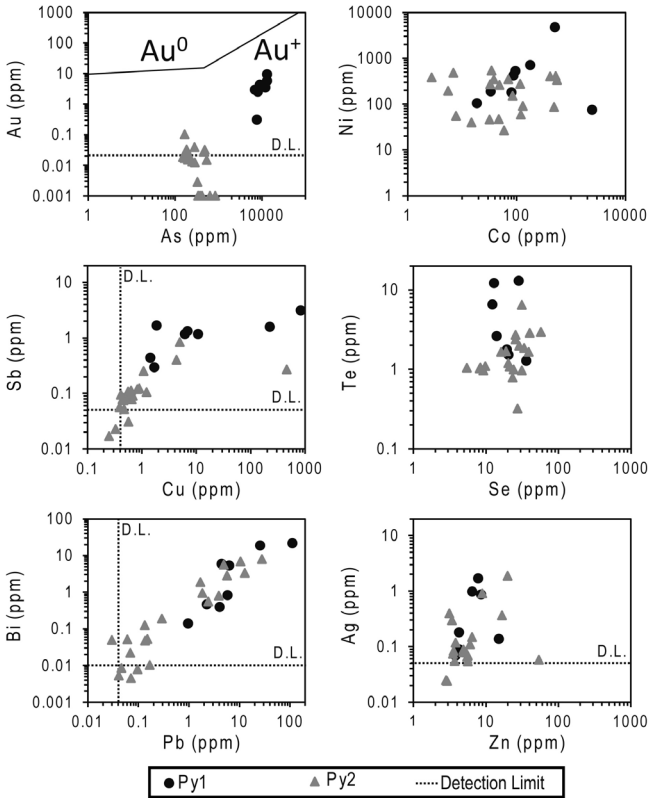

Figure 3. Binary diagrams of selected trace elements in pyrite types from 55 Zone. Gold solubility limit in As vs Au diagram is from Reich et al (2005).

6 Conclusion

At 55 Zone of the Bagassi gold deposit petrological and

chemical analyzes on pyrites allow to distinguish two pyrites generations associated to gold mineralization: As-rich Py_1 with high contents of As and Au and Py_2 showing much less grade of the same elements. Both Py_1 and Py_2 are depleted in Cu, Sb, Ag, Bi and Pb.

Pyrite investigations revealed that, due to regular boundaries and lacking of corrosion textures between Py_1 and Py_2 gold mineralization is associated to a single great hydrothermal event which can be divided into two stages of ore bearing fluids. First stage is marked by As-rich Py_1 is responsible of primary gold mineralization. Second stage is related to As-poor Py_2 and is depleted in trace elements. Most of gold co-precipitated during the second stage with Py_2.

Acknowledgements

This work has been supported by the NGO - Association le Soleil Dans la Main and the WAXI (West African eXploration Initiative) project. We would like to thank Roxgold Inc for providing logistical support and for giving access to drill core samples. We are grateful to GeoRessources (Université de Lorraine) and Laboratoire Géosciences et Environnement Minier (Université Ouaga1) for their technical support. Special thanks to Didier Béziat and GET (Toulouse) for pyrite trace element analyzes.

References

Augustin J, Gaboury D. (2019) Multi-stage and multi-sourced fluid and gold in the formation of orogenic gold deposits in the world-class Mana district of Burkina Faso – Revealed by LA-ICP-MS analysis of pyrites and arsenopyrites. Ore Geol. Rev. 104:495–521

Baratoux L, Metelka V, Naba S, Jessell MW, Gregoire M, Ganne J, (2011) Juvenile Paleoproterozoic crust evolution during the Eburnean orogeny (~2.2-2.0 Ga), western Burkina Faso. Precambrian Res 191:18-45

Béziat D, Dubois M, Debat P, Nikièma S, Salvi S, Tollon F (2008) Gold metallogeny in the birimian craton of Burkina Faso (West Africa). J Afr Earth Sci 50:215-233

Deditius AP, Reich M, Kesler SE, Utsunomiya S, Chryssoulis SL, Walshe J, Ewing RC (2014) The coupled geochemistry of Au and As in pyrite from hydrothermal ore deposits. Geochim Cosmochim Acta 140:644–670

Feybesse JL, Milési JP, (1994) The Archaean/Proterozoic contact zone in West Africa: a mountain belt of decollement thrusting and folding on a continental margin related to 2.1 Ga convergence of Archaean cratons? Precambrian Res 69:199-227

Fougerouse D, Micklethwaite S, Ulrich S, Miller J, Godel B, Adams, DT, McCuaig TC (2017) Evidence for two stages of mineralization in West Africa's largest gold deposit: Obuasi, Ghana. Econ Geol 112:3-22

Goldfarb RJ, André-Mayer AS, Jowitt SM, Mudd GM (2017) West Africa: The World's Premier Paleoproterozoic Gold Province. Econ Geol 112:123-143

Goldfarb RJ, Groves DI, Gardoll S, (2001) Orogenic gold and geologic time: A global synthesis. Ore Geol Rev 18:1-75

Hein KAA (2015). The Bagassi gold deposits on the eastern margin of the Houndé greenstone belt, Burkina Faso. Ore Geol Rev 78:660-666

Kouamelan AN, Delor C, Peucat JJ, (1997) Geochronological evidence for reworking of Archean terrains during the early Proterozoic (2.1 Ga) in the western Côte d'Ivoire (Man Rise-West African Craton). Precambrian Res 86:177–199

Large RR, Danyushevsky L, Hollit C, Maslennikov V, Meffre S, Gilbert S, Bull S, Scott R, Emsbo P, Thomas H, Singh B, Foster J (2009) Gold and trace element zonation in pyrite using a laser imaging technique: Implications for the timing of gold in orogenic and Carlin-style sediment-hosted deposits. Econ Geol 104:635-668

Large RR, Maslennikov V, Robert F, Danyushevsky LV, Chang Z (2007) Multistage sedimentary and metamorphic origin of pyrite and gold in the giant Sukhoi Log deposit, Lena gold province, Russia. Econ Geol 102:1232-1267

Le Mignot E, Siebenaller L, Beziat D, André-Mayer AS, Reisberg L, Salvi S, Velasquez G, Zimmermann C, Nare A (2017) The Paleoproterozoic copper-gold deposits of the Gaoua district, Burkina Faso: Superposition of orogenic gold on a porphyry copper occurrence? Econ Geol 112:99–122

Li XH, Fan HR, Yang KF, Hollings P, Liu X, Hu FF, Cai YC (2018) Pyrite textures and compositions from the Zhuangzi Au deposit, southeastern North China Craton: implication for ore-forming processes. Contrib Mineral Petrol 173:73

Metelka V, Baratoux L, Naba S, Jessell MW (2011) A geophysically constrained litho-structural analysis of the Eburnean greenstone belts and associated granitoid domains, Burkina Faso, West Africa. Precambrian Res 190:48-69

Milési JP, Ledru P, Feybesse JL, Dommanget A, Marcoux E (1992) Early Proterozoic ore deposits and tectonics of the Birimian orogenic belt West Africa. Precambrian Res 58:305-344

Milesi JP, Feybesse JL, Pinna P, Deschamps Y, Kampunzu H, Muhongo S, Lescuyer JL, Le Goff E, Delor C, Billa M, Ralay F, Heinry C (2004) Geological map of Africa 1:10,000,000, SIG Afrique project: Conference of African Geology, 20th, BRGM, Orléans, France

Morey AA, Tomkins AG, Bierlein FP, Weinberg RF Davidson GJ (2008) Bimodal distribution of gold in pyrite and arsenopyrite: Examples from the Archean Boorara and Bardoc shear systems, Yilgarn craton, Western Australia. Econ Geol 103: 599-614

Pearce NJG, Perkins WT, Westgate JA, Gorton MP, Jackson SE, Neal CR, Chenery SP (1997) A compilation of new and published major and trace element data for NIST SRM 610 and NIST SMR 612 glass reference materials. Geostandard Newslett 21:115–144

Reich M, Kesler SE, Utsunomiya S, Palenik CS, Chryssoulis SL, Ewing RC (2005) Solubility of gold in arsenian pyrite. Geochim Cosmochim Acta 69:2781-2796

Thomas HV, Large RR, Bull SW, Maslennikov V, Berry RF, Fraser R, Froud S, Moye R (2011) Pyrite and Pyrrhotite textures and composition in sediments, laminated quartz veins, and reefs at Bendigo gold mine, Australia: insights for ore genesis Econ Geol 106:1-31

Van Achterbergh E, Ryan CG, Griffin WL (2001) Data reduction software for LA-ICP-MS: Mineralogical Association of Canada, Short Course Series 29, 239–243.

Velasquez G, Salvi S, Siebenaller L, Beziat D, Carrizo D (2018) Formation and deformation of pyrite and implications for gold mineralization in the El Callao District, Venezuela. Minerals 8 (10) 430

Velasquez G, Beziat D, Salvi S, Siebenaller L, Borisova AY, Pokrovski GB, de Parseval P (2014) Control of Shear-Zone-Induced Pressure Fluctuations on Gold Endowment: The Giant El Callao District, Guiana Shield, Venezuela. Econ Geol 109:457–486

Tshibubudze A, Hein KAA, (2013) Structural setting of gold deposits in the Oudalan-Gorouol volcano-sedimentary belt east of the Markoye shear zone, West African craton. J Afr Earth Sci 80:31-47

Wilson SA, Ridley WI, Koenig AE (2002) Development of sulfide calibration standards for the laser ablation inductively-coupled plasma mass spectrometry technique. J Anal Atomic Spectrom 17:406-409.